

A THEORETICAL STUDY OF THE SEA BREEZE

by

JOHN E. WALSH

B.A., Dartmouth College, 1970

SUBMITTED IN PARTIAL FULFILLMENT OF THE  
REQUIREMENTS FOR THE DEGREE OF DOCTOR OF PHILOSOPHY

at the

MASSACHUSETTS INSTITUTE OF TECHNOLOGY

December, 1973, i.e. Feb. 1974

Signature of Author .....  
Department of Meteorology, December, 1973

Certified by .....  
Thesis Supervisor

Accepted by .....  
Chairman, Departmental Committee on Graduate Students

WITHDRAWN  
MASS. INST. TECH.  
JAN 18 1974  
MIT LIBRARIES

## A THEORETICAL STUDY OF THE SEA BREEZE

by

John E. Walsh

Submitted to the Department of Meteorology on 17 December 1973  
in partial fulfillment of the requirements for the degree of  
Doctor of Philosophy.

## ABSTRACT

The linearized Boussinesq equations with rotation, viscosity, conduction, and a mean stratification are used to model the sea breeze in two dimensions. The motion is forced by a prescribed surface temperature function.

The linear model produces a sea breeze with realistic velocities and spatial dimensions. Hydrostatic solutions are found to differ very little from the nonhydrostatic solutions. The phase of the solution depends on the coriolis parameter  $f$ ; the only distinguishing feature of the solution at the inertial latitude is a slight amplitude maximum far from the coastline. Both the phase and the amplitude depend on the stability parameter  $N^2$ . An inversion, simulated by a discontinuity in  $N^2$ , reduces the intensity of the circulation. The land-sea temperature difference required by the model to create a net onshore flow in opposition to a basic current agrees well with the empirical criterion defined by Lyons (1972).

The computed vertical heat fluxes, when summed along the coastlines of the principal land masses, indicate that the sea breeze effect can account for several per cent of the globally averaged vertical flux of sensible heat at a height of several hundred meters.

The nonlinear advection process is studied with a finite difference model based on a series of overlapping grids. The principal effect of the nonlinear terms is a landward advection of the sea breeze circulation.

Thesis Supervisor: Norman A. Phillips

Title: Professor of Meteorology

## ACKNOWLEDGEMENTS

The author wishes to express his gratitude to Professor Norman A. Phillips for his active interest and sound advice throughout the course of this study. His understanding and patience have made him an ideal thesis advisor. Professor James Austin is also to be thanked for valuable discussions which added perspective to the research.

Financial support for the author during his stay at M.I.T. came in part from an N.D.E.A. Title IV fellowship and in part from a Research Assistantship supported by NSF grant number GA 28724X.

Thanks are extended to Miss Isabelle Kole for assistance with the figures and to the author's wife for assistance in typing the thesis.

## TABLE OF CONTENTS

ABSTRACT	2
ACKNOWLEDGEMENTS	3
TABLE OF CONTENTS	4
LIST OF FIGURES	6
LIST OF TABLES	8
1. Introduction	9
1.1 Previous work	9
1.2 The present investigation	10
2. The linear model	15
2.1 The equations of motion and the boundary conditions	15
2.2 The method of solution	17
2.3 Results with no basic current	21
2.3.1 Hydrostatic vs. nonhydrostatic solutions	36
2.3.2 Dependence on $f$	39
2.3.3 Dependence on $N^2$	50
2.3.4 Two-layer model	54
2.4 Results with a basic current	59
2.4.1 Dependence on $U$	60
2.4.2 Application to the sea breeze prediction problem	67
3. Heat flux calculations	74
3.1 Formulation	74
3.2 Dependence of the flux on external parameters	77
3.3 Application to actual coastal configurations	82
3.3.1 Results by season and by continent	83
3.3.2 Comparison to other estimates of the sensible heat flux	83
4. The nonlinear finite difference model	87
4.1 Description of the model	88

4.2 Results of the numerical integrations	89
5. Summary and conclusions	101
Appendix A. Numerical aspects of the linear solution	104
Appendix B. Wave number dependence of the linear solution	107
Appendix C. Integration of the flux along a coastline	115
Appendix D. Formulation of the nonlinear model	117
D.1 The system of overlapping grids	118
D.2 Finite difference form of the equations	122
REFERENCES	125
BIOGRAPHICAL NOTE	129

## LIST OF FIGURES

<u>Figure</u>	<u>Page</u>
2.1	Geometry of the linear model. 15
2.2	The x-z streamlines for the symmetric circulation. 22
2.3	Regions of importance of the various terms in the equations of motion. 27
2.4	The buoyancy field for the symmetric circulation. 30
2.5	$u(x)$ at $t = 6$ hours for the symmetric circulation. 33
2.6	$w(x)$ at $t = 6$ hours for the symmetric circulation. 34
2.7	The x-z streamlines with a smoothed forcing function. 35
2.8	Horizontal wind vectors at $x = 0$ for $\frac{f}{\omega} = 0.5, 1.0, 1.5$ . 40
2.9	$u(x)$ at $z = 4$ for $\frac{f}{\omega} = 0.5, 1.0, 1.5$ . 46
2.10	$u(x)$ at $z = 0.33$ for five values of $N^2$ . 51
2.11	Sea breeze onset time at $z = 0.33$ as a function of $N^2$ . 52
2.12	Distribution of $N^2$ in the two-layer model. 54
2.13	$w(x)$ at $t = 6$ hours for the two-layer case and two one-layer cases. 56
2.14	The x-z streamlines at $t = 8$ hours for the asymmetric circulation, $U_{nd} = -250$ . 61
2.15	$w(x)$ at $z = 1$ for the asymmetric circulation, $U_{nd} = -250$ . 62
2.16	$u(x)$ at $z = 0.33$ for the asymmetric circulations, $U_{nd} = -100, -250, -400$ . 64
2.17	The product $u_{\max} \frac{U}{\omega L}$ as a function of $\frac{U}{\omega L}$ . 69
2.18	Sea breeze occurrence criteria: theoretical and observed. 71
2.19	$ U_{crit} $ vs. the critical gradient wind speed deduced from Pearson (1973). 73

<u>Figure</u>		<u>Page</u>
3.1	The time-averaged vertical heat flux $F(x)$ for the symmetric circulation.	76
3.2	Dependence on $f$ of the vertical heat flux.	78
3.3	Dependence on $N^2$ of the vertical heat flux (uniform $N^2$ ).	79
3.4	Dependence on $N^2$ of the vertical heat flux (two-layer cases).	80
3.5	Dependence on $U$ of the vertical heat flux.	81
4.1	Comparison of $u(x)$ from the linear and finite-difference models.	92
4.2	Isopleths of $u$ and $b$ for the nonlinear circulation with no basic current (run # 1a).	93
4.3	Isopleths of $u$ and $b$ for the nonlinear circulation with a basic current (run # 2c).	95
4.4	$u(x)$ at $k = 1$ , $t = 4$ and 8 hours; runs # 1a and 1b.	98
4.5	The $x$ coordinate of $u_{\max}$ as a function of time: linear vs. nonlinear.	99
B.1	The eigenvalues $\lambda_j$ for hydrostatic and nonhydrostatic cases of the symmetric circulation.	108
B.2	The coefficients $b_1, \psi_2, \psi_3, \psi_4$ for the symmetric circulation: $\frac{f}{\omega} = 0.5, 1.0, 1.5$ .	110
D.1	Modified version of the Eliassen finite-difference grid.	117
D.2	The system of overlapping grids.	123
D.3	Cross section along the $x$ axis through a region of grid overlap.	123

## LIST OF TABLES

<u>Table</u>		<u>Page</u>
1.1	Summary of previous numerical studies of the sea breeze.	11
2.1	Comparison of hydrostatic and nonhydrostatic velocities.	38
2.2	Summary of the observational study.	44
3.1	Computed vertical heat fluxes due to the sea breeze effect.	84
4.1	Summary of the nonlinear numerical integrations.	90



## 1. INTRODUCTION

The sea breeze circulation is a mesoscale response of the atmosphere to horizontal variations in surface heating. Because it is generally restricted to the lowest one or two kilometers, the sea breeze is strongly influenced by the boundary layer processes of viscosity and conduction. Yet its horizontal extent is large enough that the earth's rotation and the synoptic scale pressure gradient cannot be ignored. The task of describing and predicting the sea breeze is therefore far from trivial.

### 1.1 Previous work

Both analytic and numerical studies of the sea breeze have appeared in the literature. In the former, solutions have been obtained only after simplifying the governing equations to the point where certain physical processes are omitted. Conduction, for example, is neglected by Schmidt (1947), Pierson (1951), and Smith (1957). Diffusion of momentum is omitted by Defant (1951) as well as by Schmidt and Smith. Bretherton and Geisler (1969) also neglect viscosity and conduction in their model of the sea breeze "forerunner". Malkus and Stern (1953), the first to include a basic current, neglect viscous and coriolis effects in a model of airflow over a heated island. In a recent study of the urban heat island, Olfe and Lee (1971) include a basic current but consider the effects of rotation and viscosity only separately.

Numerical studies have suffered from computational instability effects which have required the use of artificial smoothing devices (see

table 1.1). Fisher (1961) attributed the instability of his solutions to a logarithmic spacing of grid points. Using similar coordinate stretching, Estoque (1961, 1962) was forced to replace the continuity equation with its vertical derivative; the resulting circulation has been shown to violate mass continuity (Neumann and Mahrer, 1971). Moroz (1967) applied Estoque's model to a symmetric lake breeze and found that computational effects dominated the solution after several hours. By abandoning the variable grid spacing, Neumann and Mahrer (1971) obtained stable solutions. Some accuracy was sacrificed, however, by the large (4 km) horizontal spacing of the grid points and by the closeness ( $\pm 36$  km) to the coastline of the lateral boundaries.

In the three dimensional model of McPherson (1968), nonlinear instability was controlled by the application of a filter to the fields of temperature and horizontal velocity. Although the results agreed with observations, the model was so time-consuming that only one 18-hour integration could be performed. Pielke (1973) also obtained realistic results for a particular coastline but, like McPherson's, his study was limited by the small number of experiments which were economically feasible.

## 1.2 The present investigation

This study will emphasize the value of the analytic model as an aid in understanding the sea breeze. Although all the relevant physical processes are included, the model is formulated as simply as possible in order to permit a thorough examination of its properties. The eddy diffusion coefficients  $\nu$  and  $\kappa$  are assumed to be constant in space and

Table 1.1. Numerical studies of the sea breeze

<u>author</u>	<u>hydrostatic or nonhydrostatic</u>	<u>grid size</u>	<u>computational features</u>
Fisher (1961)	hydrostatic	logarithmic $\Delta x = 2-128$ km variable $\Delta z = .015-3.84$ km (15 x 10)	circulation computationally destroyed at $t \approx 10$ hours
Estoque (1961)	hydrostatic	logarithmic $\Delta x = 2-34$ km $\Delta z = 0.1$ km (19 x 20)	upstream differencing; results violate mass continuity
Moroz (1967)	hydrostatic	logarithmic $\Delta x = 6-45$ km $\Delta z = 0.1$ km (16 x 32)	same as Estoque
McPherson (1968)	hydrostatic	$\Delta x = \Delta y = 4$ km $\Delta z = 0.2$ km (70 x 15 x 20)	upstream differencing; external filter applied to u, v, T after each time step
Estoque and Bhumralkar (1969)	hydrostatic	logarithmic $\Delta x = 1-65$ km variable $\Delta z = .002-2.7$ km (31 x 17)	upstream differencing; artificial $K_h = 1.0 \times 10^8 \text{ cm}^2 \text{ sec}^{-1}$

Table 1.1 (continued)

<u>author</u>	<u>hydrostatic or nonhydrostatic</u>	<u>grid size</u>	<u>computational features</u>
Neumann and Mahrer (1971)	nonhydrostatic	$\Delta x = 4$ km $\Delta z = 0.1$ km (20 x 19)	upstream differencing; solution stable for three days
Pielke (1973)	hydrostatic	$\Delta x = \Delta y = 11$ km variable $\Delta z = .05-3.0$ km (33 x 36 x 7)	upstream differencing; artificial horizontal diffusion
Pearson (1973)	hydrostatic	$\Delta x = 5$ km $\Delta z = 0.25$ km (66 x 17)	nonlinear instability after 6-12 hours

time rather than functions of the Richardson number as in Estoque's model. In view of the large uncertainties in estimates of eddy diffusivities (especially horizontal diffusivities), one coefficient is used to represent both horizontal and vertical diffusion of momentum and buoyancy. A comparison of the model results to the observed properties of the sea breeze will show that the model produces a realistic circulation despite the simplified treatment of diffusion. The linear model can then be used to study the other physical processes which contribute to the sea breeze circulation. The underlying hypothesis is that there is much to be learned from a study in which one is free from the financial limitations and the stability problems associated with nonlinear numerical models.

In chapter 2, the linear model is formulated and the method of solution is outlined. The effect of introducing the hydrostatic assumption is studied. The role of the coriolis parameter vis-a-vis the diurnal period is examined in order to determine whether the response changes at the inertial latitude where  $f = \frac{\pi}{12} \text{ hours}^{-1}$ . Variations in the stability parameter  $N^2$  are found to change both the phase and the amplitude of the solution. The tendency for an inversion to damp the circulation is apparent when a discontinuity in  $N^2$  is introduced.

In order to incorporate the effect of a mean advection, a basic current is then included in the model. The scaling of the velocity components is such that one can determine the land-sea temperature difference required to create a net onshore flow in the presence of an offshore gradient wind. Such a relationship between  $U$  and  $\Delta T$  is of practical value in forecasting the occurrence of a sea breeze but has

never been derived theoretically. The theoretical criterion is found to agree very well with the observational data of Lyons (1972), although construction of the theoretical criterion requires that the effects of nonlinear advection be anticipated. The assumptions concerning nonlinear advection are supported by the nonlinear computations described in chapter 4. The nonlinear results are also of some technical interest because they are based on an overlapping grid network rather than the coordinate stretching techniques of earlier models.

The results of the linear model are applied in chapter 3 to a study of the role played by the sea breeze in the general circulation. Integrations along the coastlines of the principal land masses indicate that the sea breeze can account for several per cent of the total vertical flux of sensible heat in the lowest kilometer of the atmosphere.

## 2. THE LINEAR MODEL

The model will employ the cartesian geometry sketched in figure 2.1. The x-axis is oriented perpendicular to the coastline. All variables are assumed to be uniform in the y-direction. Uniform rotation about the z-axis is assumed.

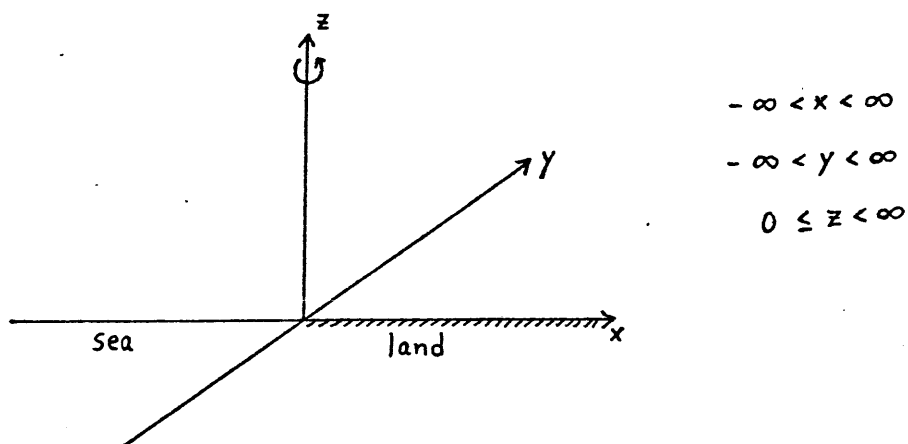


Figure 2.1. Geometry of the linear model

### 2.1 The equations of motion and the boundary conditions

Because the sea breeze rarely extends to heights greater than one or two kilometers, the Boussinesq approximation is made. Rotation, viscosity, and conduction are included. The governing equations, linearized about a basic current  $U$  normal to the coastline, are

$$\frac{\partial u}{\partial t} + U \frac{\partial u}{\partial x} - f v = -\frac{\partial p}{\partial x} + \nu \nabla^2 u \quad (2.1)$$

$$\frac{\partial v}{\partial t} + U \frac{\partial v}{\partial x} + f u = \nu \nabla^2 v \quad (2.2)$$

$$\frac{\partial w}{\partial t} + U \frac{\partial w}{\partial x} = -\frac{\partial p}{\partial z} + b + \nu \nabla^2 w \quad (2.3)$$

$$\frac{\partial b}{\partial t} + U \frac{\partial b}{\partial x} + N^2 w = \kappa \nabla^2 b \quad (2.4)$$

$$\frac{\partial u}{\partial x} + \frac{\partial w}{\partial z} = 0 \quad (2.5)$$

where  $\nabla^2 = \frac{\partial^2}{\partial x^2} + \frac{\partial^2}{\partial z^2}$ ,  $p = \frac{p - p_a}{\rho_{a0}}$ ,  $b = \frac{T - T_0 + \frac{g}{c_p} z}{T_0}$ , and  $N^2 = \frac{d\bar{b}}{dz}$ . The variables (u,v,w) are the velocity components in the (x,y,z) directions. The "buoyancy" b and the "pressure" p represent deviations of the temperature and pressure, respectively, from the temperature and pressure in an adiabatic atmosphere (Ogura and Phillips, 1962). The Brunt-Vaisälä frequency  $N^2$ , a stability index, gives the increase with height of the horizontally averaged buoyancy.  $\nu$  and  $\kappa$  are the eddy coefficients of viscosity and conduction, while  $f = 2\omega \sin \phi$  is the coriolis parameter. Constant values are assigned to f,  $N^2$ ,  $\nu$ , and  $\kappa$ . For simplicity,  $\nu$  and  $\kappa$  are assumed to be equal.

The boundary conditions are that all variables remain finite at large z, that u, v, and w vanish at the ground, and that b reduce to the specified forcing function at  $z = 0$ . This forcing function varies periodically with time to simulate the diurnal cycle:

$$b_0 = \begin{cases} b_{max} \sin \omega t & x > 0 \\ -b_{max} \sin \omega t & x < 0 \end{cases} \quad (2.6)$$



where  $b_{\max}$  is a positive real constant and  $\omega = \frac{2\pi}{24}$  hours<sup>-1</sup>. The time  $t = 0$  corresponds to sunrise.

## 2.2 The method of solution

The equations will now be non-dimensionalized. Time is scaled by the forcing frequency  $\omega$ , buoyancy by the amplitude  $b_{\max}$  of the surface buoyancy perturbation in (2.6), and both horizontal and vertical distances by the diffusive length  $L = \sqrt{\frac{\kappa}{\omega}}$ . (For the typical value of  $\kappa = 5 \times 10^4$  cm<sup>2</sup> sec<sup>-1</sup>,  $L$  is approximately 250 m). Denoting nondimensional variables by primes, the complete scaling is

$$\begin{aligned} L &= \sqrt{\frac{\kappa}{\omega}} \\ U &= \omega L U_{nd} \\ t &= \frac{t'}{\omega} & b &= b_{\max} b' \\ (x, z) &= L (x', z') & (u, v, w) &= \frac{b_{\max}}{\omega} (u', v', w') \\ \frac{\partial}{\partial t} - \nu \nabla^2 &= \omega \left( \frac{\partial}{\partial t'} - \nabla'^2 \right) & p &= b_{\max} L p' \end{aligned}$$

We note that the dimensional velocities are directly proportional to the maximum land-sea temperature difference.

Introducing the stream function  $\psi$  ( $u = -\frac{\partial \psi}{\partial z}$ ,  $w = \frac{\partial \psi}{\partial x}$ ) and substituting the nondimensional variables into (2.1)-(2.5), one obtains

$$\frac{\partial}{\partial t} \left( \frac{\partial \psi}{\partial z} \right) + U_{nd} \frac{\partial}{\partial x} \frac{\partial \psi}{\partial z} + \frac{f}{\omega} v = \frac{\partial p}{\partial x} + \nabla'^2 \frac{\partial \psi}{\partial z} \quad (2.7)$$

$$\frac{\partial v}{\partial t} + U_{nd} \frac{\partial v}{\partial x} - \frac{f}{\omega} \frac{\partial \psi}{\partial z} = \nabla'^2 v \quad (2.8)$$

$$\frac{\partial}{\partial t} \left( \frac{\partial \psi}{\partial x} \right) + U_{nd} \frac{\partial^2 \psi}{\partial x^2} = - \frac{\partial p}{\partial z} + b + \nabla^2 \frac{\partial \psi}{\partial x} \quad (2.9)$$

$$\frac{\partial b}{\partial t} + U_{nd} \frac{\partial b}{\partial x} + \frac{N^2}{\omega^2} \frac{\partial \psi}{\partial x} = \nabla^2 b \quad (2.10)$$

where the primes have been dropped. The value of  $x = y$  will enter the solution only by determining the length scale  $L$  and the strength of the basic current  $U$ .

Solutions to (2.7)-(2.10) are obtained by using Fourier integrals for the  $x$ -dependence:

$$(b, \psi, p, v) = \text{Re} \left\{ \int_{-\infty}^{\infty} (B, \bar{\Psi}, P, V) e^{i(kx+zt)} dk \right\} \quad (2.11)$$

where  $B, \bar{\Psi}, P,$  and  $V$  are functions of  $k$  and  $z$ . The boundary condition (2.6) for the surface buoyancy and the vanishing of  $u, v,$  and  $w$  at  $z = 0$  lead to

$$B(k, 0) = - \frac{1}{\pi k}$$

$$\bar{\Psi}(k, 0) = \frac{\partial \bar{\Psi}}{\partial z}(k, 0) = 0 \quad (2.12)$$

$$V(k, 0) = 0$$

The four differential equations are

$$\mathcal{L} \frac{\partial \bar{\Psi}}{\partial z} + \frac{f}{\omega} V = ikP \quad (2.13)$$

$$\mathcal{L} V - \frac{f}{\omega} \frac{\partial \bar{\Psi}}{\partial z} = 0 \quad (2.14)$$

$$ik \mathcal{L} \Psi = -\frac{\partial P}{\partial z} + B \quad (2.15)$$

$$\mathcal{L} B + ik \frac{N^2}{\omega^2} \Psi = 0 \quad (2.16)$$

where

$$\mathcal{L} = \frac{\partial}{\partial t} + U_{nd} \frac{\partial}{\partial x} - \nabla^2 = \kappa^2 - \frac{\partial^2}{\partial z^2} \quad (2.17)$$

and

$$\kappa = \sqrt{i(1 + U_{nd}k) + k^2} \quad (\text{Re}\{\kappa\} \geq 0)$$

(2.13)-(2.16) can be solved for any of the four unknowns. The equations for  $\Psi$  and B are

$$\left[ \left( \mathcal{L}^2 + \frac{f^2}{\omega^2} \right) \frac{\partial^2}{\partial z^2} - \left( \mathcal{L}^2 + \frac{N^2}{\omega^2} \right) k^2 \right] \Psi = 0 \quad (2.18)$$

$$\mathcal{L} \left[ \left( \mathcal{L}^2 + \frac{f^2}{\omega^2} \right) \frac{\partial^2}{\partial z^2} - \left( \mathcal{L}^2 + \frac{N^2}{\omega^2} \right) k^2 \right] B = 0 \quad (2.19)$$

It is evident that B contains a solution which satisfies  $\mathcal{L}(B) = 0$  and in which  $\mathcal{L}\Psi = 0$ . Utilizing the upper boundary condition on B, this solution is

$$\begin{aligned} B &= b_1 e^{-\kappa z} \\ \Psi &= 0 \\ P &= -\kappa^{-1} B \\ V &= ik \frac{\omega}{f} P \end{aligned} \quad (2.20)$$

where  $b_1$  is a constant which will be determined later. (2.20) is a hydrostatic, geostrophic solution ( $\frac{\partial \Psi}{\partial x} = \frac{\partial \Psi}{\partial z} = 0$ ) in which the vertical

structure is such that time changes in V and B are due solely to viscosity and conduction.

It is now necessary to consider the operator

$$\theta = \left( \mathcal{L}^2 + \frac{f^2}{\omega^2} \right) \frac{\partial^2}{\partial z^2} - \left( \mathcal{L}^2 + \frac{N^2}{\omega^2} \right) k^2$$

from (2.18) and (2.19) where  $\theta \Psi = 0$  and  $\mathcal{L} \theta B = 0$ . Substituting solutions of the form  $e^{-\lambda z}$  gives a characteristic equation in  $\lambda$ :

$$\left[ (\lambda^2 - \kappa^2)^2 + \frac{f^2}{\omega^2} \right] \lambda^2 - k^2 \left[ (\lambda^2 - \kappa^2)^2 + \frac{N^2}{\omega^2} \right] = 0 \quad (2.21)$$

The roots in  $\lambda$  are complex and occur in three pairs of the form  $\pm(a+bi)$ .

The upper boundary conditions require that only roots with positive real parts be chosen; these will be denoted by  $\lambda_2, \lambda_3,$  and  $\lambda_4$ , while  $\kappa \equiv \lambda_1$ , from (2.20).

(2.21) is solved numerically by the procedure outlined in Appendix A. Solutions for typical values of  $\frac{f}{\omega}$  and  $\frac{N^2}{\omega^2}$  are discussed in Appendix B.

The solutions to (2.13)-(2.16) are then

$$\Psi(k, z) = \sum_{j=2}^4 \psi_j(k) e^{-\lambda_j z} \quad (2.22)$$

$$B(k, z) = b_1 e^{-\kappa z} + \sum_{j=2}^4 \alpha_j \psi_j e^{-\lambda_j z} \quad (2.23)$$

$$V(k, z) = -\frac{ik}{\kappa} \frac{\omega}{f} b_1 e^{-\kappa z} + \sum_{j=2}^4 \gamma_j \psi_j e^{-\lambda_j z} \quad (2.24)$$

$$P(k, z) = -\frac{1}{\kappa} b_1 e^{-\kappa z} + \sum_{j=2}^4 \epsilon_j \psi_j e^{-\lambda_j z} \quad (2.25)$$

where

$$\alpha_j = \frac{i k \frac{N^2}{\omega^2}}{\lambda_j^2 - \kappa^2} \quad j = 2, 3, 4$$

$$\gamma_j = \frac{\frac{f}{\omega} \lambda_j}{\lambda_j^2 - \kappa^2} \quad j = 2, 3, 4$$

$$\epsilon_j = \frac{-i k (\lambda_j^2 - \kappa^2) - \alpha_j}{\lambda_j} \quad j = 2, 3, 4$$

The surface boundary conditions on  $u$ ,  $v$ ,  $w$ , and  $b$  become

$$\sum_{j=2}^4 \lambda_j \psi_j = 0 \quad (2.26)$$

$$-i \frac{k}{\kappa} \frac{\omega}{f} b_1 + \sum_{j=2}^4 \gamma_j \psi_j = 0 \quad (2.27)$$

$$\sum_{j=2}^4 \psi_j = 0 \quad (2.28)$$

$$b_1 + \sum_{j=2}^4 \alpha_j \psi_j = -\frac{1}{\pi k} \quad (2.29)$$

(2.26)-(2.29) comprise a system of four simultaneous linear equations which can be solved for the four unknowns.

The complete solution for a single wave component has now been obtained, and the problem is reduced to an integration over  $k$  for fixed  $x, z, t$  according to the previous definitions of the Fourier integrals. The numerical integration procedure is described in Appendix A.

### 2.3 Results with no basic current

The computed circulation is illustrated in the  $x$ - $z$  streamline plots of figure 2.2 for the case of  $U = 0$ ,  $\frac{f}{\omega} = 1.5$  ( $\phi = 48.6^\circ$ ) and

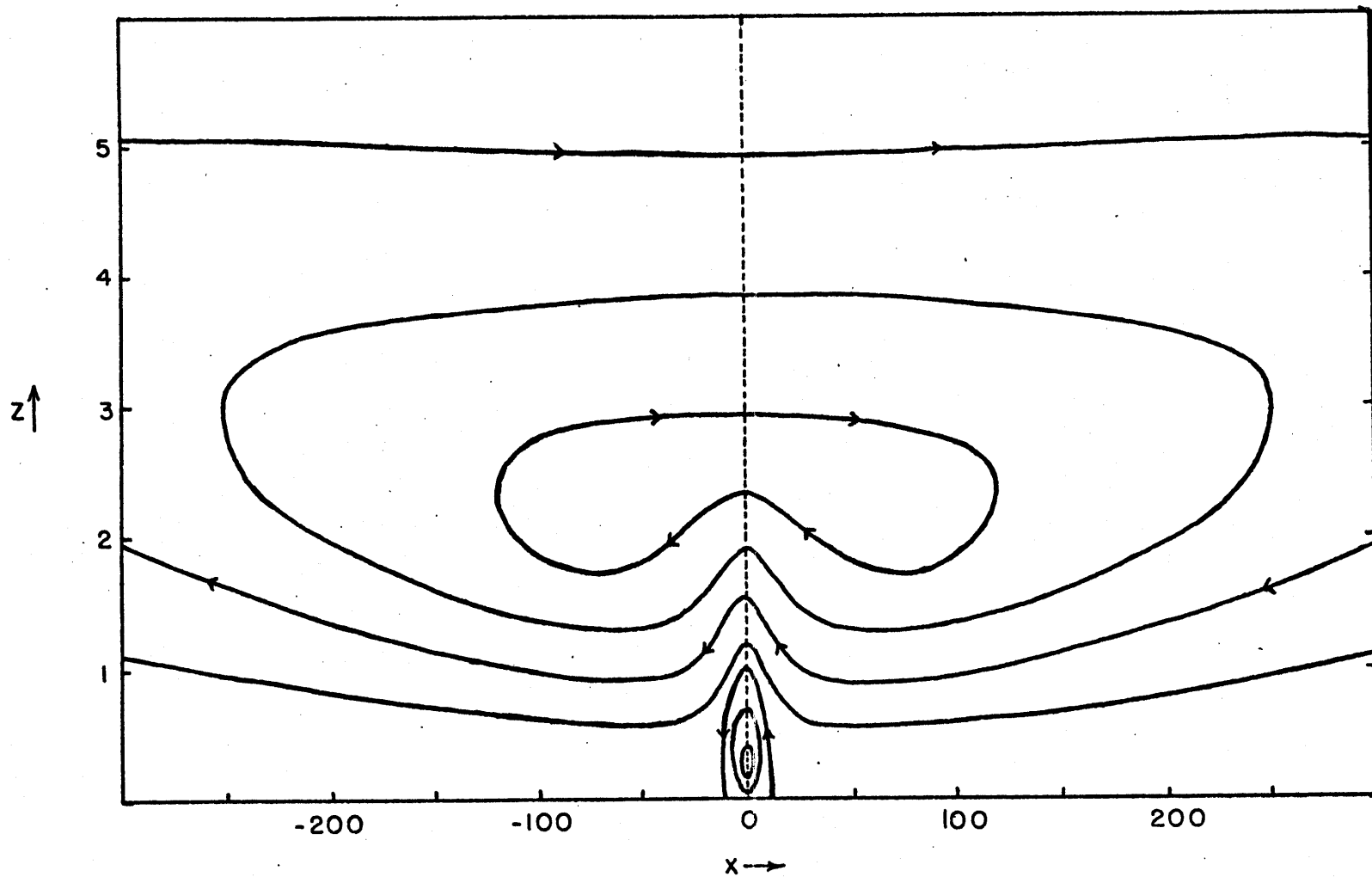


Figure 2.2a.  $x$ - $z$  streamlines at  $t = 2$  hours for the case of  $\frac{f}{\omega} = 1.5$ ,  $N^2 = 10^{-4} \text{ sec}^{-2}$ , and  $U = 0$ .  $x$  and  $z$  are nondimensional.

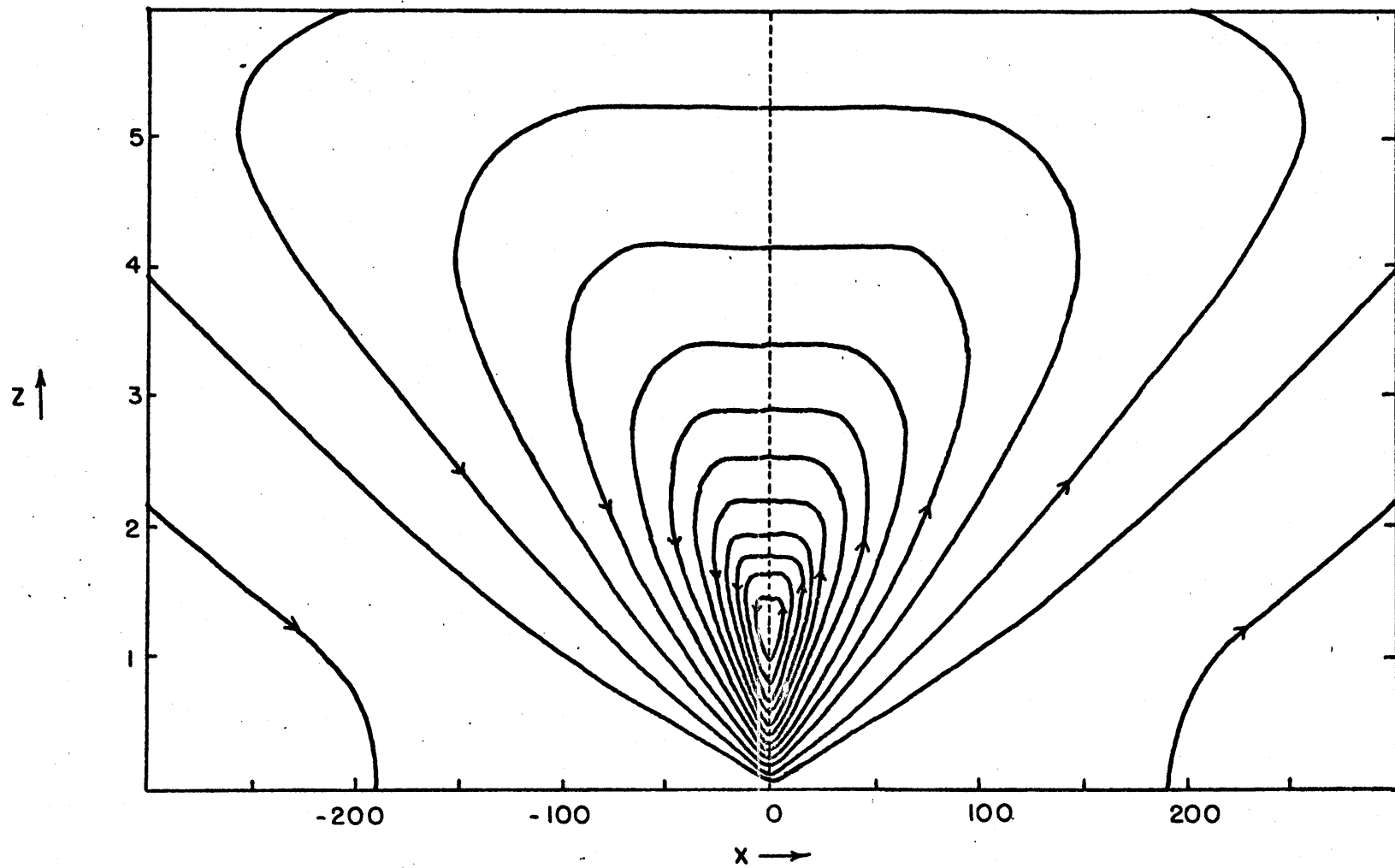


Figure 2.2b. Same as figure 2.2a but for  $t = 6$  hours.

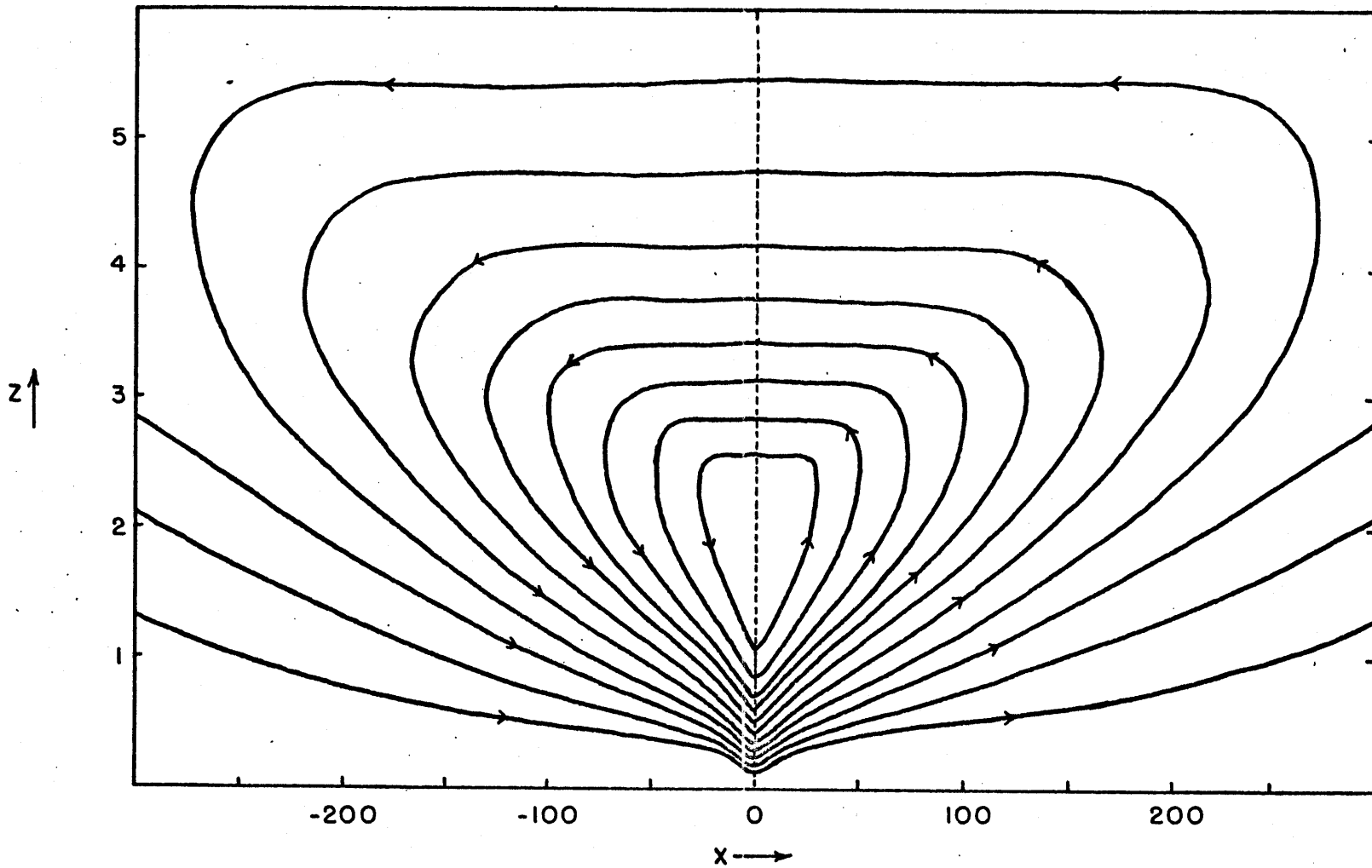


Figure 2.2c. Same as figure 2.2a but for  $t = 10$  hours.



$N^2 = 10^{-4} \text{ sec}^{-2}$ . If  $x$  is taken as  $5 \times 10^4 \text{ cm}^2 \text{ sec}^{-1}$ , each unit on the abscissa and ordinate represents approximately 0.25 km. The velocities in later figures of this section are dimensionalized by assuming that  $b_{\text{max}} = 9.8 \text{ cm sec}^{-2}$ , corresponding to a maximum land-sea temperature difference of about  $\pm 5.5 \text{ C}^\circ$ . The forcing function is given by (2.6).

As seen in figure 2.2a, the remnants of the land breeze persist for several hours after sunrise. The sea breeze circulation first appears near the surface and extends inland to  $x \approx 2 \text{ km}$  by 2 hours. It then develops rapidly and completely displaces the land breeze. By  $t = 6 \text{ hours}$  (figure 2.2b), maximum wind speeds are  $u \approx 4.2 \text{ m sec}^{-1}$  and  $w \approx 56 \text{ cm sec}^{-1}$  in the region of closely packed streamlines near the coastline. The onshore winds near the coastline continue to increase slightly until  $t \approx 8 \text{ hours}$ , about two hours after the maximum surface temperature perturbation. Frictional deceleration and coriolis deflection then begin to decrease  $u$ . Farther inland, maximum wind speeds occur several hours later as the  $u$  and  $w$  waves propagate inland at a finite rate. Figure 2.2c ( $t = 10 \text{ hours}$ ) shows the circulation when its intensity is decreasing.

The depth of the low-level onshore current depends on  $x$  and  $t$ . At a fixed  $x$ , the depth increases with time as shown in figures 2.2a-2.2c. This feature is in agreement with the observations of Moroz (1967). The model of Geisler and Bretherton (1969), on the other hand, predicts a disturbance which settles to the ground as time progresses. The difference is presumably due to the fact that Geisler and Bretherton introduced the differential heating instantaneously, while in this model the buoyancy accelerates the circulation continuously and is

periodic in time.

At a fixed time, the depth of the onshore sea breeze flow increases with distance from the coastline. Figures 2.2b and 2.2c show that the layer of onshore winds is 2-3 times deeper at  $x = 100$  than at  $x = 0$ .

The upper-level return current, which is essentially horizontal, contains maximum wind speeds which are less than 50% as strong as those in the onshore flow. This result is also supported by the observations of Moroz (1967).

The relative importance of the various forces is assessed by examining the individual terms in the equations of motion. Figure 2.3 shows the major components of the force balance in different regions of the  $x$ - $z$  plane at  $t = 6$  hours. (Terms are defined as unimportant when less than 0.1 as large in magnitude as the two largest terms in the equation). Figures 2.3a and 2.3b show that the rotation terms in the  $u$  and  $v$  momentum equations are important at all  $(x,z)$ . The pressure gradient term in the  $u$  equation is also important at all  $(x,z)$ . Friction can be neglected only well above the surface at  $x \geq 100$ . Figure 2.3c shows that the system is essentially hydrostatic, while figure 2.3d shows that vertical conduction cannot be neglected anywhere. The advection of buoyancy by the vertical motion ( $N^2 w$ ) is important at small  $x$  near the surface and at larger  $x$  aloft. It is to be noted that this discussion is valid for  $t = 6$  hours and that the relative importance of the various terms, especially the local accelerations "A", may change with time.

A closer examination of the factors affecting the buoyancy can be made from figure 2.4, which shows the computed values of  $b$  at two-hour

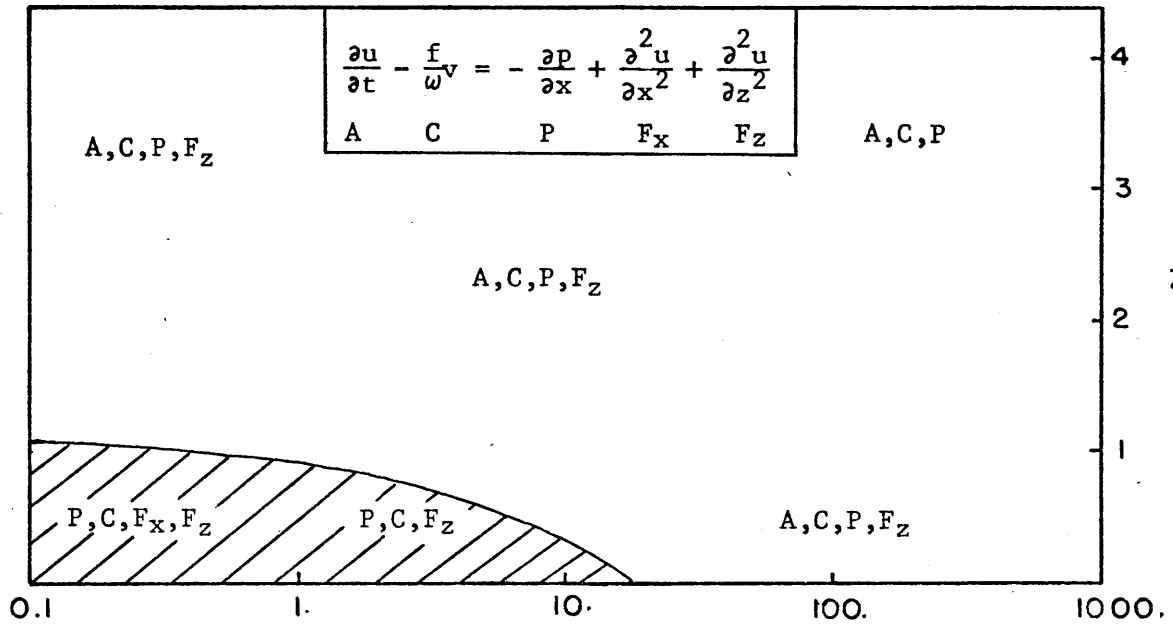


Figure 2.3a. u equation

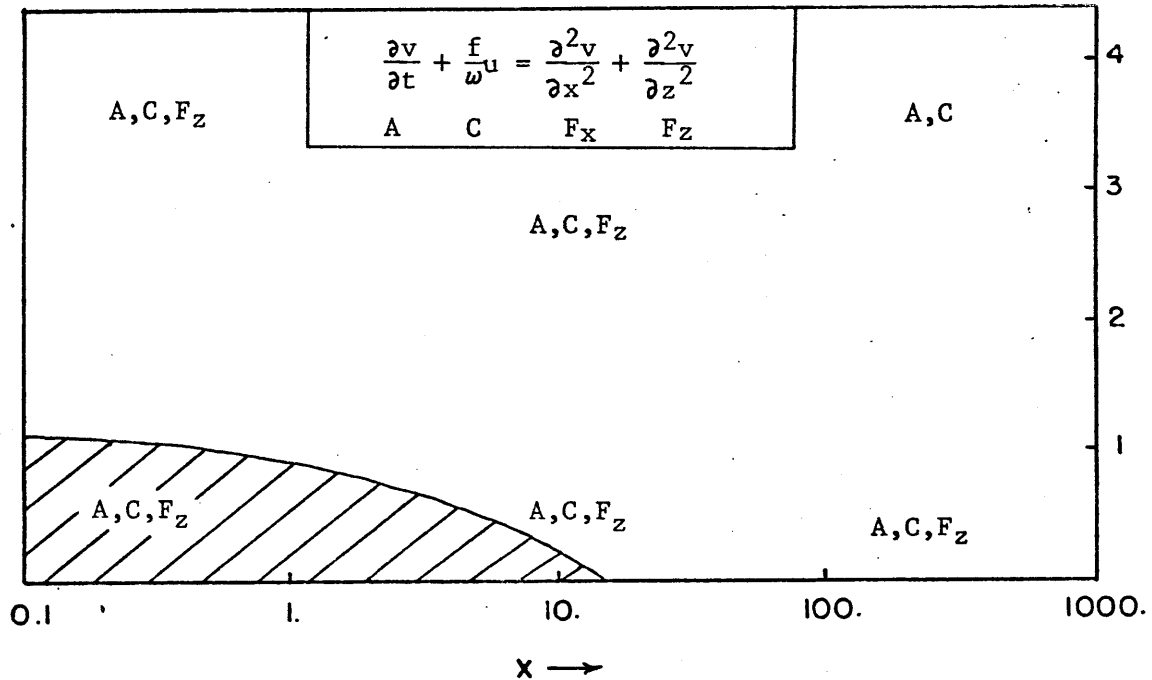


Figure 2.3b. v equation

Figure 2.3. Regions of importance (see text) of the various terms in the equations of motion at  $t = 6$  hours. In the shaded regions, the nonlinear advection terms are important.  $x$  and  $z$  are nondimensional.

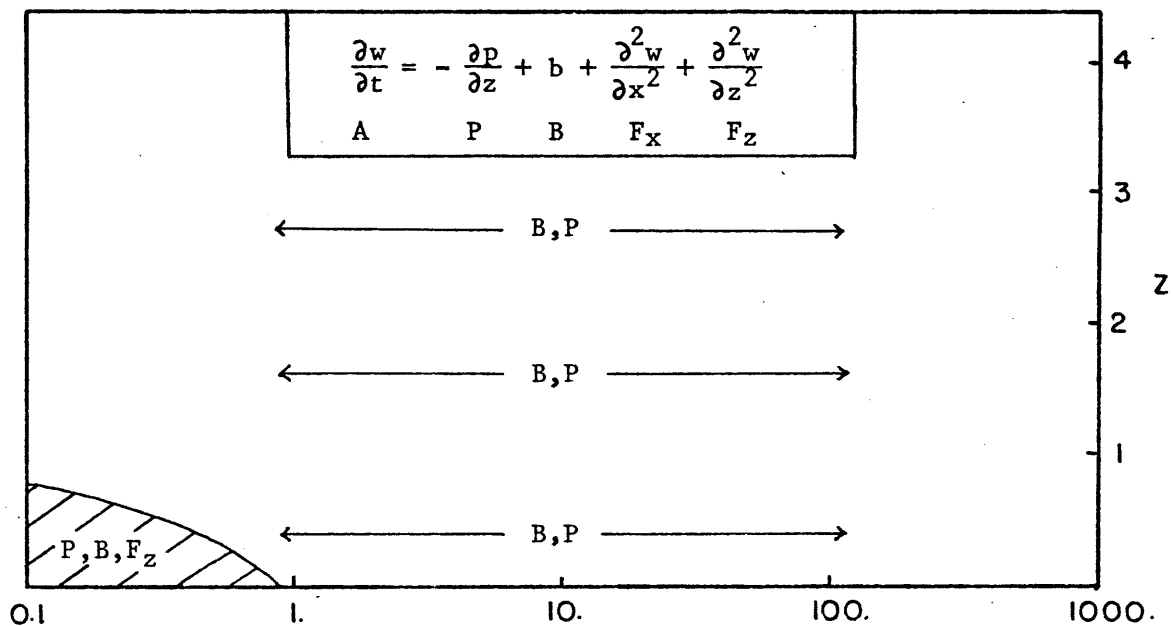


Figure 2.3c. w equation

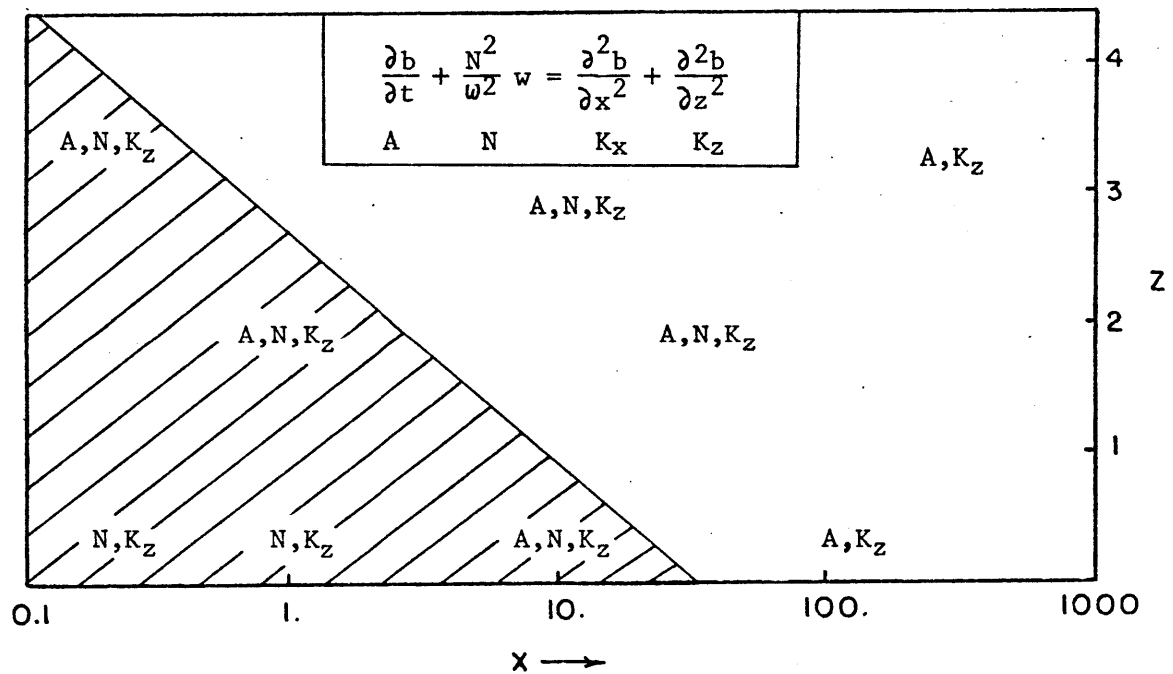


Figure 2.3d. b equation

intervals. Also shown are the values of  $b$  satisfying the diffusion equation  $\frac{\partial b}{\partial t} = \frac{\partial^2 b}{\partial z^2}$  and the lower boundary condition on  $b$ :

$$b = e^{-\frac{z}{\sqrt{2}}} \sin\left(t - \frac{z}{\sqrt{2}}\right)$$

According to this solution, the following phase lags and amplitudes (relative to the prescribed surface values) would be expected if diffusion were the only factor acting to change  $b$ :

	phase lag	amplitude / surface amplitude
$z = 0.33$	0.9 hrs	0.79
$z = 1.00$	2.7 hrs	0.49
$z = 2.00$	5.4 hrs	0.24
$z = 4.00$	10.8 hrs	0.06

At  $z = 0.33$  (figure 2.4a), the diffusive solution describes  $b$  for all  $x \geq 100$ . (The slight disagreement at very large  $x$  is evidently due to approximations in the numerical integrations). At higher levels (figure 2.4b), one must proceed farther from the coastline in order that the diffusive solution be valid. As implied by figure 2.3d, the additional factor affecting the solution at larger  $z$  is the  $N^2 w$  term.

The nonlinear advection terms can be estimated from the linear solution; they are dimensionalized by the factor  $\frac{b_{\max}}{\omega^2 L}$ . In the shaded regions of figure 2.3, the nonlinear terms are important (by the 0.1 criterion). Figures 2.3a and 2.3b show that the nonlinear terms in the horizontal momentum equations are important only at small  $x$  ( $\leq 10$ )

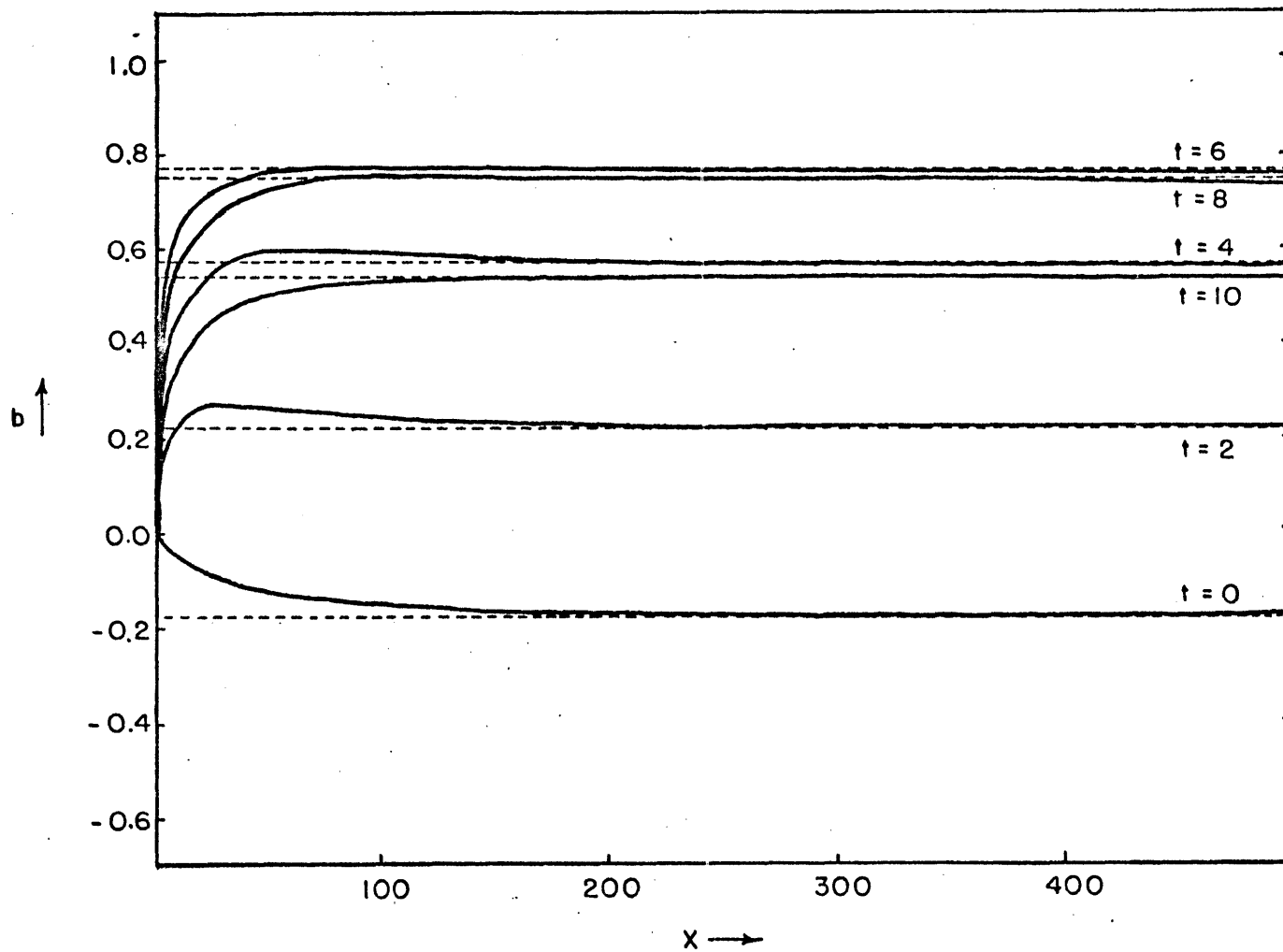


Figure 2.4a. Computed values of the buoyancy at  $z = 0.33$  for the case of  $\frac{f}{\omega} = 1.5$ ,  $N^2 = 10^{-4} \text{ sec}^{-2}$ , and  $U = 0$ . Values of  $b$  ( $\text{cm sec}^{-2}$ ), dimensionalized by  $b_{\text{max}} = 9.8 \text{ cm sec}^{-2}$ , are shown at 2-hour intervals. Dashed lines show values of  $b$  satisfying the diffusion equation.  $x$  and  $z$  are nondimensional.

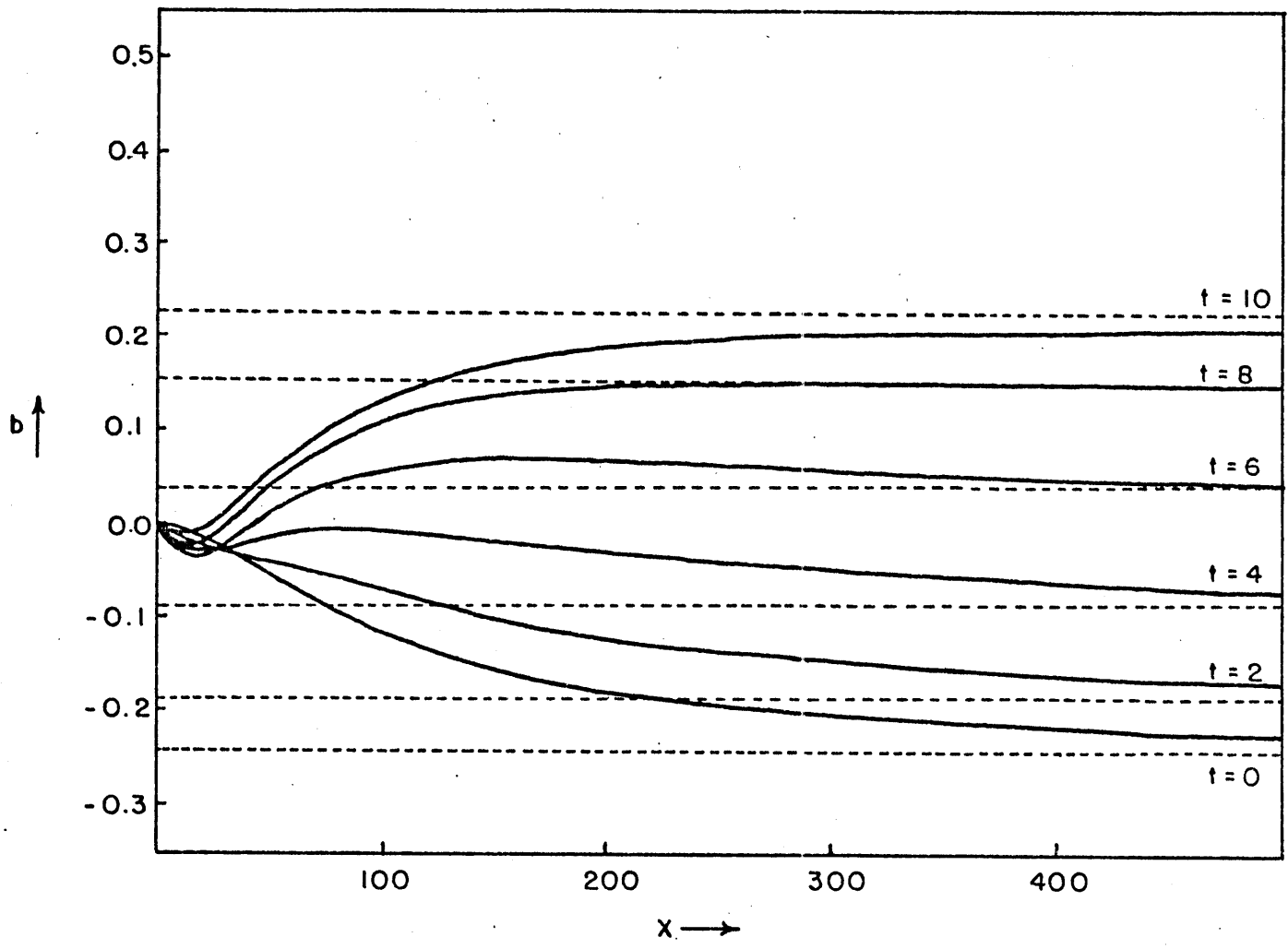


Figure 2.4b. Same as figure 2.4a but for  $z = 4$ .

and  $z$  ( $\leq 1$ ). According to figure 2.3d, however, the omission of non-linear temperature advection is more serious.

The absence of temperature advection has its consequences in the computed velocity profiles. Figures 2.5 and 2.6 show  $u$  and  $w$  as functions of  $x$  at  $t = 6$  hours. The sharpness of the peaks at  $z = 0.33$  and  $z = 0.67$  is somewhat unrealistic, since the concentration of large values near the coastline creates very large gradients. In the atmosphere, the advection of cooler temperatures from offshore will tend to reduce the temperature of the land near the coast. As a result of the "smoothed" forcing function, the observed values of  $w$  (Defant, 1950) are smaller than those of figure 2.6 near the coastline and larger farther inland. (The negative  $w$  near the coastline at  $z = 1, 2, 4$  in figure 2.6 appear to be remnants of the land breeze circulation).

The smoothing of the surface temperature field can be anticipated in the model by removing the discontinuity in the lower boundary condition on  $b$ :

$$b_0 = \begin{cases} -b_{\max} \sin \omega t & x \leq -a \\ \frac{x}{a} b_{\max} \sin \omega t & -a \leq x \leq a \\ b_{\max} \sin \omega t & x \geq a \end{cases}$$

where  $a = \text{constant} \approx 50$ . Figure 2.7, which is to be compared with figure 2.2b, shows that the streamlines are much less concentrated than in the previous case. The corresponding values of  $u$  and  $w$  are considerably more realistic than those in figures 2.5 and 2.6.

Alternatively, advection can be incorporated into the model by including a basic current ( $U \neq 0$ ). The results, discussed in section 2.4, are again in better agreement with observation.



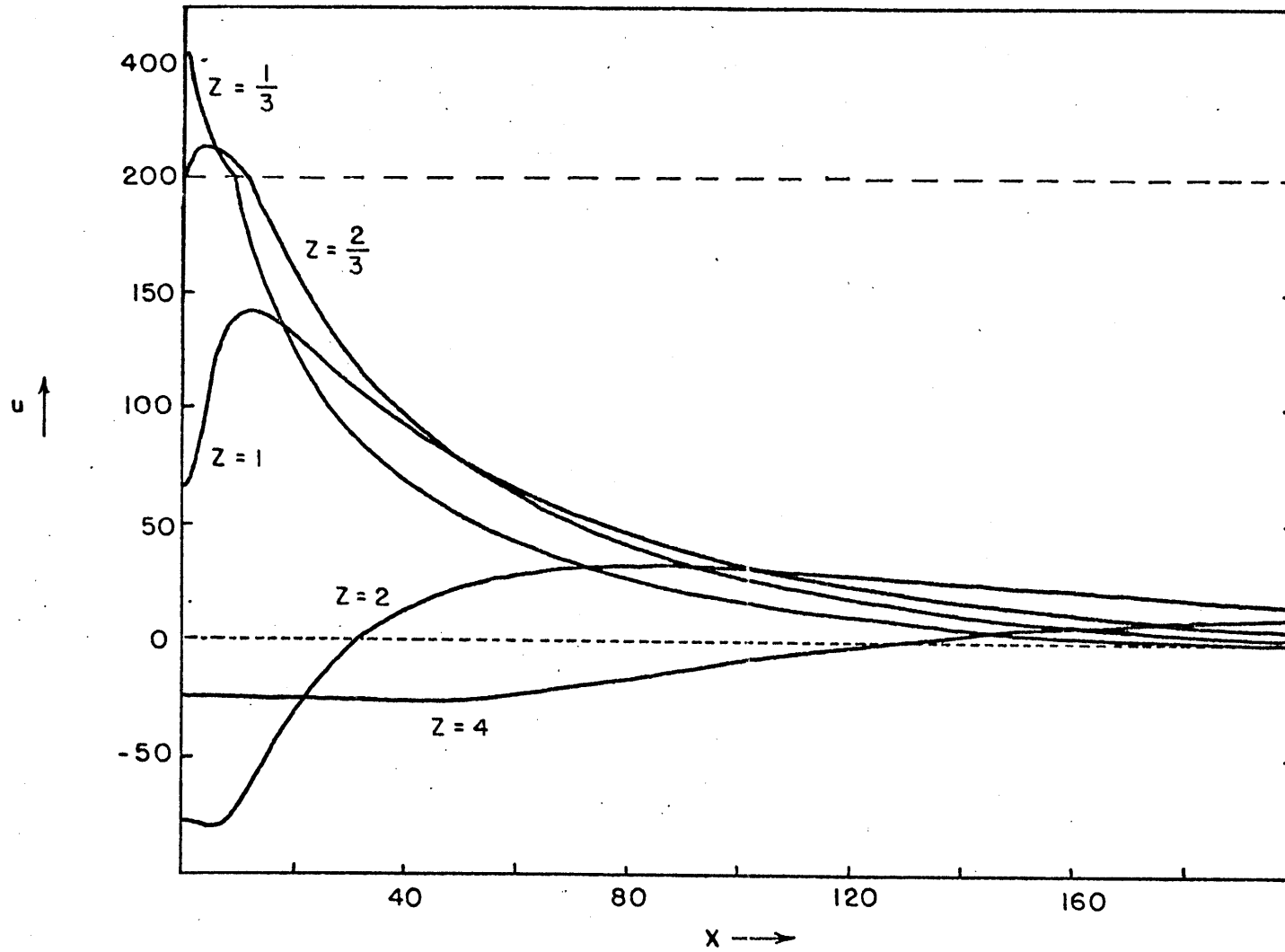


Figure 2.5.  $u$  component of the velocity at  $t = 6$  hours for the case of  $\frac{f}{\omega} = 1.5$ ,  $N^2 = 10^{-4} \text{ sec}^{-2}$ , and  $U = 0$ . Velocities ( $\text{cm sec}^{-1}$ ) are scaled using  $b_{\text{max}} = 9.8 \text{ cm sec}^{-2}$ ;  $x$  and  $z$  are nondimensional.

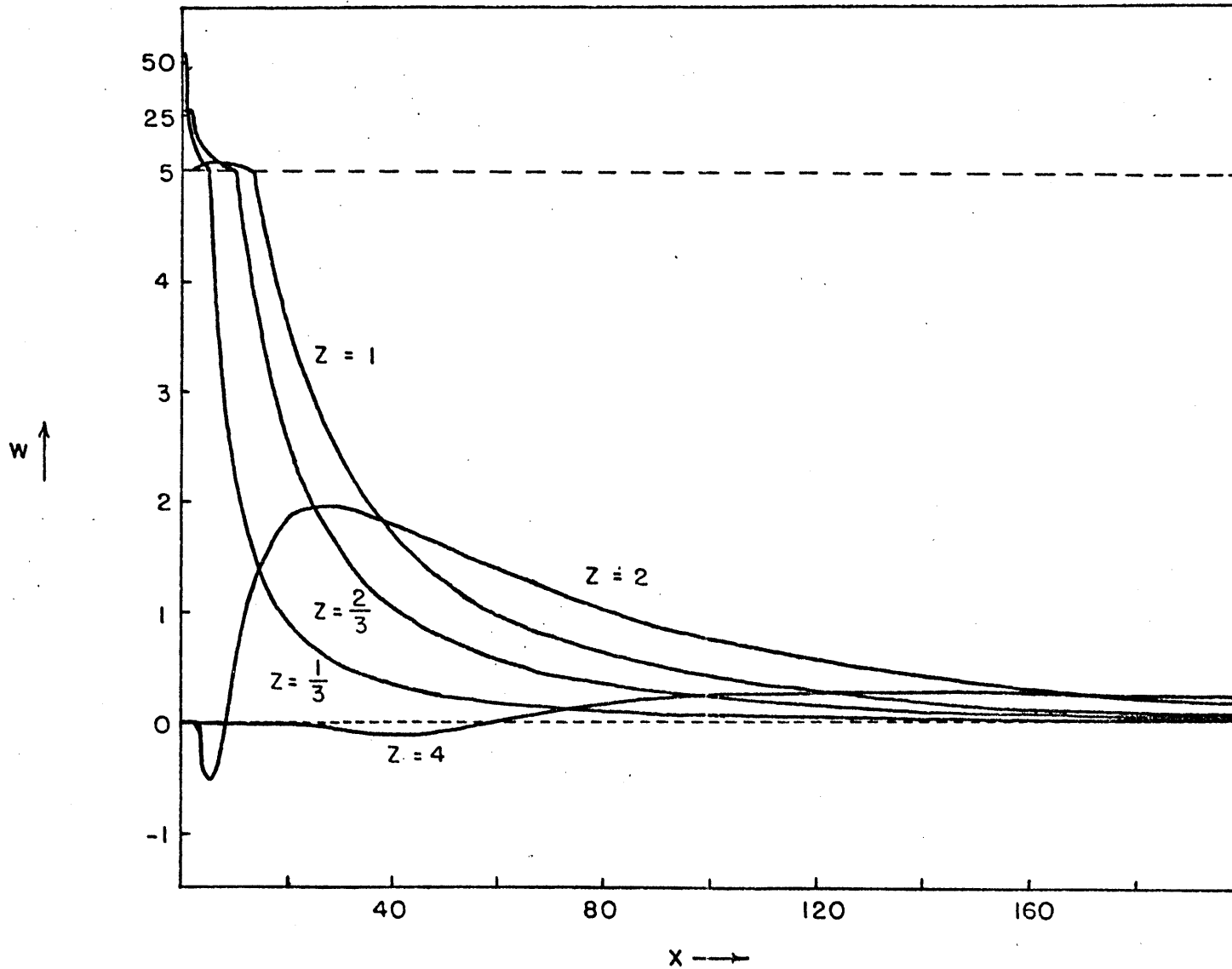


Figure 2.6.  $w$  component of the velocity at  $t = 6$  hours for the case of  $\frac{f}{\omega} = 1.5$ ,  $N^2 = 10^{-4} \text{ sec}^{-2}$ , and  $U = 0$ . Velocities ( $\text{cm sec}^{-1}$ ) are scaled using  $b_{\text{max}} = 9.8 \text{ cm sec}^{-2}$ ;  $x$  and  $z$  are nondimensional.

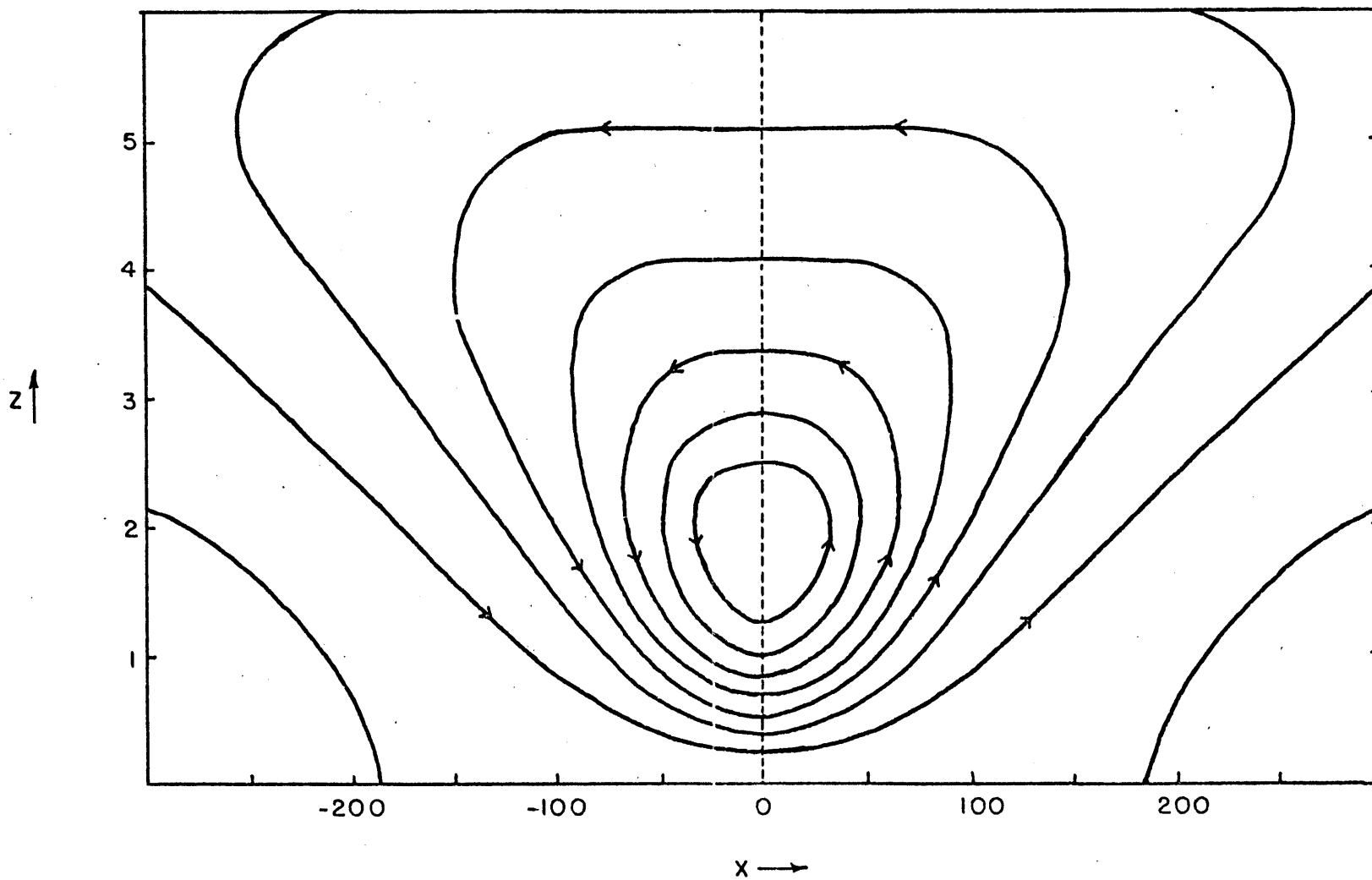


Figure 2.7.  $x$ - $z$  streamlines at  $t = 6$  hours for the case of  $\frac{f}{\omega} = 1.5$ ,  $N^2 = 10^{-4} \text{ sec}^{-2}$ , and  $U = 0$ ;  $x$  and  $z$  are nondimensional. Surface buoyancy is a linear function of  $x$  in the region  $-50 \leq x \leq 50$ .

### 2.3.1 Hydrostatic vs. nonhydrostatic solutions

From a review of the literature, it is apparent that there is a difference of opinion concerning the validity of the hydrostatic assumption in sea breeze models. Previous studies have not compared the results of hydrostatic and nonhydrostatic versions of the same model. Estoque's (1961) model is hydrostatic, although Bhumralkar (1972) notes that nonhydrostatic effects should be investigated when Estoque's model is applied to a tropical island. Neumann and Mahrer (1971) claim that the vertical acceleration  $\frac{\partial w}{\partial t}$  cannot be neglected. However, their scale analysis is based on an adiabatic stratification and the a priori assumption that the pressure variation has a magnitude  $\rho W^2$ . In a more consistent approach, the horizontal equation of motion is used to scale the pressure variation. Denoting the horizontal and vertical length scales by L and H, the velocity scales by U and W ( $\frac{U}{L} \sim \frac{W}{H}$ ), and the time scale by  $\tau$ , one obtains

$$\delta p \sim L \rho \frac{U}{\tau} \quad \frac{1}{\rho} \frac{\partial p}{\partial z} \sim \frac{L^2}{H^2} \frac{W}{\tau} \sim \frac{L^2}{H^2} \frac{\partial w}{\partial t}$$

Any a priori conclusion about hydrostatic balance depends then on a knowledge of  $\frac{L}{H}$ , a ratio which is not determined by the usual formulation of the sea breeze problem. However, it is certainly inconsistent to use a horizontal grid increment of 4 km and a total depth of 2 km -- as Neumann and Mahrer did -- if nonhydrostatic effects are thought to be significant.

The hydrostatic approximation is made in (2.1)-(2.5) by neglecting  $\frac{\partial^2}{\partial x^2}$  in the Laplacian operator and by retaining only the pressure and

buoyancy terms in (2.3). One proceeds as before to obtain equations corresponding to (2.18) and (2.19):

$$\left[ \left( \mathcal{L}'^2 + \frac{f^2}{\omega^2} \right) \frac{\partial^2}{\partial z^2} - k^2 \frac{N^2}{\omega^2} \right] \bar{\Psi} = 0 \quad (2.30)$$

$$\mathcal{L}' \left[ \left( \mathcal{L}'^2 + \frac{f^2}{\omega^2} \right) \frac{\partial^2}{\partial z^2} - k^2 \frac{N^2}{\omega^2} \right] B = 0 \quad (2.31)$$

where, assuming  $U = 0$ ,

$$\mathcal{L}' = \kappa'^2 - \frac{\partial^2}{\partial z^2} \quad \kappa' = \sqrt{i} = \frac{1+i}{\sqrt{2}}$$

The solution for which  $\bar{\Psi} = 0$  and  $\mathcal{L}' B = 0$  differs from (2.20) only in that  $\kappa$  is replaced by  $\kappa'$ . When solutions of the form  $e^{-\lambda z}$  are assumed, the characteristic equation corresponding to (2.21) is

$$\left[ (i - \lambda^2)^2 + \frac{f^2}{\omega^2} \right] \lambda^2 - k^2 \frac{N^2}{\omega^2} = 0 \quad (2.32)$$

and the roots  $\lambda_2$ ,  $\lambda_3$ , and  $\lambda_4$ , chosen as before, are not the same as in the nonhydrostatic case. The values of  $\alpha_j$  and  $\gamma_j$  ( $j=2,3,4$ ) and the coefficients  $b_1$ ,  $\psi_2$ ,  $\psi_3$ ,  $\psi_4$  obtained from the four lower boundary conditions will also be changed by the hydrostatic assumption.

In Appendix B, the eigenvalues  $\lambda_j$  are shown as functions of  $k$  for the hydrostatic and nonhydrostatic cases. The values are the same (to three significant figures) for small  $k$ , but differences begin to appear when  $k$  increases beyond  $10^{-2}$ . In fact, when (2.21) and (2.32) are examined for the case of large  $k$ , it is found that the hydrostatic approximation changes the power dependence on  $k$  of each  $\lambda_j$ . As shown

Table 2.1.  $u, v, w$  in  $\text{cm sec}^{-1}$  for  $\frac{f}{\omega} = 1.5, N^2 = 10^{-4} \text{ sec}^{-2}; t = 6 \text{ hours}$

		<u>x = 0.25</u>		<u>x = 1.0</u>		<u>x = 5.0</u>		<u>x = 25.0</u>		<u>x = 105.0</u>	
		hyd	non	hyd	non	hyd	non	hyd	non	hyd	non
z = 4	u	-24.1	-24.1	-24.1	-24.1	-24.1	-24.1	-25.5	-25.6	-6.99	-6.99
	v	-36.0	-34.3	-34.8	-34.1	-31.2	-31.4	-22.1	-22.1	-18.1	-18.1
	w	0.00	0.00	0.00	0.00	0.00	0.00	-0.07	-0.07	0.29	0.29
z = 2	u	-78.9	-78.9	-78.9	-78.9	-82.4	-82.3	-14.0	-14.0	29.9	29.9
	v	42.6	43.4	41.5	42.5	36.2	35.9	11.8	11.8	18.9	18.9
	w	-0.00	0.00	0.01	0.04	-0.55	-0.53	1.95	1.95	0.74	0.74
z = 1	u	11.4	9.51	13.5	16.7	114.	114.	120.	120.	30.7	30.7
	v	2.42	-1.63	-6.26	-5.55	-28.0	-27.9	-23.2	-23.2	22.1	22.1
	w	-0.04	-1.41	0.35	1.17	8.65	8.59	2.89	2.89	0.39	0.39
z = $\frac{2}{3}$	u	125.	136.	202.	201.	251.	251.	138.	138.	25.2	25.2
	v	-28.4	-31.7	-39.7	-38.6	-50.4	-50.2	-26.9	-26.9	16.7	16.7
	w	-2.06	5.78	20.0	18.8	10.0	10.0	1.91	1.91	0.22	0.22
z = $\frac{1}{3}$	u	429.	411.	413.	411.	266.	266.	106.	106.	15.7	15.7
	v	-43.3	-44.4	-47.1	-46.2	-42.2	-42.2	-18.7	-18.7	8.91	8.91
	w	72.8	56.0	27.2	27.1	4.94	4.99	0.67	0.67	0.07	0.07

in Appendix B, however, the solutions for large  $k$  contribute small amounts to the integrals in (2.11).

Integrated values of  $\begin{pmatrix} u \\ v \\ w \end{pmatrix}$  at  $t = 6$  hours are shown in table 2.1 for both the hydrostatic and nonhydrostatic cases. The velocities have been scaled using  $b_{\max} = 9.8 \text{ cm sec}^{-2}$ , corresponding to  $(\Delta T)_{\max} \approx \pm 5.5 \text{ C}^\circ$ . It is apparent that only minor changes result when the hydrostatic approximation is made. Only at small  $x$  ( $\leq 5$ ) and  $z$  ( $\leq 1$ ), where  $\frac{\partial w}{\partial t}$  and  $\frac{\partial^2}{\partial x^2}$  are largest, are there differences of more than 2-3%. The percentage differences are greatest in the  $w$  field. In all regions, the qualitative features of the circulation are unchanged.

### 2.3.2 Dependence on $f$

Solutions were computed for cases in which the coriolis frequency is less than ( $\frac{f}{\omega} = 0.5$ ), equal to ( $\frac{f}{\omega} = 1.0$ ), and greater than ( $\frac{f}{\omega} = 1.5$ ) the forcing frequency  $\omega$ . The corresponding latitudes are  $14.5^\circ$ ,  $30.0^\circ$ , and  $48.6^\circ$ . Both the phase and the amplitude of the solution show a dependence on  $f$ .

Figure 2.8 shows the computed horizontal wind vectors at the coastline ( $x = 0$ ) for five levels in the vertical. Vectors are plotted at two-hour intervals beginning at  $t = 0$  (sunrise). The stability is the same in each case,  $N^2 = 10^{-4} \text{ sec}^{-2}$ , and all velocities are scaled using  $b_{\max} = 9.8 \text{ cm sec}^{-2}$ . A basic current is not included.

In all three cases, the vectors at  $x = 0$  are similar in magnitude. The winds rotate in the expected clockwise sense under the influence of coriolis deflection, although the  $v$  components become noticeably larger as  $f$  is increased.

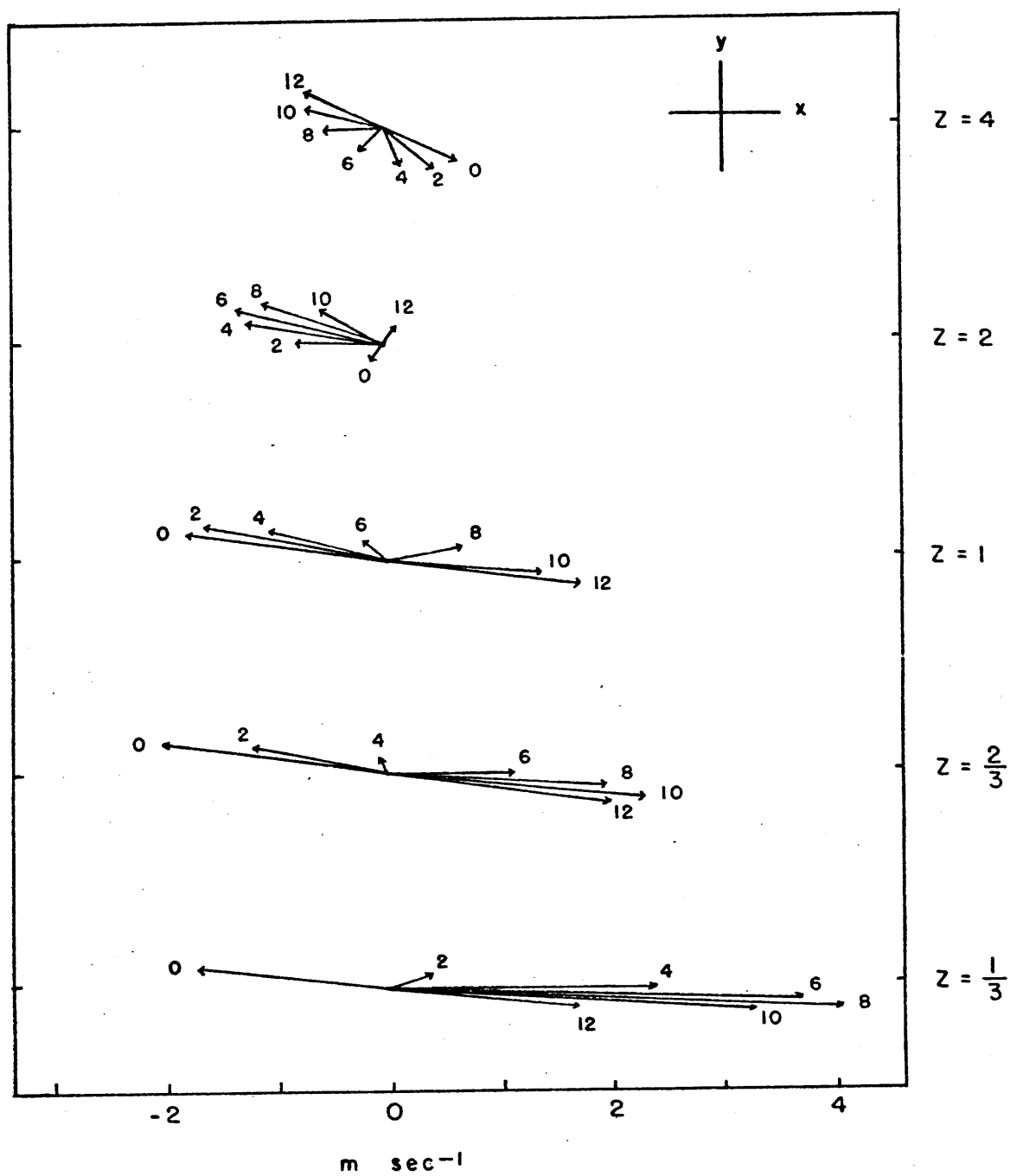


Figure 2.8a. Horizontal wind vectors at  $x = 0$  for the case of  $\frac{f}{U} = 0.5$ ,  $U = 0$ ;  $z$  is nondimensional. Velocities ( $\text{m sec}^{-1}$ ) are scaled using  $b_{\text{max}} = 9.8 \text{ cm sec}^{-2}$ .



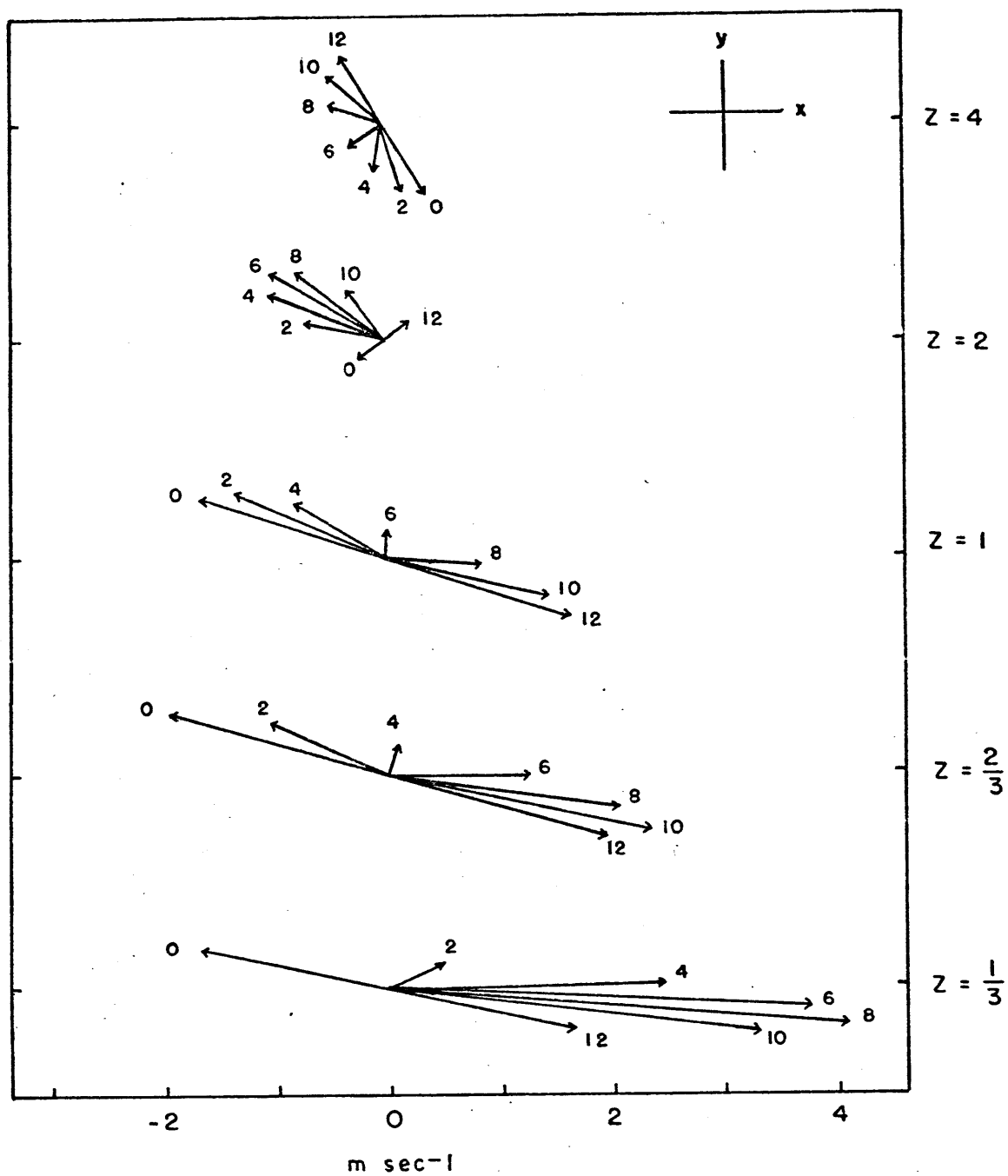


Figure 2.8b. Same as figure 2.8a but for  $\frac{f}{\omega} = 1.0$ .

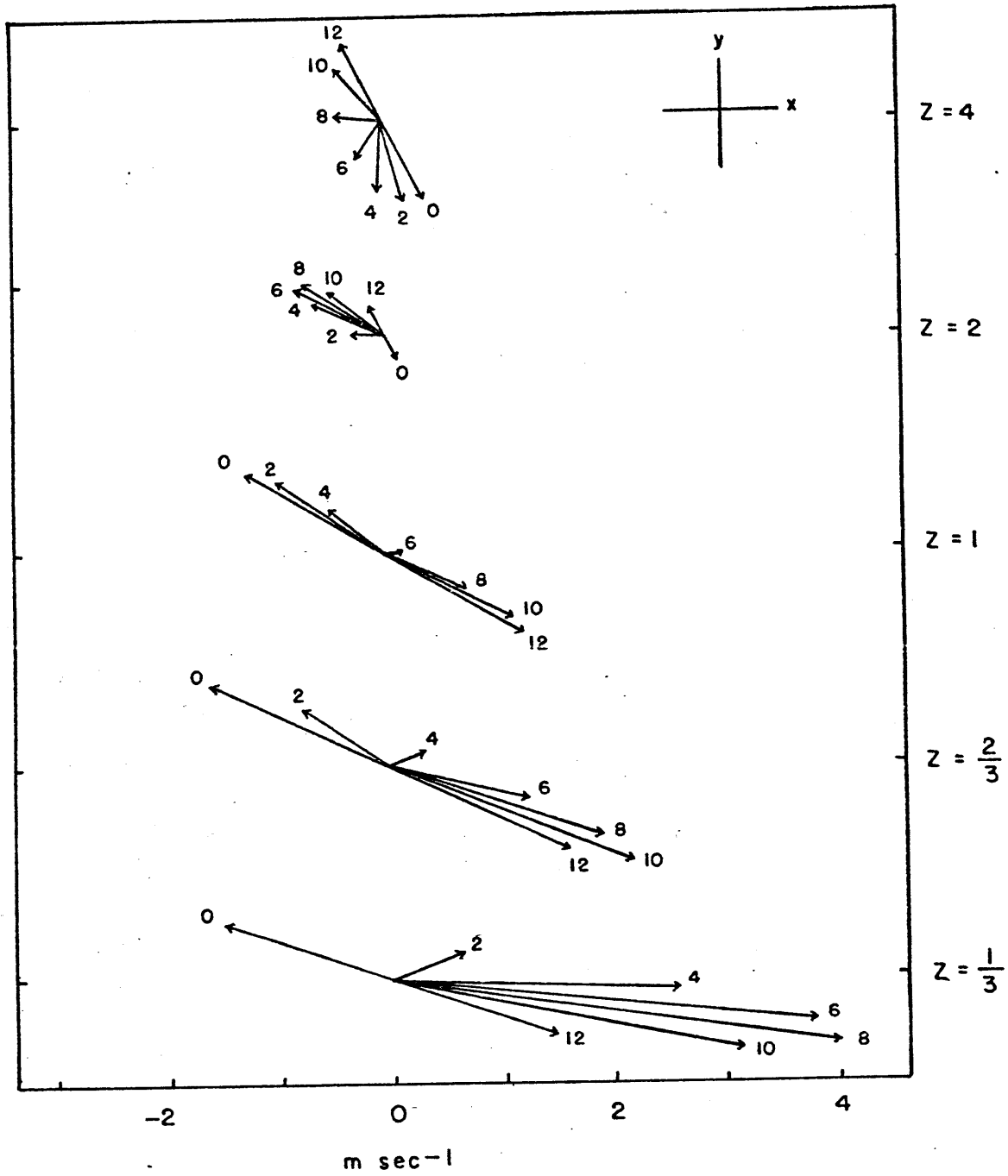


Figure 2.8c. Same as figure 2.8a but for  $\frac{f}{\omega} = 1.5$ .

In the onshore current, there is a slight phase shift as  $\frac{f}{\omega}$  is increased from 0.5 to 1.5. This phase shift is as large as 2 hours at  $z = 0.67$  and  $z = 1$ . Above the surface, therefore, an earlier sea breeze onset time is predicted for the higher latitudes. A similar phase shift is predicted at inland points. In the region  $200 \leq x \leq 800$ , the phase shift is as large as 4 hours at  $z = 1$  and  $z = 2$ , although the wind speeds are quite small at these large distances from the coast.

The phase dependence follows from the simplified system

$$\frac{\partial u}{\partial t} - fv = -ku + e^{i\omega t}$$

$$\frac{\partial v}{\partial t} + fu = -kv$$

which can be solved for  $u(t)$  and  $v(t)$ . The criterion for  $u = 0$  (sea breeze onset) is

$$\tan t = \frac{k}{\omega} \left( \frac{\frac{f^2}{\omega^2} + \frac{k^2}{\omega^2} + 1}{\frac{f^2}{\omega^2} - \frac{k^2}{\omega^2} - 1} \right)$$

When typical values of  $k$  are inserted, one finds that  $u$  becomes positive several hours earlier with  $\frac{f}{\omega} = 1.5$  than with  $\frac{f}{\omega} = 0.5$ . Evidently the transition between the land and sea breeze phases is hastened by the stronger rotational effect at higher latitudes.

In order to compare this result with observations, a study was made using 12 equinoctial months of surface data for Portland, Me. ( $\frac{f}{\omega} \approx 1.4$ ) and Daytona Beach, Fla. ( $\frac{f}{\omega} \approx 1.0$ ). Both stations are approximately the same distance from the coastline. The results are summarized in table 2.2. Although the average sea breeze onset time at each station agrees with

Table 2.2. Summary of observational study

station	<u>Portland, Me.</u>	<u>Charleston, S.C.</u>	<u>Daytona Beach, Fla.</u>
latitude	43.8° N	32.9° N	29.2° N
distance from coastline	8 km (x ≈ 32)	25 km (x ≈ 100)	9 km (x ≈ 36)
# of sea breeze <sup>1</sup> cases	34	34	51
average onset time (hours after sunrise)	3.4	5.1	3.4
stability correlation <sup>2</sup>	-0.05	-0.40	no upper air data

<sup>1</sup> data sample: sea breeze days within one month of either equinox, 1970-72. sea breeze days satisfied the following criteria: surface wind shifted at least 30° in one hour to an off-the-water trajectory; synoptic pressure gradient less than 1 mb / 150 km; skies at most partly cloudy; land temperature greater than mean monthly ocean temperature.

<sup>2</sup> stability correlation: correlation coefficient between 1) time of sea breeze onset (hours after sunrise) and 2) the quantity  $\frac{\Delta\theta}{\Delta z}$  for the surface-to-850 mb layer calculated from the 1200Z sounding.

the theoretical onset time ( $z = 0.33$ ) to within one hour, there is no significant difference between the observed surface onset times at the two latitudes. Figures 2.8b and 2.8c suggest that hourly upper air wind observations would be most appropriate for testing the theoretical phase results. This type of data is unavailable.

In addition to its effect on the phase, the latitude parameter  $\frac{f}{\omega}$  is found to influence the magnitude of the theoretical velocities at large  $x$  and large  $z$ . Figures 2.9a-2.9c show that the magnitude of  $u$  at  $z = 4$ ,  $x \geq 300$  is several times larger at  $30^\circ$  than at the higher and lower latitudes. The nodal point in figure 2.9b indicates the presence of a standing wave in the  $u$  field when  $f = \omega$ .

Although the  $v$  fields are not shown here, the values of  $v$  in this region are also largest at  $30^\circ$ , as one might expect from the magnitudes of the  $u$  components that are subjected to coriolis deflection. The  $f = \omega$  nodal point appears as a minimum in the  $v$  amplitude at  $x \approx 200$ .

The  $f$  dependence of the amplitudes can be explored further by examining the inviscid form of (2.1)-(2.5). In the absence of conduction, the motion is assumed to be forced by a prescribed vertical velocity at the surface:

$$w = W_0 \cos kx \sin \omega t \quad (2.33)$$

The solution will be periodic in  $x$  and  $t$ ; for example,

$$w = \cos kx \operatorname{Re} \{ W(z) e^{i\omega t} \}$$

$$u = \sin kx \operatorname{Re} \{ U(z) e^{i\omega t} \}$$

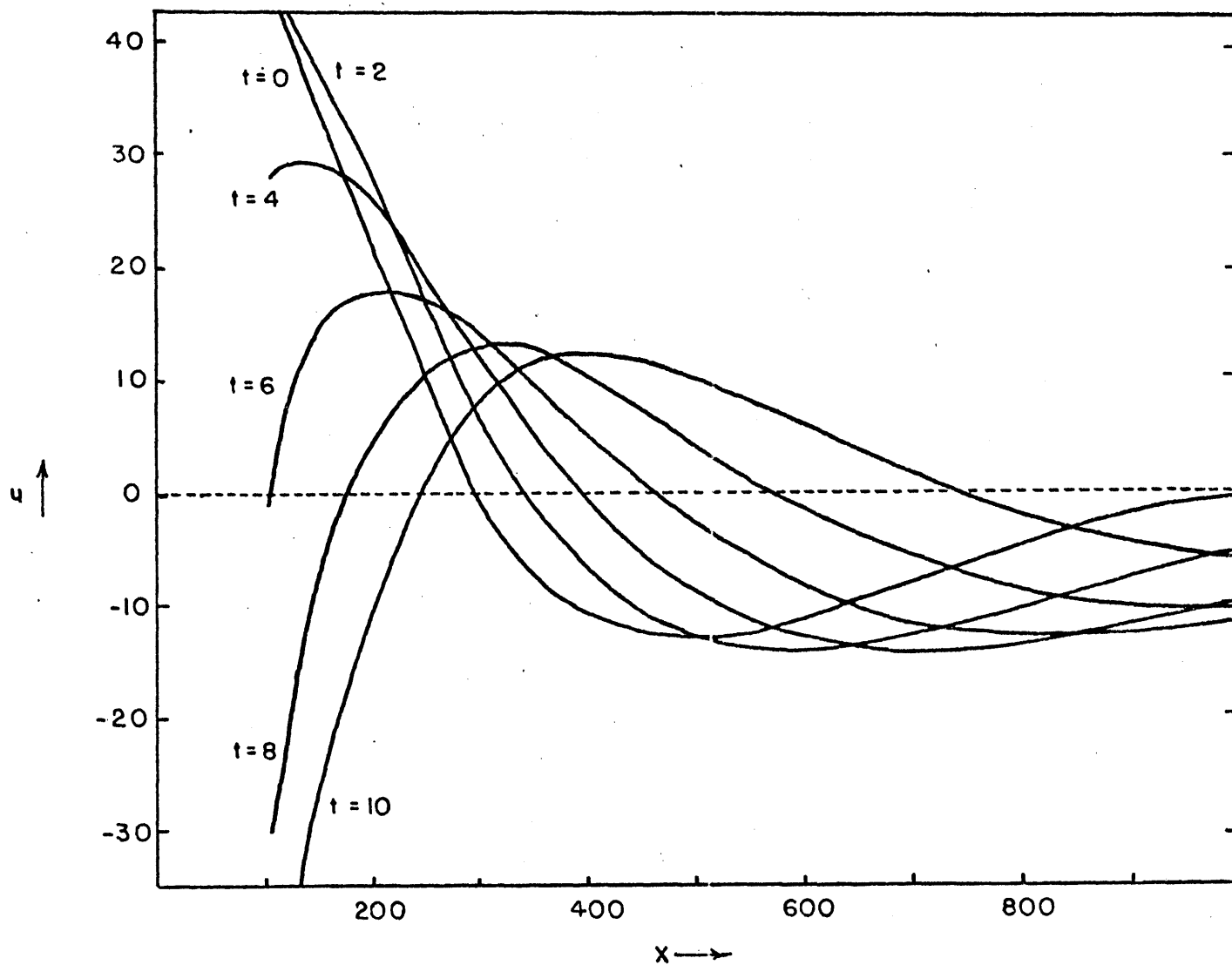


Figure 2.9a.  $u$  component of the velocity at  $z = 4$  for the case of  $\frac{f}{\omega} = 0.5$ ,  $N^2 = 10^{-4} \text{ sec}^{-2}$ ,  $U = 0$ ;  $x$  is nondimensional,  $t$  is in hours. Velocities ( $\text{cm sec}^{-1}$ ) are scaled using  $b_{\text{max}} = 9.8 \text{ cm sec}^{-2}$ .

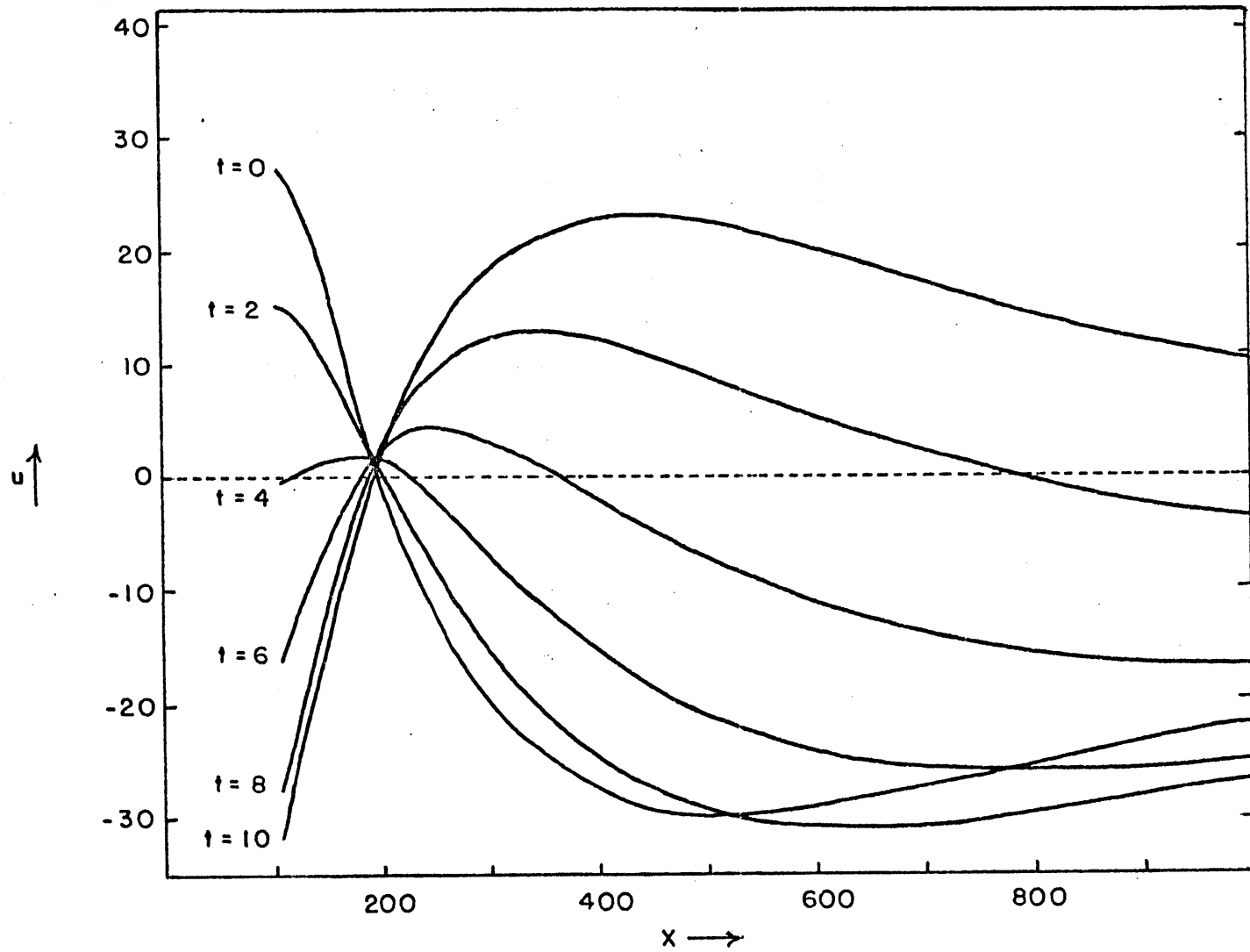


Figure 2.9b. Same as figure 2.9a but for  $\frac{f}{\omega} = 1.0$ .

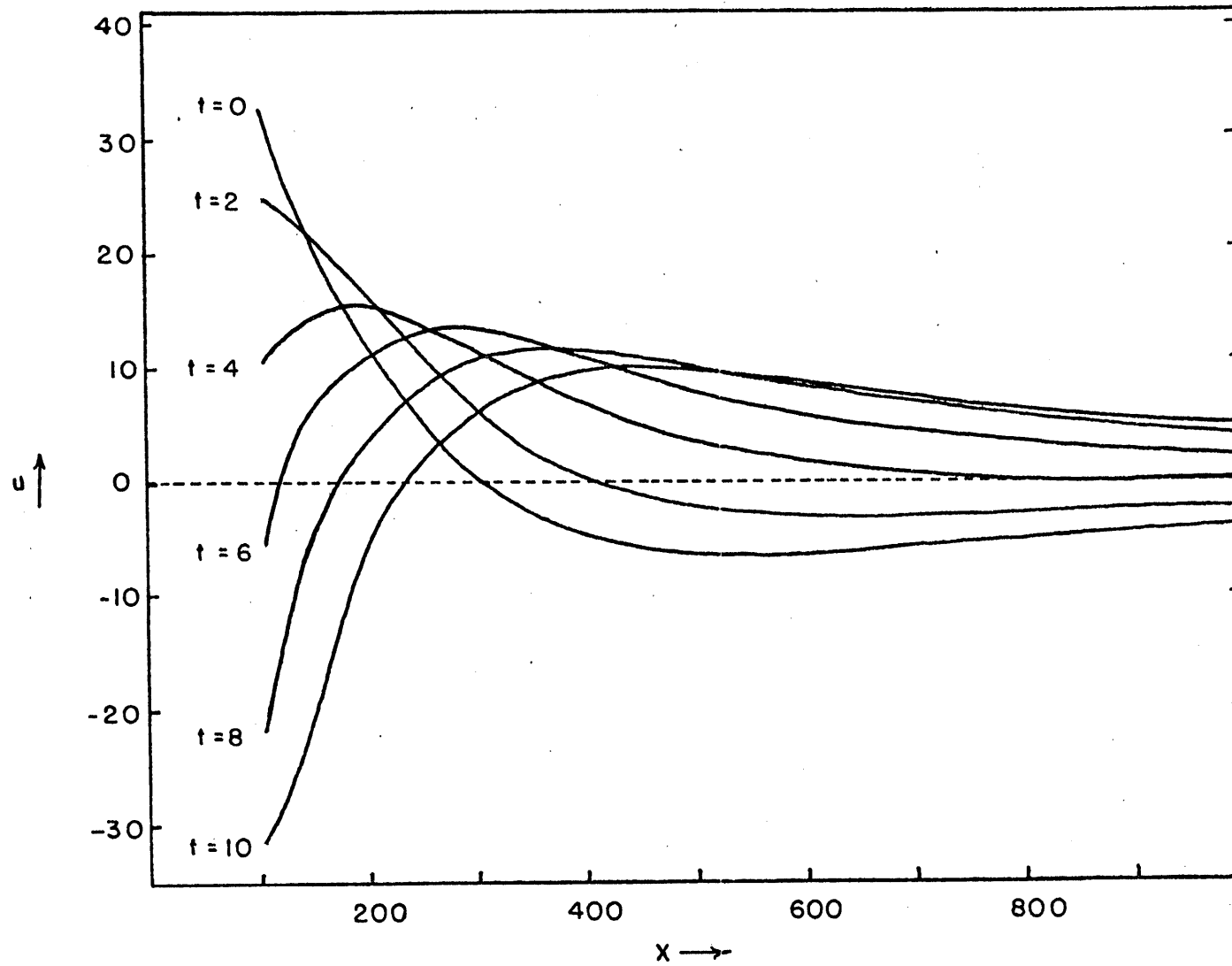


Figure 2.9c. Same as figure 2.9a but for  $\frac{f}{\omega} = 1.5$ .



The differential equation for  $W$  is

$$\frac{d^2 W}{dz^2} + k^2 \left( \frac{N^2 - \omega^2}{\omega^2 - f^2} \right) W = 0$$

Boundary conditions, in addition to (2.33), are that the solutions remain finite as  $z \rightarrow \infty$  and that the energy propagate upwards. The form of the solution depends on the relative magnitudes of  $f$ ,  $\omega$ , and  $N$ . The  $u$  component of the velocity, obtained from  $w$  by the continuity equation, is

$$\underline{\omega < f < N}$$

$$u = W_0 \frac{\gamma}{k} \sin kx e^{-\gamma z} \sin \omega t$$

$$\gamma = k \sqrt{\frac{N^2 - \omega^2}{f^2 - \omega^2}}$$

$$\underline{f < \omega < N}$$

$$u = -W_0 \frac{\gamma}{k} \sin kx \cos(\gamma z + \omega t)$$

$$\gamma = \sqrt{\frac{N^2 - \omega^2}{\omega^2 - f^2}}$$

It is apparent that the vertical wave number becomes undefined as  $f \rightarrow \omega$ . When  $\omega < f < N$ ,  $u \rightarrow 0$  at a fixed  $z$  as  $\omega \rightarrow f$ . However, when  $f < \omega < N$ ,  $u \rightarrow \infty$  as  $\omega \rightarrow f$ . Viscosity will evidently limit the magnitude of  $u$  at the inertial latitude. The velocities computed from the viscous equations show the strongest latitude dependence at large  $z$  because friction plays a more important role near the surface. This masking effect of friction, together with the other factors that affect sea breeze intensity,

tends to prevent the detection in the atmosphere of larger magnitudes at the inertial latitude.

### 2.3.3 Dependence on $N^2$

The effect of the stability on the low-level flow is illustrated in figure 2.10, which shows  $u(x)$  at  $z = 0.33$  when the horizontal winds are well developed,  $t = 8$  hours. The coriolis parameter is  $\frac{f}{\omega} = 1.5$ , and a basic current is not included; curves are sketched for five values of  $N^2$ .

Near the coastline, the winds are strongest when the stability is weakest ( $N^2 = 10^{-5} \text{ sec}^{-2}$ ). This suggests that the observed weakness of the land breeze may be attributed to the higher nighttime stability of the atmosphere.

Figure 2.10 also shows that  $u$  decreases more rapidly with  $x$  when the stability is weaker. By  $x \approx 60$ ,  $u$  actually increases slightly with  $N^2$ . The larger magnitudes of  $\frac{\partial u}{\partial x}$  when  $N^2$  is small are associated with large values of  $w$ , as required by the continuity equation.

Physically, a nearly unstable stratification ( $N^2 = 10^{-5} \text{ sec}^{-2}$ ) offers little resistance to motion in the vicinity of the temperature discontinuity, so most of the potential energy is released near  $x = 0$ . When the stratification is stable, the atmosphere resists vertical motion, so  $w$ ,  $\frac{\partial w}{\partial z}$ , and  $\frac{\partial u}{\partial x}$  are small; winds therefore weaken less rapidly with distance from the coastline.

The tendency for a stable atmosphere to be more "inelastic" results in a more rapid inland propagation of the disturbance when  $N^2$  is large. Figure 2.11 shows the sea breeze onset time as a function of  $N^2$  for four

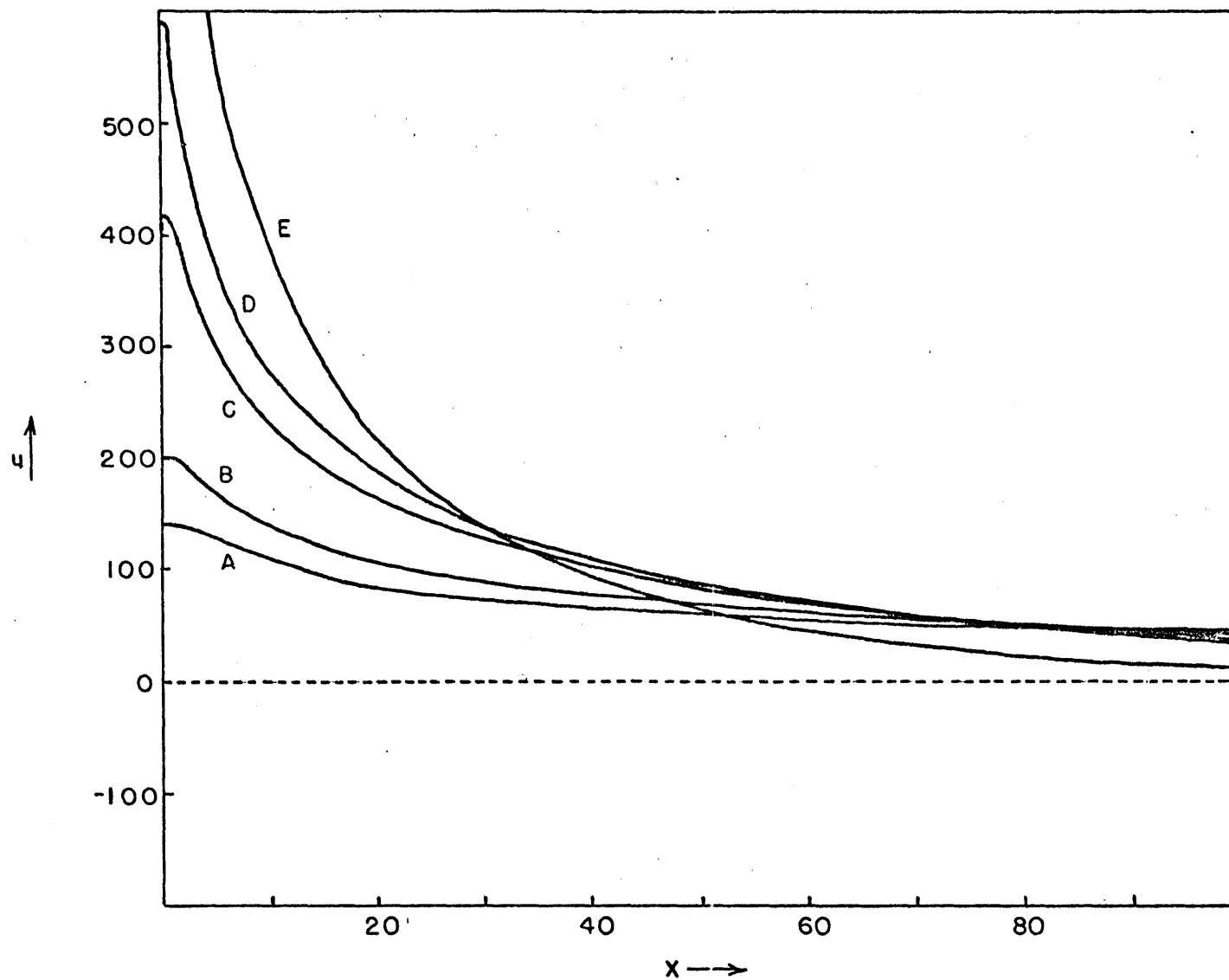


Figure 2.10.  $u$  component of the velocity at  $z = 0.33$ ,  $t = 8$  hours for the case of  $\frac{f}{\omega} = 1.5$ ,  $U = 0$ . Results are shown for  $N^2 =$  A)  $10^{-3}$ , B)  $5 \times 10^{-4}$ , C)  $10^{-4}$ , D)  $5 \times 10^{-5}$ , E)  $10^{-5} \text{ sec}^{-2}$ . Velocities ( $\text{cm sec}^{-1}$ ) are scaled using  $b_{\text{max}} = 9.8 \text{ cm sec}^{-2}$ ;  $x$  is nondimensional.

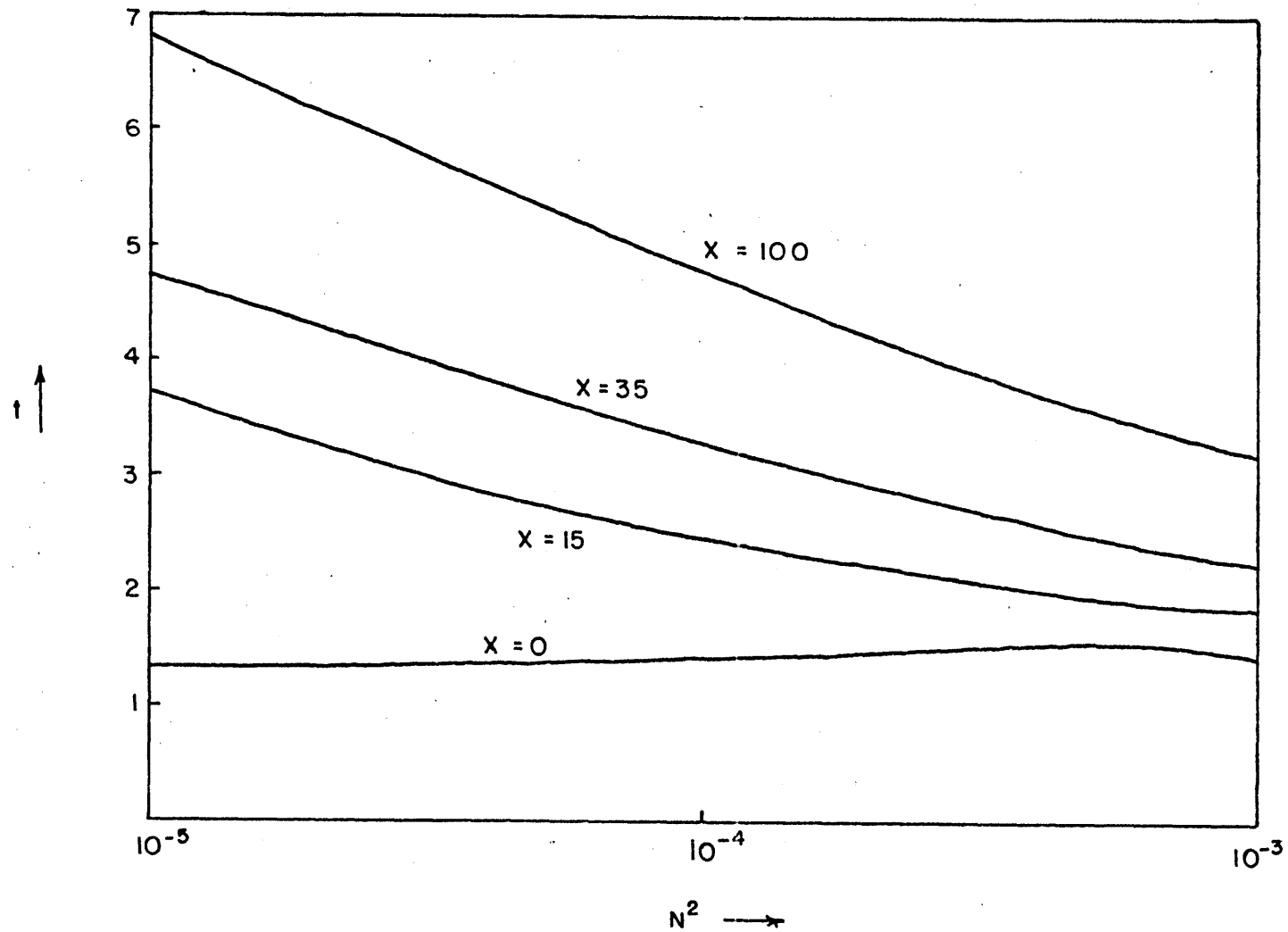


Figure 2.11. Sea breeze onset time (hours after sunrise) for the case of  $\frac{f}{\omega} = 1.5$ ,  $U = 0$ . Results are shown for four nondimensional values of  $x$ ; all curves are for  $z = 0.33$ .

values of  $x$ . The earlier onset time when the stratification is stable is evident at all inland points. The inland extent of the sea breeze, defined as the value of  $x$  at which  $u = 0$  for fixed  $z$  and  $t$ , can therefore be said to increase with increasing  $N^2$ .

The synoptic data mentioned in section 2.3.2 were examined for observational verification of this dependence on  $N^2$ . Since few coastal stations are part of the radiosonde network, the necessary data were available only for Portland, Me. and Charleston, S.C. The quantity used as a stability index was the 1200Z value of  $\frac{\Delta\theta}{\Delta z}$  for the surface-850 mb layer. Since the 850 mb level is near  $z = 6$ , this index is roughly equivalent to a mean  $N^2$  for the sea breeze layer.

The results in table 2.2 show that the onset time correlated negatively with the stability at both stations. The data therefore agree qualitatively with figure 2.11. The value of  $-0.05$  at Portland is too small to be considered significant, but the value of  $-0.40$  at Charleston is significant at the 5% level. Since Charleston is farther inland than Portland, the results support the prediction that the stability dependence of the onset time increases with distance from the coastline.

Conclusions based on this observational study are obviously tentative because only two stations were examined. More importantly, the effect of the gradient wind may contribute to the apparent dependence of the observed onset times on the stability. The most stable stratifications (inversions) generally occur when the gradient wind is calm, and calm conditions favor rapid sea breeze development.

### 2.3.4 Two-layer model

In many sea and lake breeze situations, the assumption of a constant  $N^2$  is unrealistic. The model is now modified to include a discontinuity in  $N^2$ . In the examples to be discussed, inversions will be simulated. The geometry is sketched in figure 2.12.

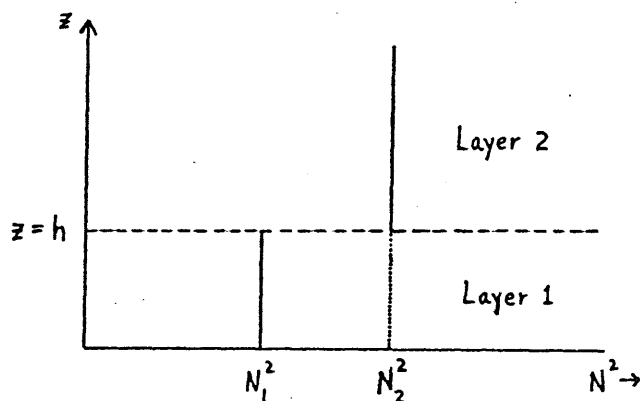


Figure 2.12. Distribution of  $N^2$  in the two-layer model

The equations for each layer are the same as before. In each layer, the  $\bar{\Psi}$  solution consists of six exponentials, while the B solution consists of eight exponentials. Because of the different  $N^2$ , the values of  $\lambda_j$  ( $j=3, \dots, 8$ ),  $b_1$ ,  $b_2$ , and  $\psi_j$  ( $j=3, \dots, 8$ ) are not the same in each layer.

The 16 constants (8 for each layer) are determined by the boundary conditions:

$$z \rightarrow \infty : \quad \bar{\Psi}_2, V_2, P_2, B_2 \text{ finite} \quad (2.34a-2.34d)$$

$$z = 0: \quad W_1 = 0 \Rightarrow \bar{\Psi}_1 = 0 \quad (2.34e)$$

$$U_1 = 0 \Rightarrow \frac{\partial \bar{\Psi}_1}{\partial z} = 0 \quad (2.34f)$$

$$V_1 = 0 \quad (2.34g)$$

$$B_1 = -\frac{1}{\pi k} \quad (2.34h)$$

$$z = h: \quad W_1 = W_2 \Rightarrow \bar{\Psi}_1 = \bar{\Psi}_2 \quad (2.34i)$$

$$U_1 = U_2 \Rightarrow \left( \frac{\partial \bar{\Psi}}{\partial z} \right)_1 = \left( \frac{\partial \bar{\Psi}}{\partial z} \right)_2 \quad (2.34j)$$

$$V_1 = V_2 \quad (2.34k)$$

$$B_1 = B_2 \quad (2.34l)$$

$$P_1 = P_2 \quad (2.34m)$$

$$\left( \frac{\partial U}{\partial z} \right)_1 = \left( \frac{\partial U}{\partial z} \right)_2 \Rightarrow \left( \frac{\partial^2 \bar{\Psi}}{\partial z^2} \right)_1 = \left( \frac{\partial^2 \bar{\Psi}}{\partial z^2} \right)_2 \quad (2.34n)$$

$$\left( \frac{\partial V}{\partial z} \right)_1 = \left( \frac{\partial V}{\partial z} \right)_2 \quad (2.34o)$$

$$\left( \frac{\partial B}{\partial z} \right)_1 = \left( \frac{\partial B}{\partial z} \right)_2 \quad (2.34p)$$

The additional boundary condition at  $z = h$ ,  $\left( \frac{\partial W}{\partial z} \right)_1 = \left( \frac{\partial W}{\partial z} \right)_2$ , becomes the same as (2.34j). (2.34m) is the dynamic boundary condition, while (2.34n) and (2.34o) require that the viscous terms be finite. (2.34p) is, to first order, the requirement that the conductive heat flux be finite at the interface (Ogura and Kondo, 1970). The equations (2.34e)-(2.34p) are solved for the twelve unknown constants. The model can be

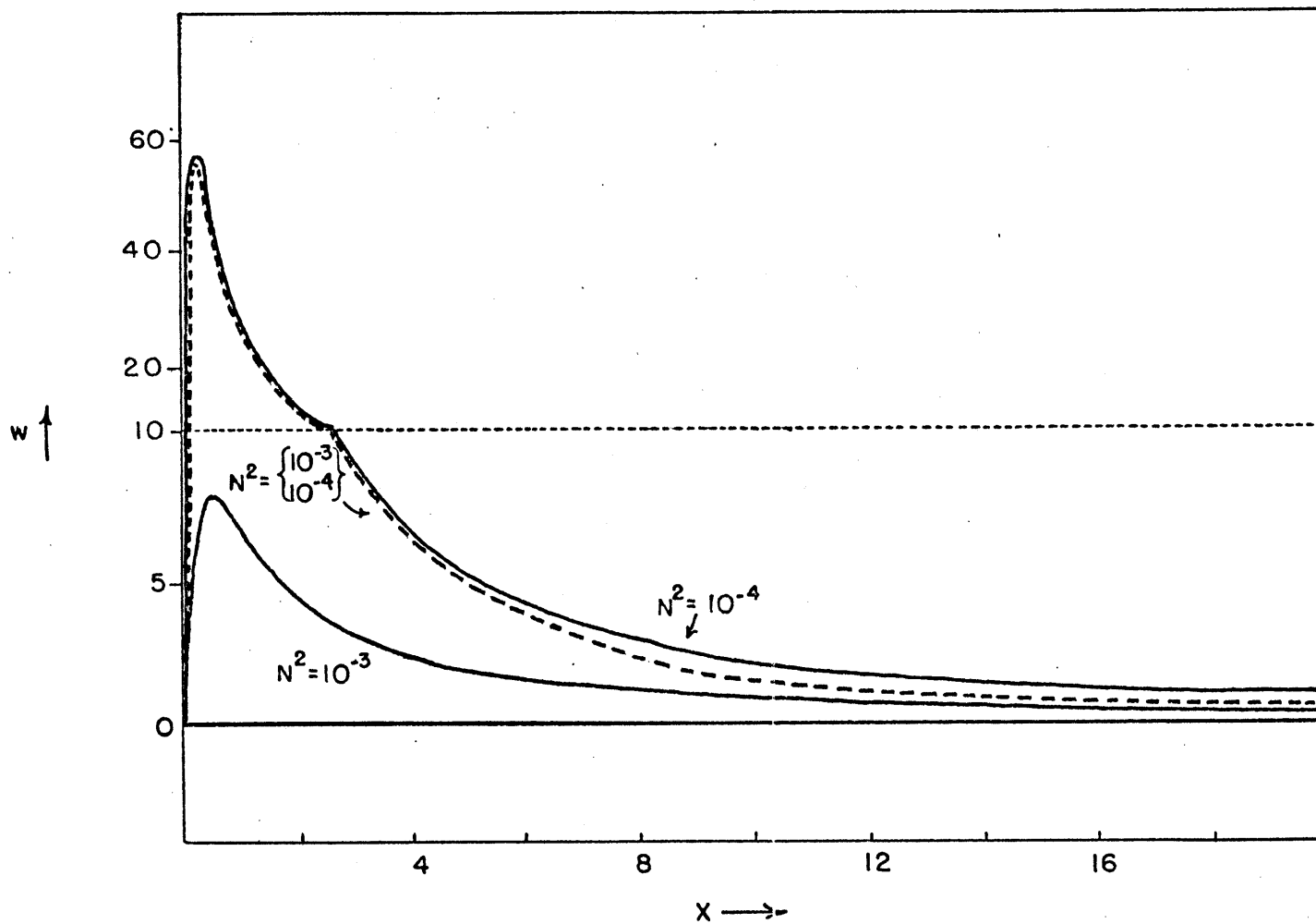


Figure 2.13a.  $w$  component of the velocity at  $z = 0.33$ ,  $t = 6$  hours. Solid curves are for cases of uniform  $N^2$ , dashed curve for two-layer case of  $N_1^2 = 10^{-4} \text{ sec}^{-2}$ ,  $N_2^2 = 10^{-3} \text{ sec}^{-2}$ ,  $h = 1$ ; other parameters are  $\frac{1}{\bar{w}} = 1.5$ ,  $U = 0$ . Velocities ( $\text{cm sec}^{-1}$ ) are scaled using  $b_{\text{max}} = 9.8 \text{ cm sec}^{-2}$ .  $x$  is nondimensional.



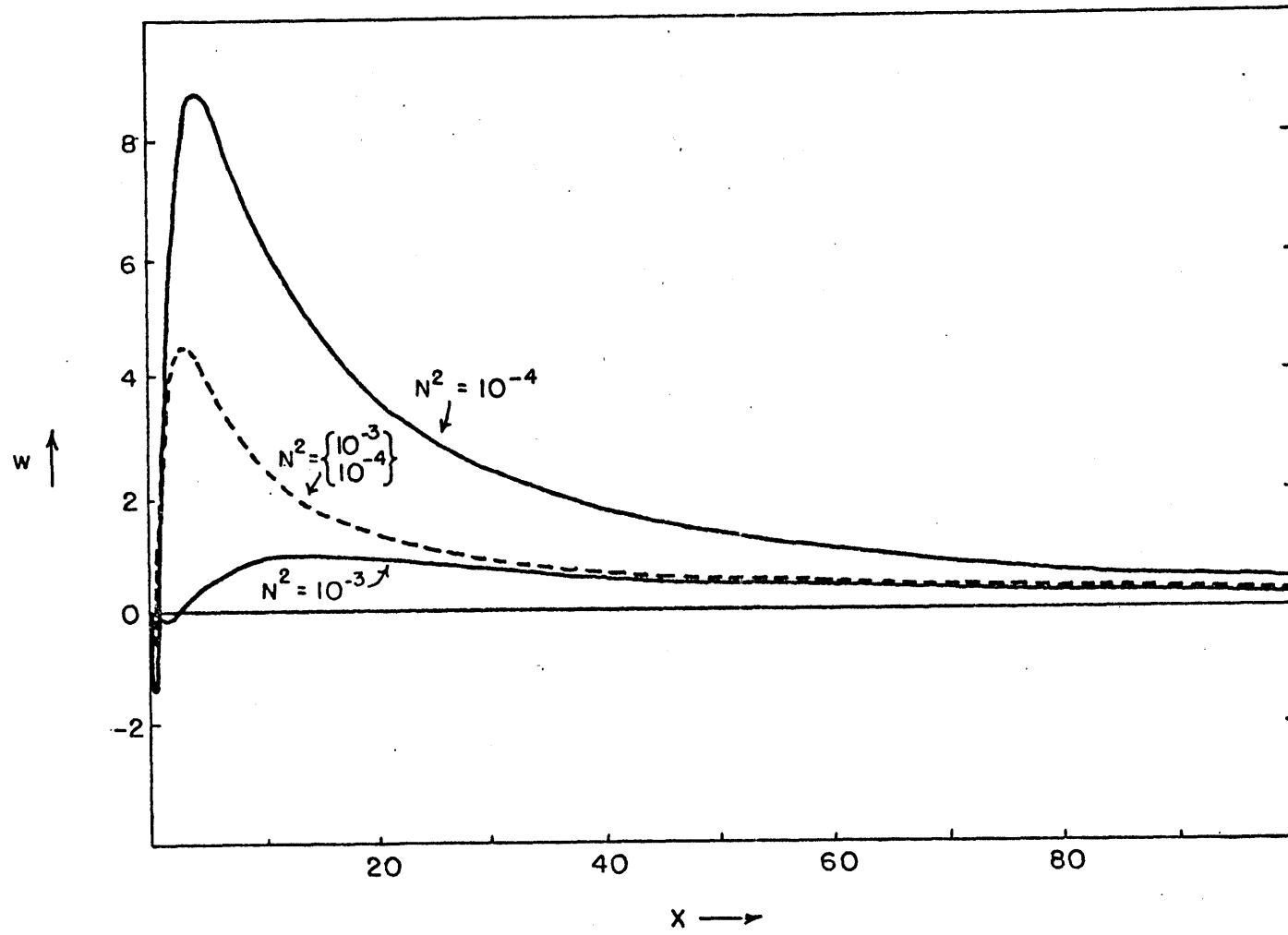


Figure 2.13b. Same as figure 2.13a, but for  $z = 1 = h$ .

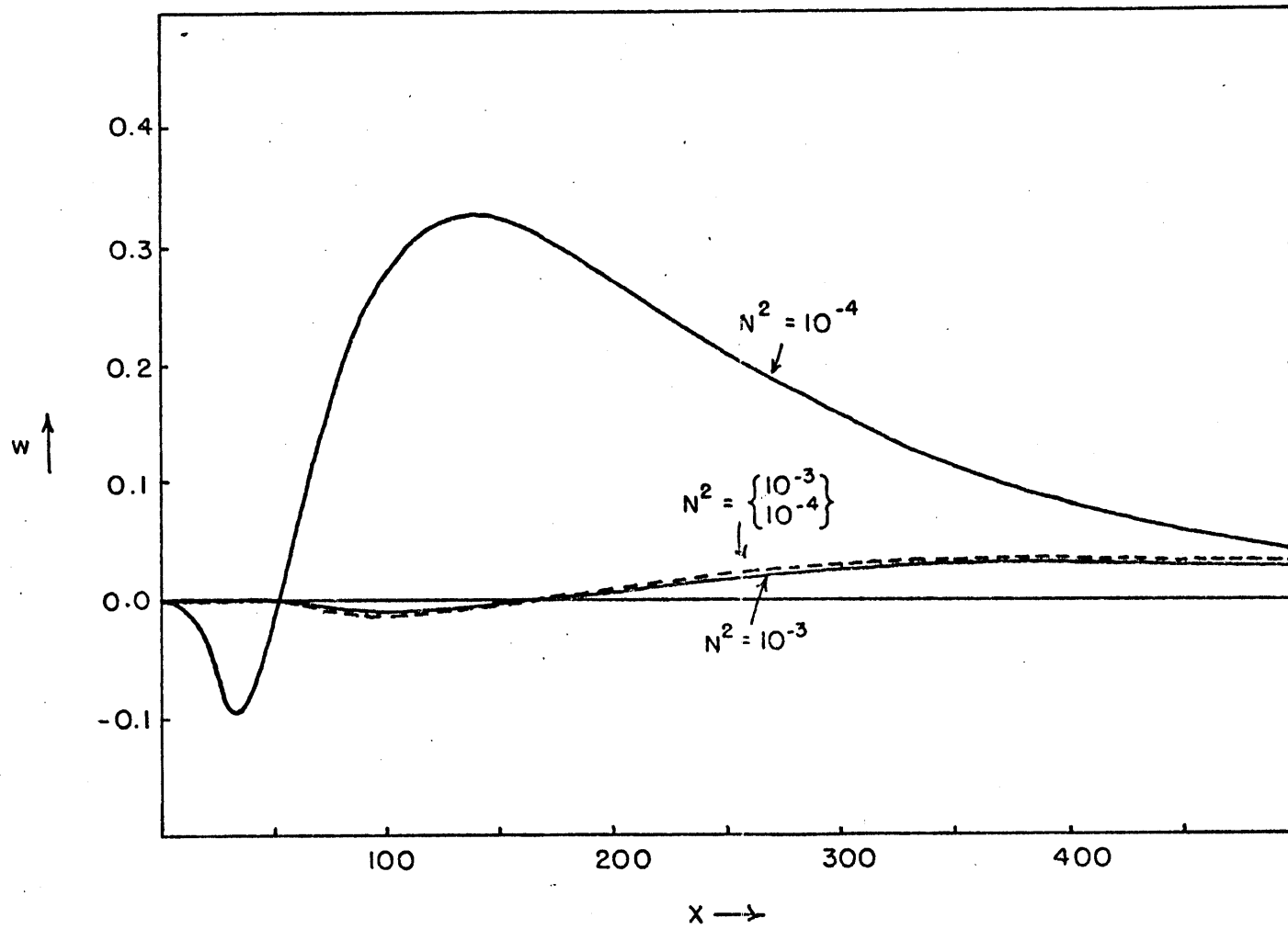


Figure 2.13c. Same as figure 2.13a, but for  $z = 4$ .

extended to include any number of discontinuities in  $N^2$  by introducing the conditions (2.34i)-(2.34p) at each interface.

An arrangement of  $N^2$  typical of the subtropical regions where large-scale subsidence takes place is simulated by setting  $N_1^2 = 10^{-4} \text{ sec}^{-2}$ ,  $N_2^2 = 10^{-3} \text{ sec}^{-2}$ , and  $h = 1$ . The damping effect of the inversion is apparent in figures 2.13a-2.13c, which compare the vertical velocities in the two-layer case to those in the one-layer cases ( $N^2 = 10^{-3}$ ,  $10^{-4} \text{ sec}^{-2}$ ). Near the surface,  $w$  is nearly the same as in the  $N^2 = 10^{-4}$  case, although the damping is apparent at large  $x$  (figure 2.13a). Above the inversion base (figure 2.13c), the vertical velocities are nearly identical to those that occur in the one-layer case with  $N^2 = 10^{-3}$ . At the interface, the values of  $w$  are intermediate between the two one-layer cases (figure 2.13b). The values of  $u$  and  $v$  show similar relations to the constant- $N^2$  cases.

The damping of the onshore sea breeze current is even more apparent when a surface inversion is simulated by setting  $N_1^2 = 10^{-3} \text{ sec}^{-2}$ ,  $N_2^2 = 10^{-4} \text{ sec}^{-2}$ , and  $h = 1$ . This case is discussed in chapter 3 when the vertical heat fluxes are evaluated.

#### 2.4 Results with a basic current

Because of its role in advecting the perturbation quantities, the gradient wind  $U$  cannot be neglected in a study of the sea breeze. It has already been seen (section 2.3) that the absence of advection results in very steep temperature and velocity gradients near the coastline.

In the presence of a basic current, the horizontal velocity will

be given by the vector sum of the perturbation velocity and the basic current. Since the primary goal of this section is to examine the effect of a mean advection,  $U$  is assumed to be independent of height.

#### 2.4.1 Dependence on $U$

Results were computed for the following values of the nondimensional basic current:  $U_{nd} = -50, -100, -175, -250, -325, -400, \text{ and } -500$ . When dimensionalized by the scale factor  $\omega L$ , these represent offshore winds ranging from approximately  $1 \text{ m sec}^{-1}$  to  $10 \text{ m sec}^{-1}$ . By the symmetry of the problem, the results apply to onshore basic currents if the phase is shifted by  $\pi$  and the land-sea relationship is reversed.

Figure 2.14, a sketch of the streamlines when  $U_{nd} = -250$  and  $t = 8$  hours, illustrates several effects of the basic current. In addition to the expected offshore advection of the circulation center, there is an asymmetry in the intensities of the ascending and descending currents. The asymmetry is also evident in figure 2.15, which shows the dependence of the vertical velocity on  $x$  and  $t$ . The updraft, occurring near the coastline, is considerably stronger than the offshore downdraft. As required by the continuity equation, the  $u$  gradient ( $\frac{\partial u}{\partial x}$ ) is steepest near the coastline (figure 2.16b).

These features are suggestive of the sea breeze front, which has been observed when the gradient wind is offshore. Although it has been reproduced in the nonlinear numerical models of Estoque (1962) and McPherson (1968), the sea breeze front has not been detected in previous analytic results. The asymmetric features of figures 2.14-2.16 may be the closest reproduction of a sea breeze front that the linear

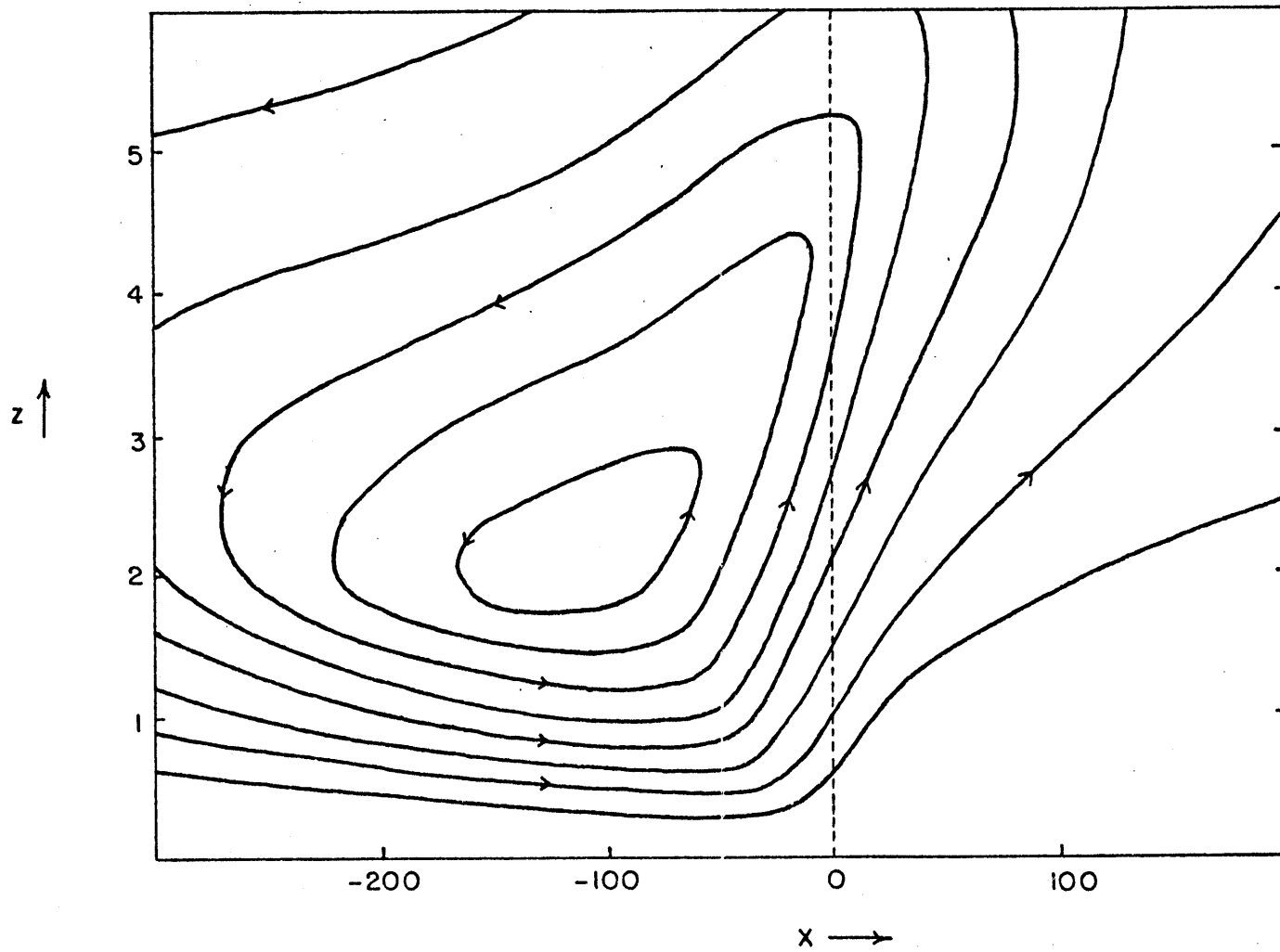


Figure 2.14.  $x$ - $z$  streamlines at  $t = 8$  hours for the case of  $\frac{f}{\omega} = 1.5$ ,  $N^2 = 10^{-4} \text{ sec}^{-2}$ ,  $\frac{U}{\omega L} = -250$ .  
 $x$  and  $z$  are nondimensional.

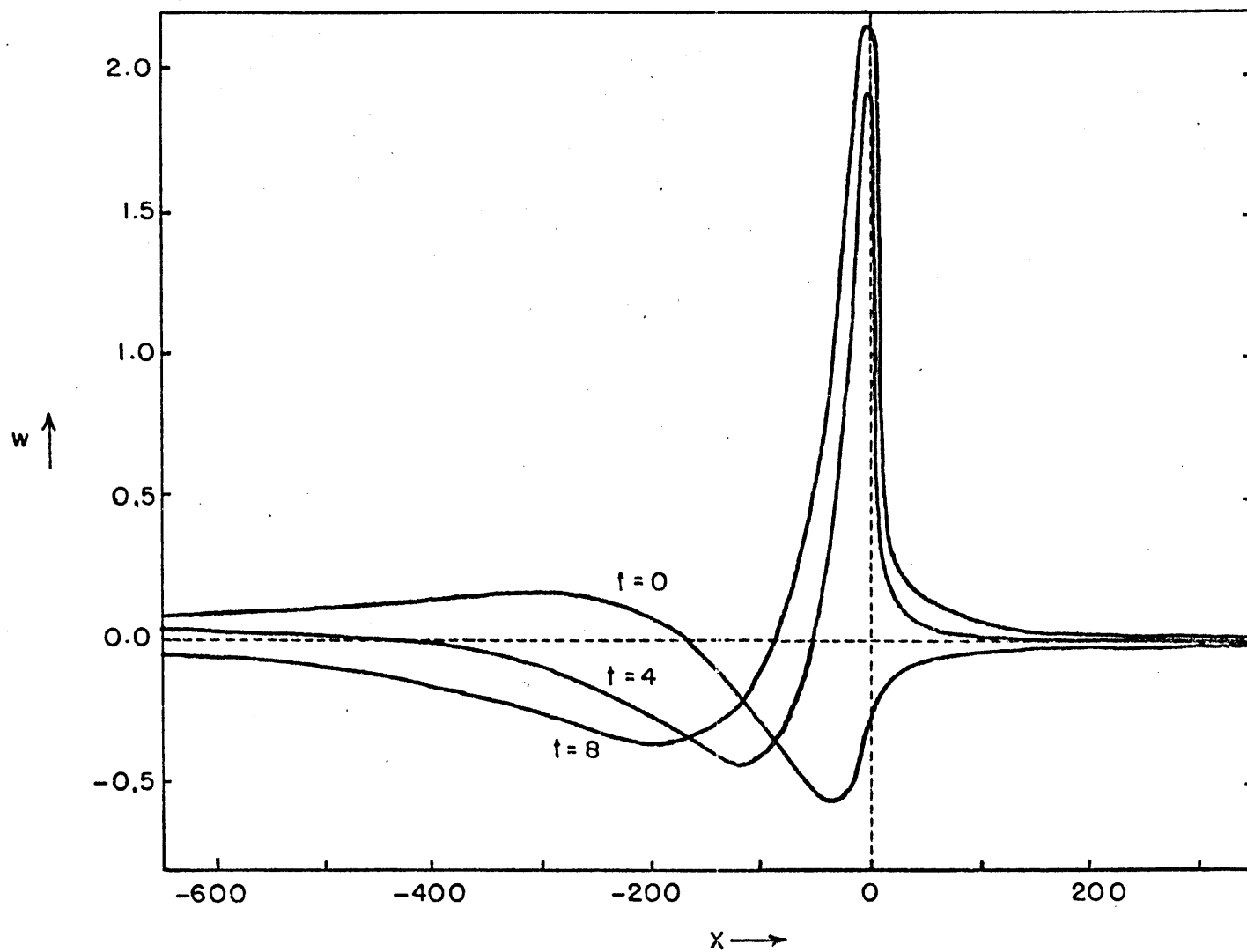


Figure 2.15.  $w$  component of the velocity at  $z = 1$  for the case of  $\frac{f}{\omega} = 1.5$ ,  $N^2 = 10^{-4} \text{ sec}^{-2}$ ,  $\frac{U}{\omega L} = -250$ .  $x$  is nondimensional,  $t$  is in hours. Velocities ( $\text{cm sec}^{-1}$ ) are scaled using  $b_{\text{max}} = 9.8 \text{ cm sec}^{-2}$ .

model will allow, since the periodic time dependence at each point restricts the inland movement of the front.

The asymmetric features of the circulation can be explained qualitatively in terms of the factors affecting the buoyancy. In the offshore downdraft, vertical conduction from below contributes negatively to  $b$ ; this contribution is partially offset by the horizontal advection of positive  $b$  from over the land. As a result, the values of  $b$  and  $w$  are small. In the updraft region, however, horizontal advection and vertical diffusion both contribute positively to  $b$ . The larger values of  $b$  allow stronger vertical motion. The continuity equation then requires that the updraft be narrower than the downdraft.

Figures 2.16a-2.16c show that the peaks of the  $u(x)$  curves are smoothed considerably as  $-U_{nd}$  increases: the maximum  $u$  ( $t = 8$  hours) decreases from  $250 \text{ cm sec}^{-1}$  with  $U_{nd} = -100$  to  $75 \text{ cm sec}^{-1}$  with  $U_{nd} = -400$ . We can conclude that the omission of horizontal advection is responsible for the unrealistic sharpness of the  $u$  and  $w$  curves in figures 2.5 and 2.6.

The dependence of the onshore flow on  $U_{nd}$  can be summarized as follows. At offshore points, the perturbation  $u$  first increases to a maximum as  $-U_{nd}$  increases. As  $-U_{nd}$  becomes still larger, the maximum perturbations occur farther out at sea so that the  $u$  velocities near the coast decrease with increasing  $-U_{nd}$ . At inland points,  $u$  decreases monotonically with increasing  $-U_{nd}$ .

The asymmetric circulation was found to show the same qualitative dependence on  $f$  and  $N^2$  as the symmetric circulation of section 2.3, although these results are not shown here.

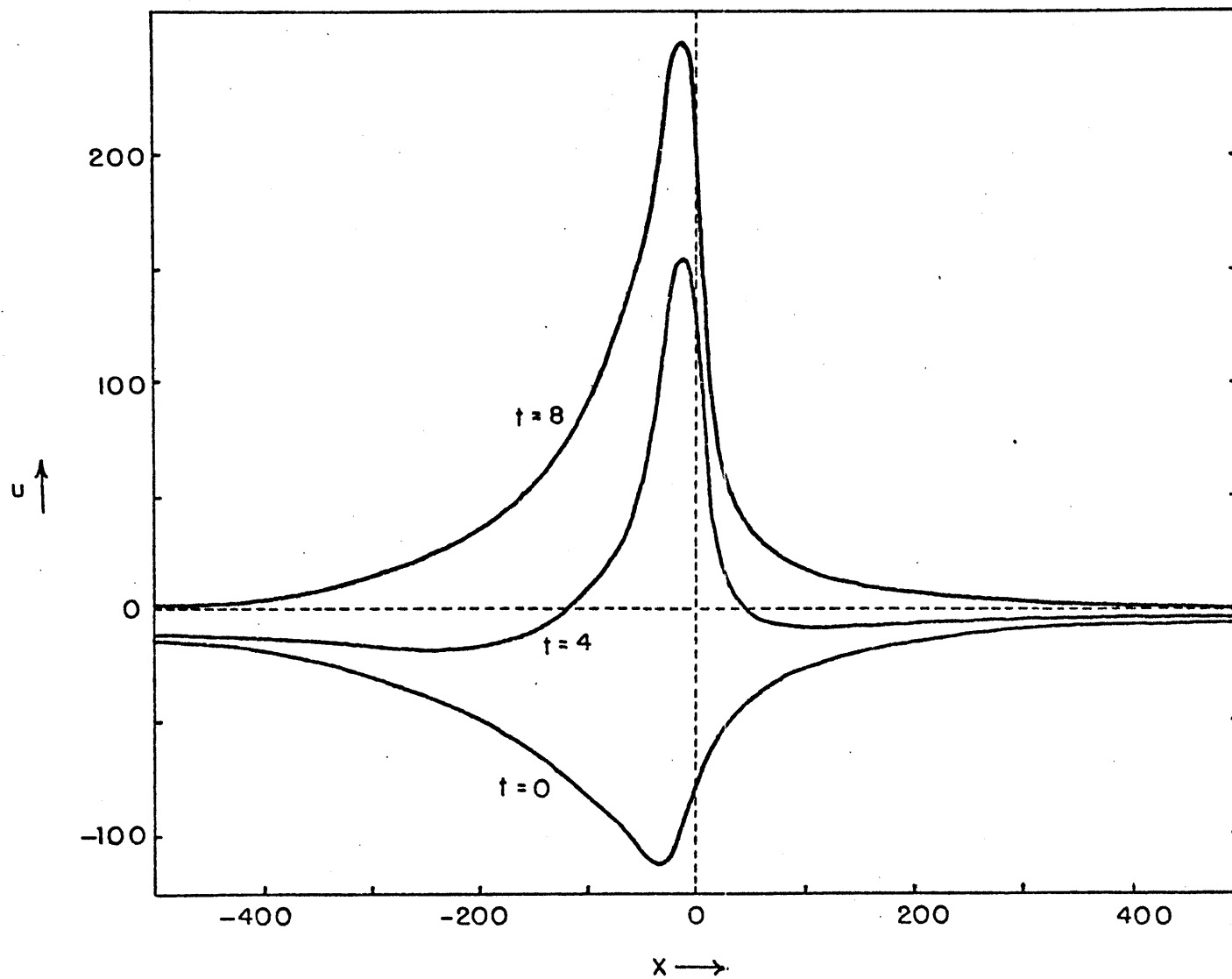


Figure 2.16a.  $u$  component of the velocity at  $z = 0.33$  for the case of  $\frac{f}{\omega} = 1.5$ ,  $N^2 = 10^{-4} \text{ sec}^{-2}$ ,  $\frac{U}{\omega L} = -100$ .  
 $x$  is nondimensional,  $t$  is in hours. Velocities ( $\text{cm sec}^{-1}$ ) are scaled using  $b_{\text{max}} = 9.8 \text{ cm sec}^{-2}$ .



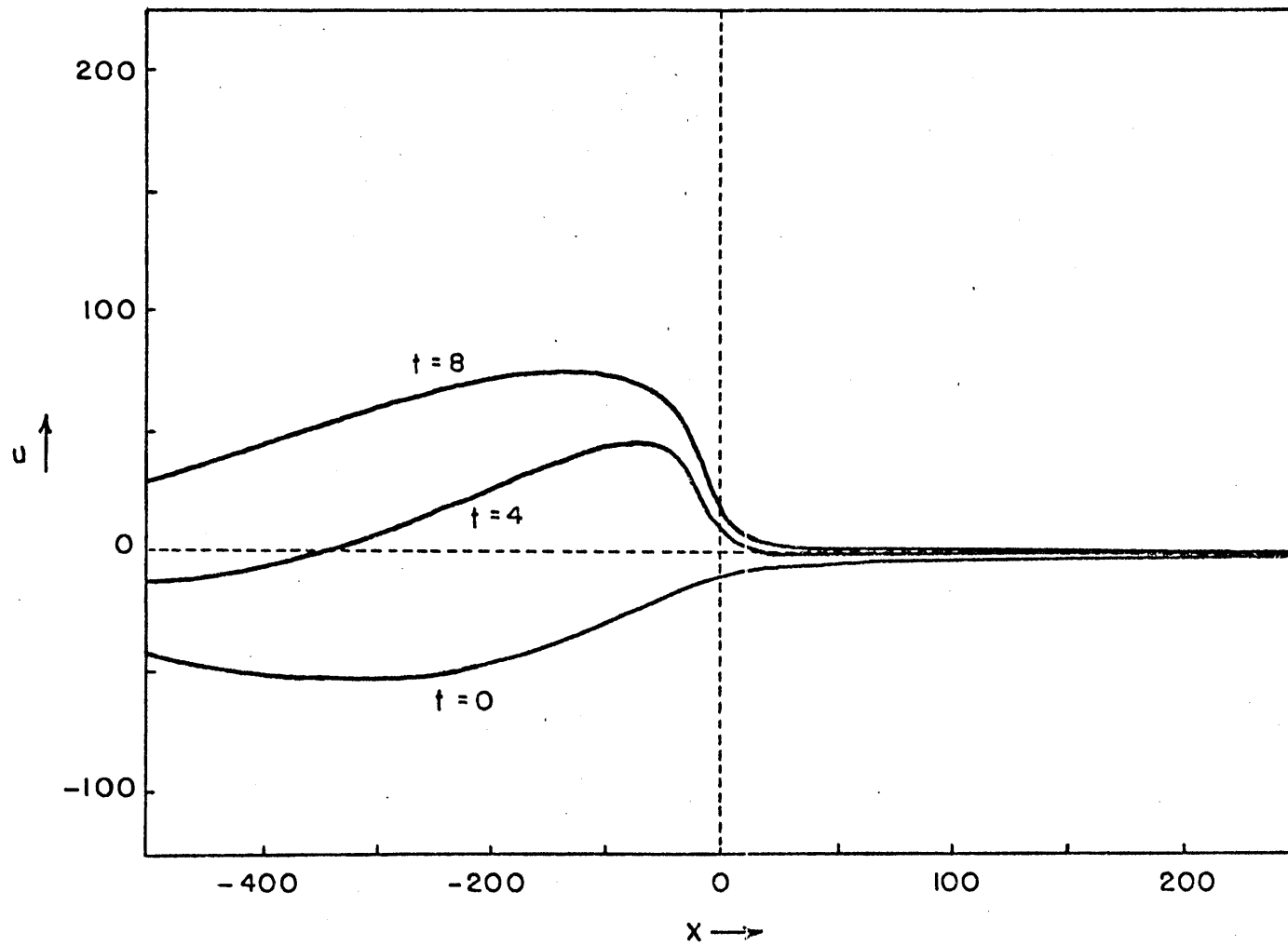


Figure 2.16b. Same as figure 2.16a but for  $\frac{U}{\omega L} = -250$ .

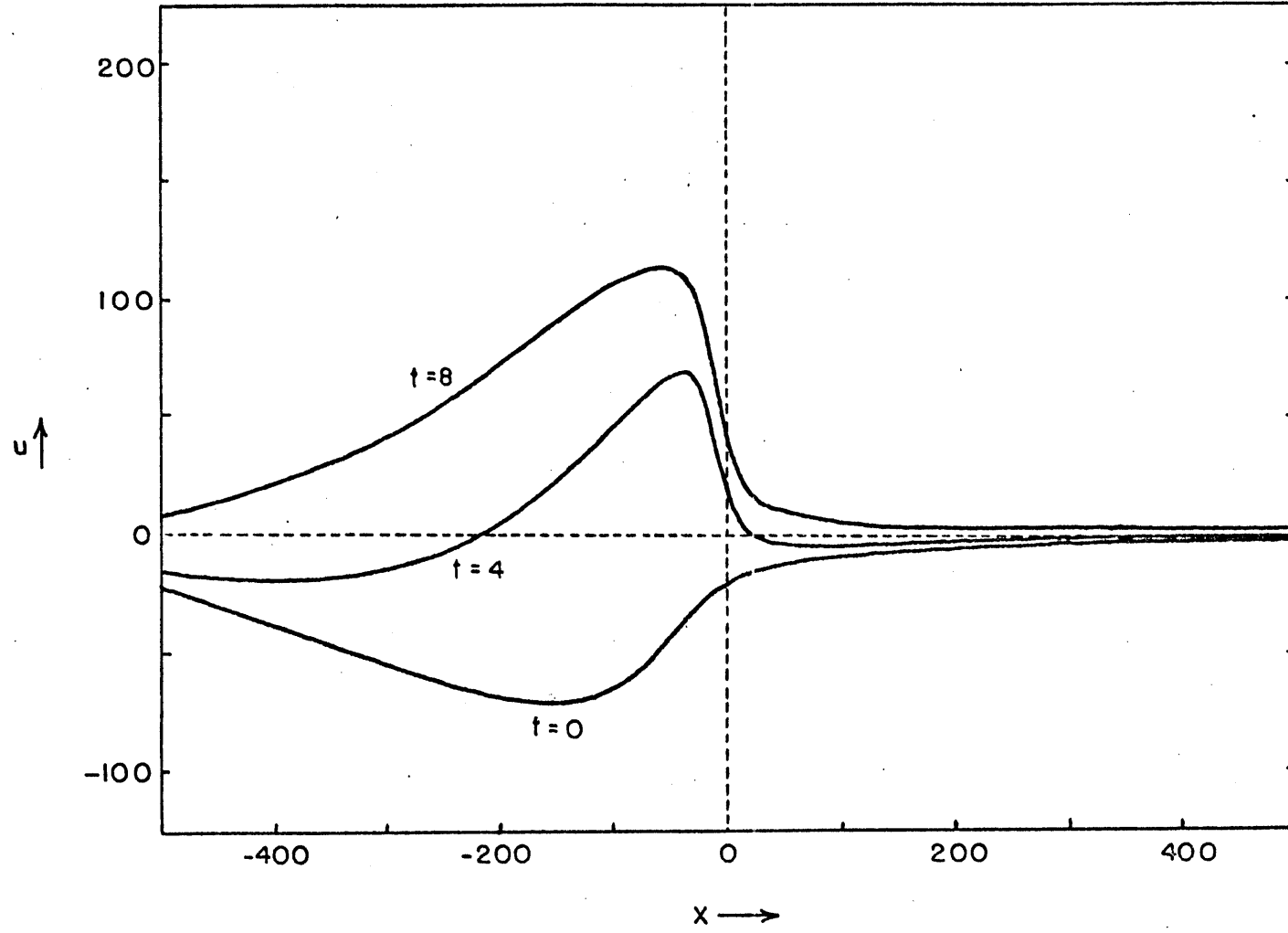


Figure 2.16c. Same as figure 2.16a but for  $\frac{U}{\omega L} = -400$ .

#### 2.4.2 Application to the sea breeze prediction problem

The scaling of the velocity components by  $b_{\max}/\omega$  enables one to determine the land-sea temperature difference that is necessary to create a positive  $u_{\text{total}} = u + U$  at any point for a specified offshore  $U$ . Alternatively, for a given  $\Delta T$ , one can determine the magnitude of the offshore current that is necessary to prevent an onshore flow. Such a relationship between  $U$  and  $\Delta T$  is of practical value in forecasting the occurrence of a sea breeze.

Empirical relations have been developed by using observational data from various coastal stations. Lyons (1972), for example, develops the following criterion for the occurrence of a lake breeze on the western shore of Lake Michigan:

$$(\Delta T)_{\max} > \frac{\epsilon}{2} V_g^2$$

where  $V_g$  is the gradient wind speed ( $\text{m sec}^{-1}$ ) at the surface irrespective of direction and  $(\Delta T)_{\max}$  is the maximum land-water temperature difference in  $^{\circ}\text{C}$ .  $\epsilon$  ( $= \frac{2}{3} \text{ deg m}^{-2} \text{ sec}^{-2}$ ) is an empirically determined constant. For comparison to the results of the linear model, we assume  $V_g = \sqrt{2}V_{\text{gn}}$  to obtain an average component  $V_{\text{gn}}$  normal to the coast. Lyons' relation then becomes

$$(\Delta T)_{\max} > \epsilon V_{\text{gn}}^2 \quad (2.35)$$

In the notation of the model, where  $b_{\max} = \frac{g}{2 T_o} (\Delta T)_{\max}$  and  $V_{\text{gn}} = U$ ,

(2.35) becomes

$$\frac{b_{\max}}{\omega^2 L} > \frac{\epsilon}{2} \frac{g}{T_o} \sqrt{\frac{k}{\omega}} \left( \frac{U}{\omega L} \right)^2 \quad (2.36)$$

The scaling of section 2.2 enables the theoretical criterion  $(u + U)_{x=0} > 0$  to be written as

$$\frac{b_{max}}{\omega^2 L} > \frac{1}{u_{max}} \frac{|U|}{\omega L} \quad (2.37)$$

where  $u_{max}(\frac{f}{\omega}, \frac{N^2}{\omega^2}, \frac{U}{\omega L})$  is the maximum (nondimensional) value of  $u$  obtained in the solution. We ignore the functional dependence of  $u_{max}$  on  $\frac{f}{\omega}$  and  $\frac{N^2}{\omega^2}$  because Lyons' data do not allow such dependence.

Although the sea breeze occurrence criteria are defined for the coastline, (2.37) will be interpreted using the maximum value of  $u$  even if it occurs offshore. This choice of  $u_{max}$  anticipates the nonlinear self-advection of the disturbance. Tests in chapter 4 verify the intuitive idea that the self-advection does displace  $u_{max}$  back to the coastline.

A physical interpretation for the parameter  $\epsilon$  can be obtained by equating the right hand sides of (2.36) and (2.37). The result is

$$u_{max} \frac{|U|}{\omega L} = \frac{2}{\epsilon} \frac{T_o}{g} \sqrt{\frac{\omega}{K}} = C \quad (2.38)$$

where  $C$  is a constant independent of the nondimensional basic current. Figure 2.17 shows that  $u_{max} \frac{|U|}{\omega L}$  is indeed nearly constant except at small  $|U|$ , where the vanishing of  $|U|$  requires that the product also vanish. Using the asymptotic value for  $C$  of 0.22 (figure 2.17), solving (2.38) for  $\epsilon$ , and substituting the result for  $\epsilon$  into the empirical criterion gives

$$(\Delta T)_{max} > \frac{T_o}{.11g} \sqrt{\frac{\omega}{K}} U^2 \quad (2.39)$$

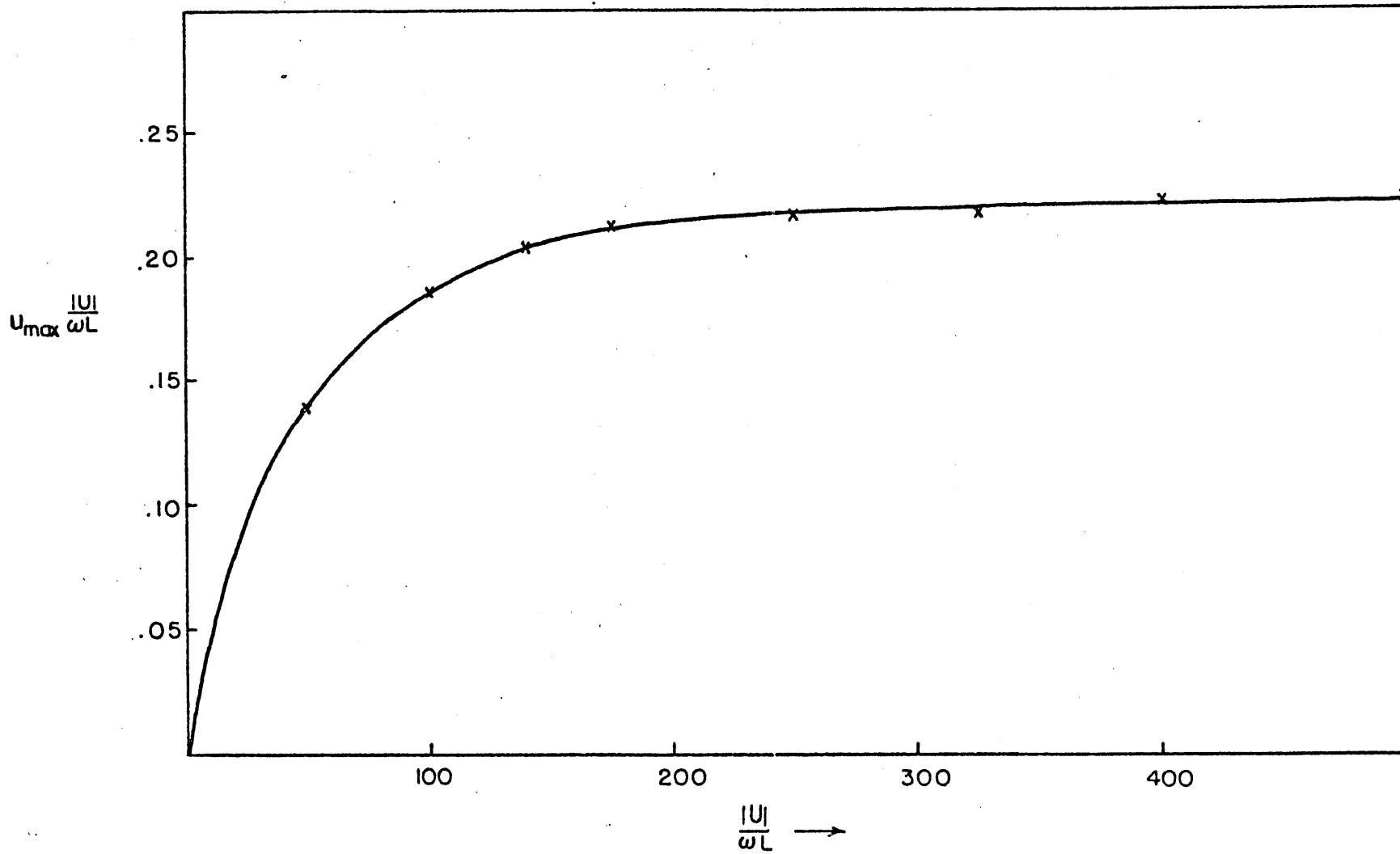


Figure 2.17. The product  $u_{\max} \frac{|U|}{\omega L}$  as a function of  $\frac{|U|}{\omega L}$ ;  $\frac{f}{\omega} = 1.5$ ,  $N^2 = 10^{-4} \text{ sec}^{-2}$ .

According to (2.39), the critical  $(\Delta T)_{\max}$  increases as the forcing frequency increases. Physically, a rapidly oscillating forcing function implies that there is little time for the circulation to increase in intensity by the potential  $\rightarrow$  kinetic energy conversion. Therefore, if a critical perturbation velocity is to develop, there must be a large amount of "available potential energy", or a large  $(\Delta T)_{\max}$ . (2.39) also implies that an increase in the eddy conduction coefficient  $\kappa$  decreases the critical  $(\Delta T)_{\max}$ . This latter result follows from the fact that conduction is the process which creates available potential energy for the sea breeze circulation.

When the computed asymptotic value of  $C$  ( $=0.22$ ) and the observed value of  $\epsilon$  ( $= 2/3 \text{ deg m}^{-2} \text{ sec}^{-2}$ ) are substituted into (2.38), the diffusion coefficient most appropriate to the daytime phase of the Chicago lake breeze can be evaluated. The result,  $\kappa = 1.1 \times 10^5 \text{ cm}^2 \text{ sec}^{-1}$ , agrees very well with the daytime eddy diffusivity of  $10^5 \text{ cm}^2 \text{ sec}^{-1}$  suggested by Kuo (1969) and Yoshikado and Asai (1972).

The theoretical prediction criterion based on  $\kappa = 10^5 \text{ cm}^2 \text{ sec}^{-1}$  is compared to Lyons' criterion in figure 2.18. The linear model requires a slightly larger  $(\Delta T)_{\max}$  for  $U \leq 6 \text{ m sec}^{-1}$  and a slightly smaller  $(\Delta T)_{\max}$  for  $U \geq 6 \text{ m sec}^{-1}$ , although the latter portion of the curve is not shown because both criteria require such large values of  $(\Delta T)_{\max}$  for  $U \geq 6 \text{ m sec}^{-1}$  that sea breezes will rarely occur. For all  $U \leq 10 \text{ m sec}^{-1}$ , the curves agree to within  $1 \text{ C}^\circ$ . It is to be noted that the use of a mean  $\kappa$  based on observed data assures only a "mean" agreement between the theoretical and empirical curves over the range  $U \leq 10 \text{ m sec}^{-1}$ . Such a value of  $\kappa$  does not guarantee that the two curves will agree as closely as they do

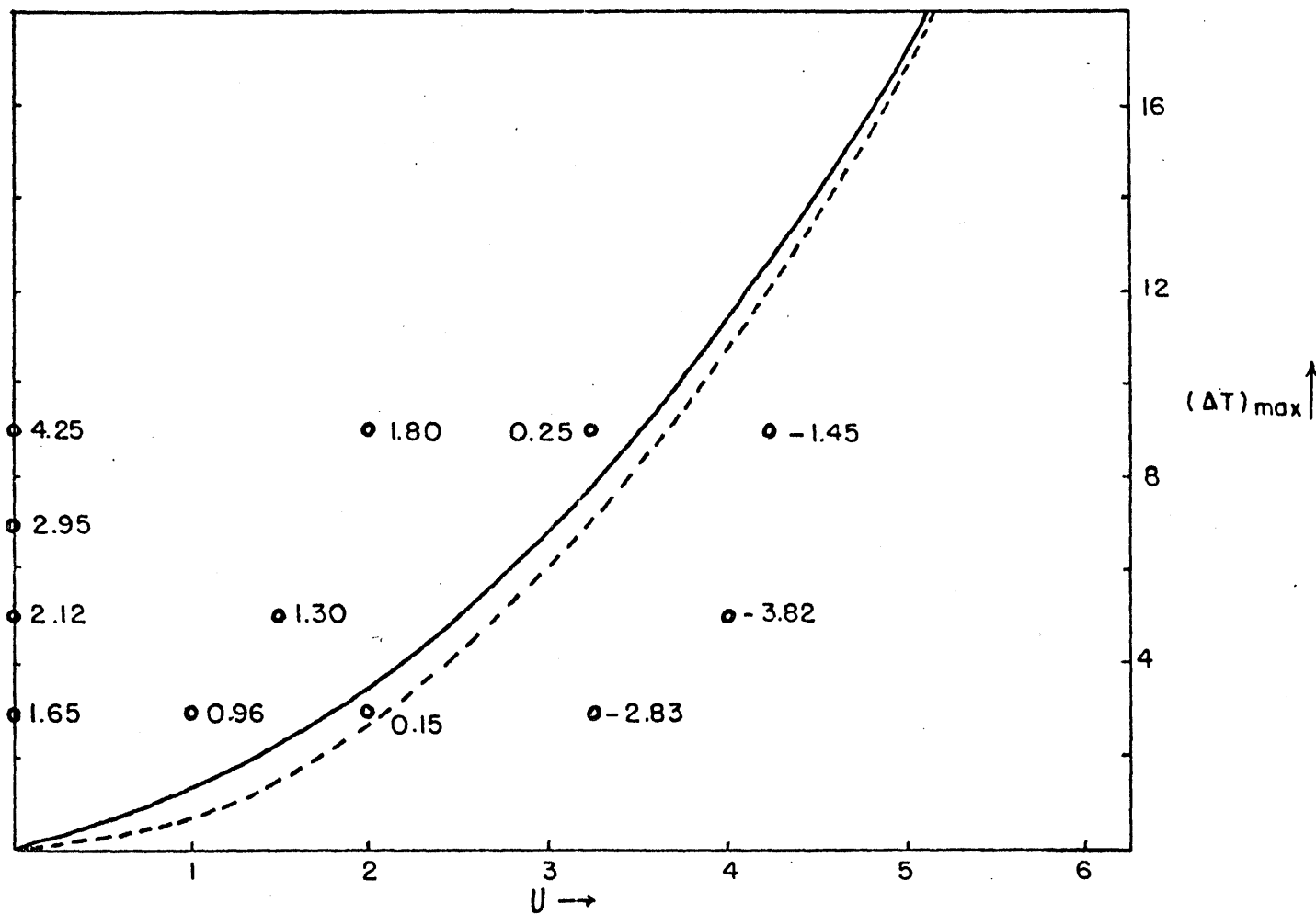


Figure 2.18. The critical land-sea temperature difference  $\Delta T$  ( $^{\circ}\text{C}$ ) required for sea breeze occurrence.  $U$  ( $\text{m sec}^{-1}$ ) is scaled using  $\kappa = 10^5 \text{ cm}^2 \text{ sec}^{-1}$ . Solid curve is the linear criterion (see text), dashed curve is based on Lyons' data. Numbers accompanying circles are the values of  $(U+u)_{\text{max}}$  in the region  $x \geq 0$  based on the nonlinear integrations of chapter 4; positive values indicate sea breeze occurrence.

at each value of  $U$ . One may therefore conclude that the model provides theoretical support for the observed linear relationship between  $U^2$  and the critical  $(\Delta T)_{\max}$ .

Pearson (1973) has recently reported results from an inviscid non-conductive numerical model in which no basic current is present and in which the heating is specified as a function of space and time. He obtained the following relationship between the "total heat transfer"  $H_1$  (in  $\text{m}^2 \text{sec}^{-2}$ ) and the speed  $V_f$  (in  $\text{m sec}^{-1}$ ) of the sea breeze front:

$$V_f = .49 \sqrt{H_1 - 22.0} \quad (2.40)$$

(2.40) is considered valid in the range  $40 < H_1 < 120 \text{ m}^2 \text{sec}^{-2}$ . A relation based on the linear results of this section is obtained from (2.38):

$$|U_{\text{crit}}| = .34 \sqrt{H_2} \quad (2.41)$$

where  $H_2 = \sqrt{\frac{k}{w}} g \frac{(\Delta T)_{\max}}{T_0}$  and  $U_{\text{crit}}$  is the gradient wind for the "critical case" in which the (onshore) perturbation flow is just strong enough to balance the (offshore) gradient wind. Although Pearson states that  $V_f$  was not correlated with the maximum velocity  $u_{\max}$ , his results can be compared to the results of this study if one assumes that his "critical case" is given by  $|U_{\text{crit}}| = V_f$ . Figure 2.19 shows that (2.40) and (2.41) then predict critical gradient wind speeds which differ by less than  $1 \text{ m sec}^{-1}$ , although Pearson's critical speeds are larger for all  $H \geq 45 \text{ m}^2 \text{sec}^{-2}$ . This difference is most likely due to the omission of viscosity in Pearson's computations of  $V_f$ .



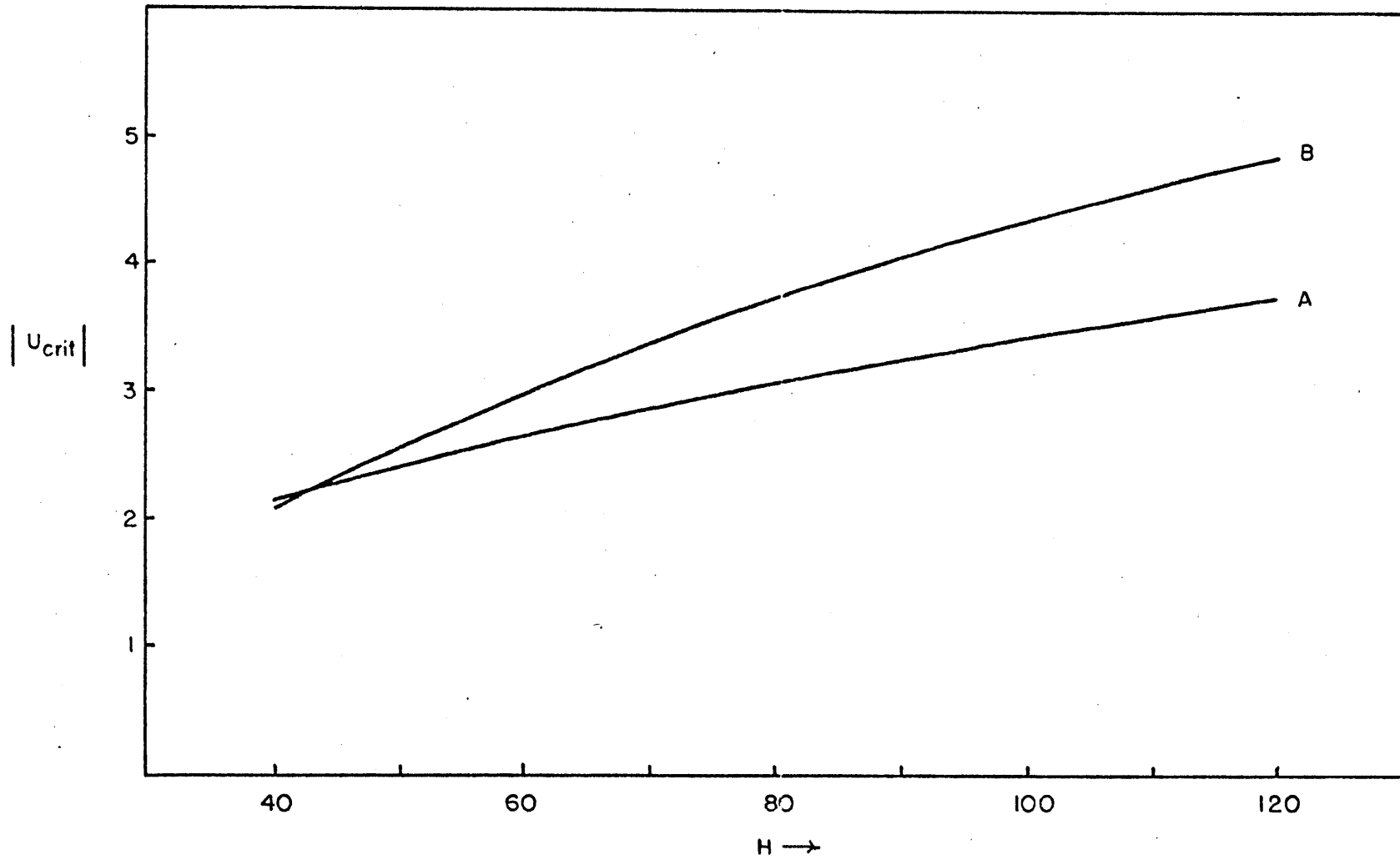


Figure 2.19. The critical gradient wind speed  $|U_{crit}|$  in  $m \text{ sec}^{-1}$  based on the linear results (curve A) and the critical gradient wind speed deduced from Pearson's results (curve B).  $H$  is the total heat input in  $m^2 \text{ sec}^{-2}$ .

### 3. HEAT FLUX CALCULATIONS

The mechanism by which the sea breeze generates kinetic energy is the rising of warm air and the sinking of cool air. The net upward heat flux is therefore a measure of the kinetic energy generated by the circulation. By comparing the fluxes associated with the sea breeze and other atmospheric circulations, one can assess the importance of the sea breeze as a feature of the general circulation.

#### 3.1 Formulation

The time-averaged vertical heat flux along a unit distance of coastline is given by

$$F = \frac{1}{2\pi} \int_0^{2\pi} dt \int_{-\infty}^{\infty} \rho C_p w' T' dx \quad (3.1)$$

Using the definition  $b' = g \frac{T'}{T_0}$ , assuming constant  $\rho$ ,  $C_p$ , and  $T_0$ , and dropping the primes, one obtains

$$\begin{aligned} F &= \frac{1}{2\pi} \frac{\rho C_p T_0}{g} \int_0^{2\pi} dt \int_{-\infty}^{\infty} w b dx \\ &= \frac{1}{2\pi} \frac{\rho C_p T_0}{g} \int_{-\infty}^{\infty} dx \int_0^{2\pi} \operatorname{Re} \{ \tilde{W}(x, z) e^{it} \} \operatorname{Re} \{ \tilde{B}(x, z) e^{it} \} dt \\ \tilde{W}(x, z) &= \int_{-\infty}^{\infty} i \sum_{j=1}^4 k_j \psi_j e^{-\lambda_j z} e^{ikx} dk \\ \tilde{B}(x, z) &= \int_{-\infty}^{\infty} (b_1 e^{-\lambda_1 z} + \sum_{j=2}^4 \alpha_j \psi_j e^{-\lambda_j z}) e^{ikx} dk \\ &= \frac{1}{\pi} \frac{\rho C_p T_0}{g} \int_0^{2\pi} dx \int_0^{2\pi} (w_{t=0} \cos t + w_{t=\frac{\pi}{2}} \sin t) (b_{t=0} \cos t + b_{t=\frac{\pi}{2}} \sin t) dt \end{aligned}$$

where the last step assumes symmetry about  $x = 0$ . Evaluation of the

time integrals then gives

$$F = \frac{\rho C_p T_0}{g} \int_0^{\infty} (w_{t=0} b_{t=0} + w_{t=\frac{\pi}{2}} b_{t=\frac{\pi}{2}}) dx \quad (3.2)$$

When a basic current is present, the asymmetry requires that the lower limit of integration be extended to  $x = -\infty$ . In CGS units,  $\frac{\rho C_p T_0}{g} \approx 3.0 \times 10^3 \text{ g cm}^{-2}$ .

The flux was evaluated at five values of  $z$  for the case of  $U = 0$ ,  $\frac{f}{\omega} = 1.5$ , and  $N^2 = 10^{-4} \text{ sec}^{-2}$ . The results are shown in figure 3.1 as functions of  $x$ , which has replaced the upper limit of integration in (3.2). The levelling off of the curves indicates that convergence is rapid at small  $z$  and only slightly slower at large  $z$ . When the upper integration limit is extended from  $x = 500$  to  $x = 1000$ , the  $z = 4$  integral changes by approximately  $.015 \text{ kj cm}^{-1} \text{ sec}^{-1}$ , while the  $z = .33$  integral changes by  $.008 \text{ kj cm}^{-1} \text{ sec}^{-1}$ . The rapid convergence indicates that the vertical heat flux decreases rapidly with distance from the coastline.

The horizontally integrated flux reaches its maximum value near  $z = 0.67$ , several hundred meters above the surface. It is interesting to note that the flux at  $z = 4$  is slightly negative, implying that the region above  $z = 4$  is forced mechanically by the motion below it. If all  $z$  are considered, the volume integral of the flux is clearly positive, as it must be if there is to be a net conversion of potential to kinetic energy to offset frictional dissipation. The negative flux at  $z = 4$  suggests that the sea breeze (with  $U = 0$ ) is restricted to  $0 \leq z \leq 4$ , or approximately the lowest kilometer.

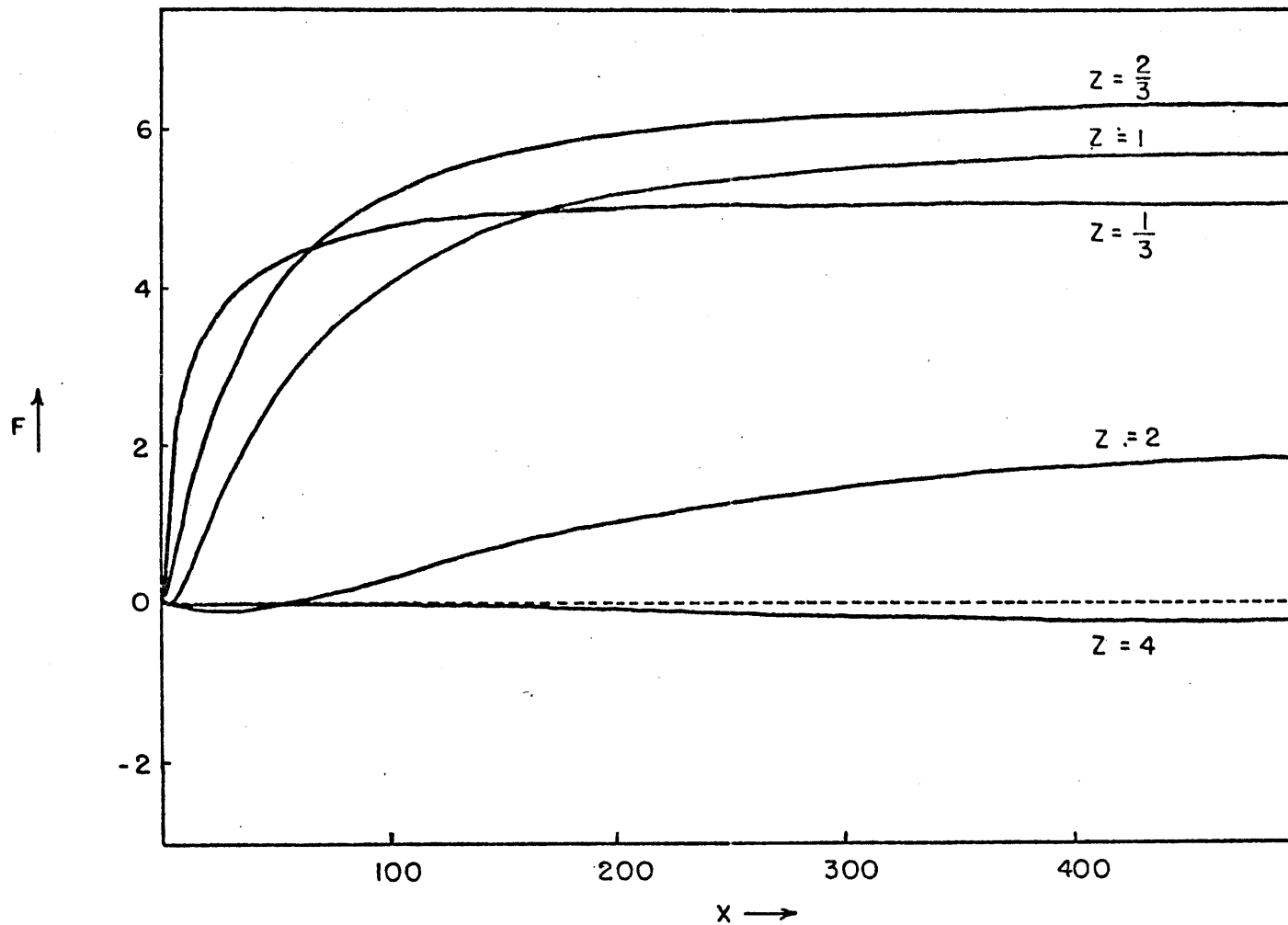


Figure 3.1. The time-averaged vertical heat flux  $F(x) = \frac{\rho C_p T_0}{2\pi g} \int_0^{2\pi} dt \int_{-\infty}^{\infty} wb \, dx$  ( $\text{kJ sec}^{-1} \text{cm}^{-1}$ ) for the case of  $\frac{f}{\omega} = 1.5$ ,  $N^2 = 10^{-4} \text{sec}^{-2}$ ,  $U = 0$ .  $x$  and  $z$  are nondimensional;  $w$  and  $b$  are scaled using  $b_{\text{max}} = 9.8 \text{cm sec}^{-2}$ .

### 3.2 Dependence of the flux on external parameters

Figure 3.2 shows that the heat flux does not vary significantly with  $f$ . The fact that the high-latitude circulation is slightly weaker suggests that rotation acts to reduce the values of  $u$  (and hence  $w$ ) that have been created by the thermal wave.

The sea breeze heat flux depends strongly on  $N^2$  because of the resistance of a stable atmosphere to vertical motion. Figure 3.3 shows that the flux decreases approximately linearly with  $N^2$ . The ratio of the fluxes for any two cases is fairly constant with height up to  $z \approx 3$ , where the fluxes become small.

Figure 3.4 contains the flux curves for the two-layer model of section 2.3.4. In both two-layer cases, the flux curves at large  $z$  become asymptotic to the one-layer case of  $N_2^2$ . The damping effect of the stable layer is apparent in each case, and the flux maximum is shifted upward or downward into the less stable layer. The total heat transport, or the vertical integral of the flux, is smaller when the inversion is aloft. This latter result depends on the height chosen for the discontinuity in  $N^2$ .

The effect of a basic current is illustrated in figure 3.5. The basic current reduces the heat flux and displaces its maximum to a slightly larger value of  $z$ . As suggested in section 2.4, the weakening is attributable to the small offshore values of  $b$  which result from the opposing effects of vertical diffusion and horizontal advection. Since  $U_{nd} = 500$  corresponds to a basic current of about 16 knots, we see that typical gradient winds will reduce the vertical heat flux by approximately a factor of 2.

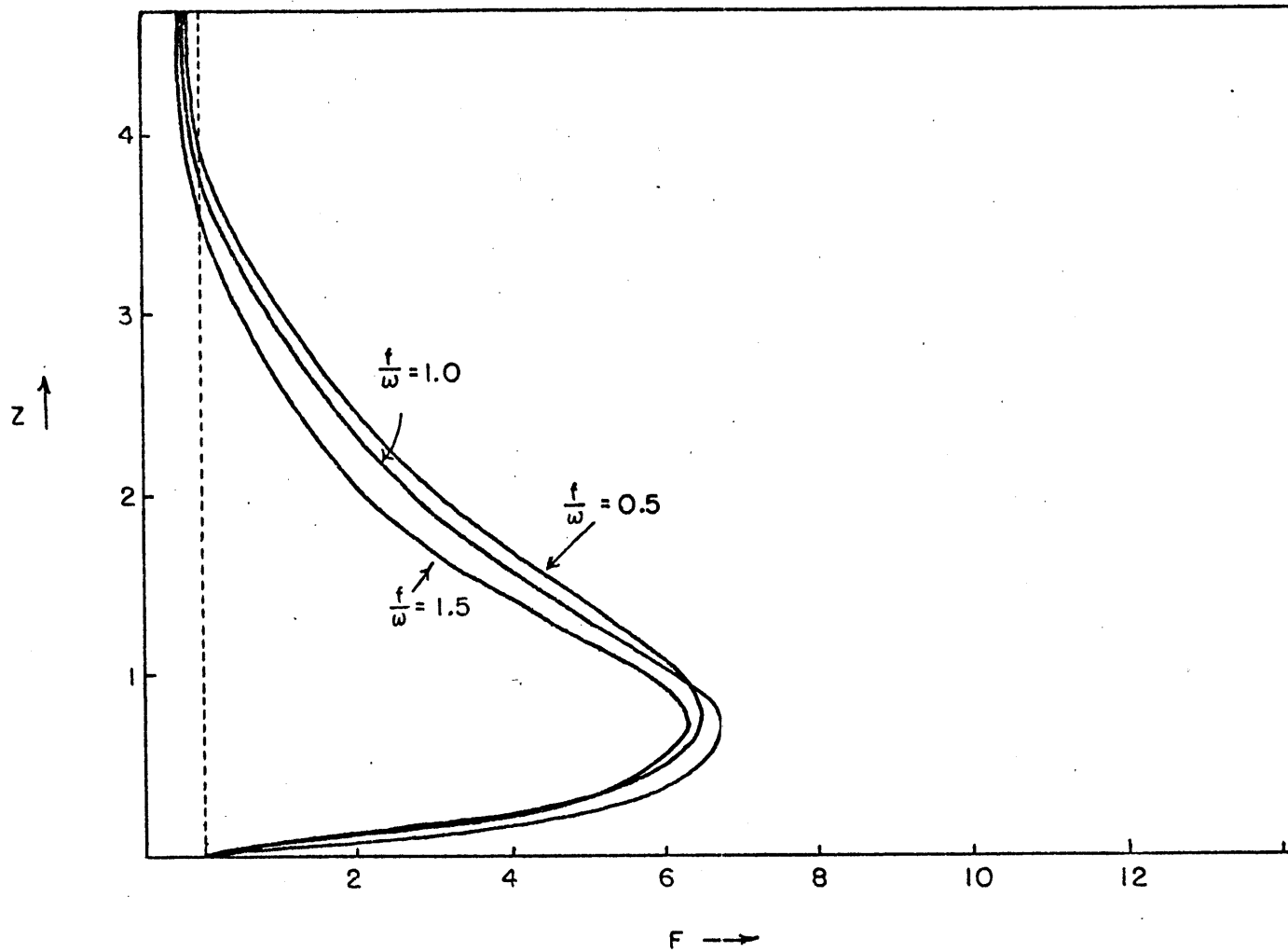


Figure 3.2. The time-averaged vertical heat flux  $F$  ( $\text{kJ sec}^{-1} \text{cm}^{-1}$ ) for the cases of  $N^2 = 10^{-4} \text{sec}^{-2}$ ,  $U = 0$ .  $z$  is nondimensional;  $w$  and  $b$  are scaled using  $b_{\text{max}} = 9.8 \text{cm sec}^{-2}$ .

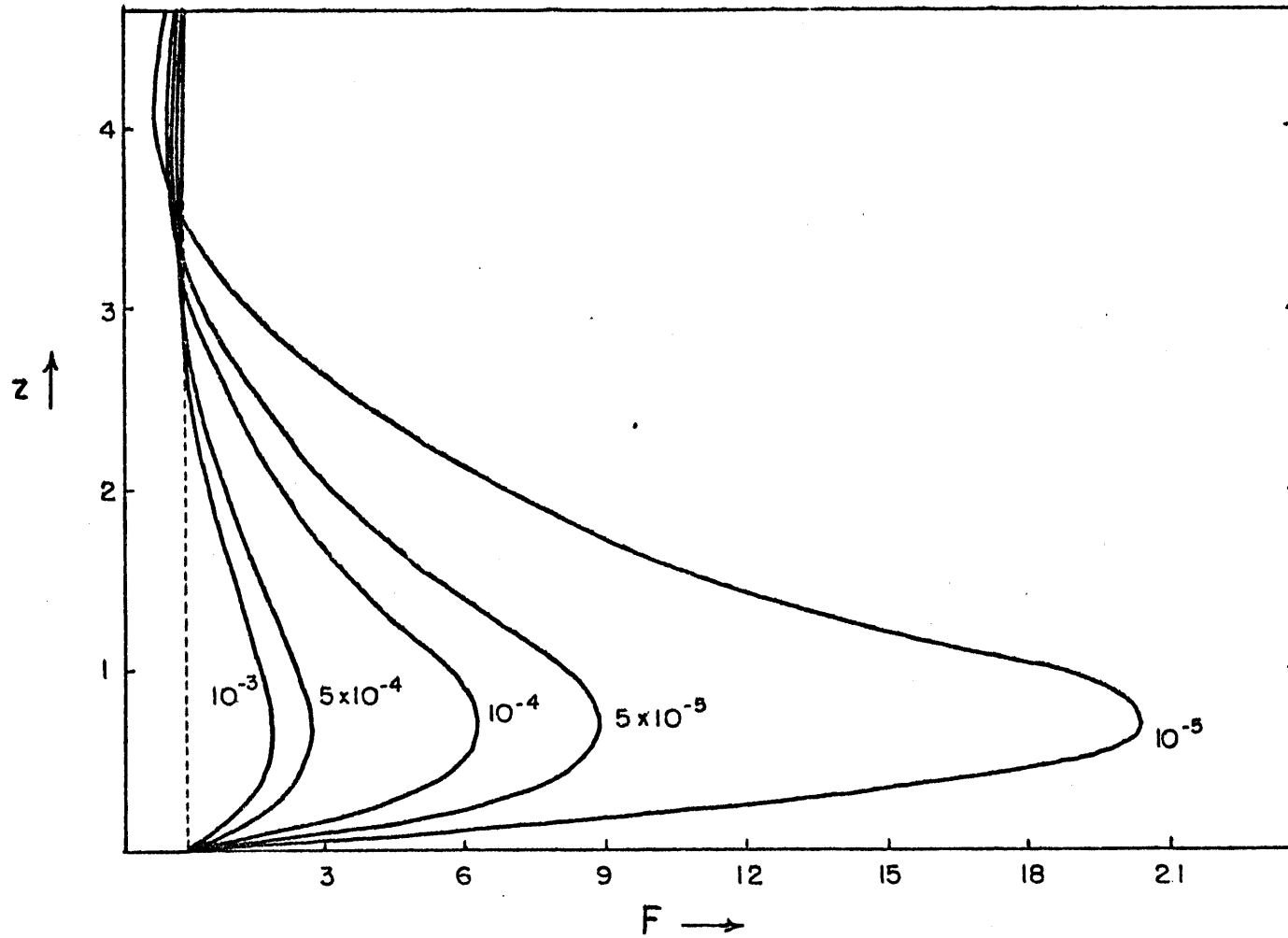


Figure 3.3. The time-averaged vertical heat flux  $F$  ( $\text{kJ sec}^{-1} \text{cm}^{-1}$ ) for five values of  $N^2$  with  $\frac{f}{\omega} = 1.5$ ,  $U = 0$ .  $z$  is nondimensional;  $w$  and  $b$  are scaled using  $b_{\text{max}} = 9.8 \text{ cm sec}^{-2}$ .

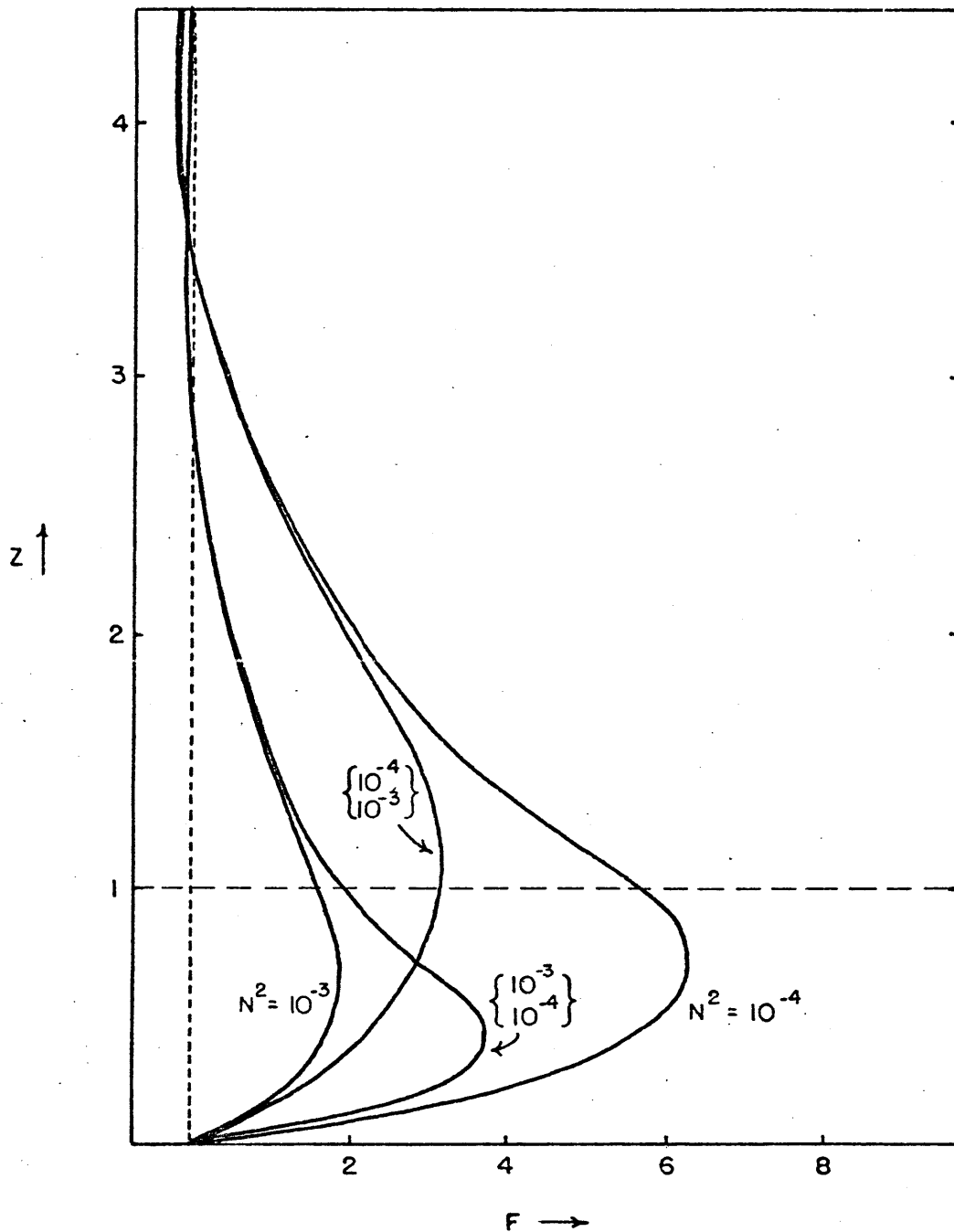


Figure 3.4. The time-averaged vertical heat flux  $F$  ( $\text{kJ sec}^{-1} \text{cm}^{-1}$ ) for four arrangements of  $N^2$  with  $\frac{f}{w} = 1.5$ ,  $U = 0$ .  $z$  is nondimensional;  $w$  and  $b$  are scaled using  $b_{\text{max}} = 9.8 \text{ cm sec}^{-2}$ .



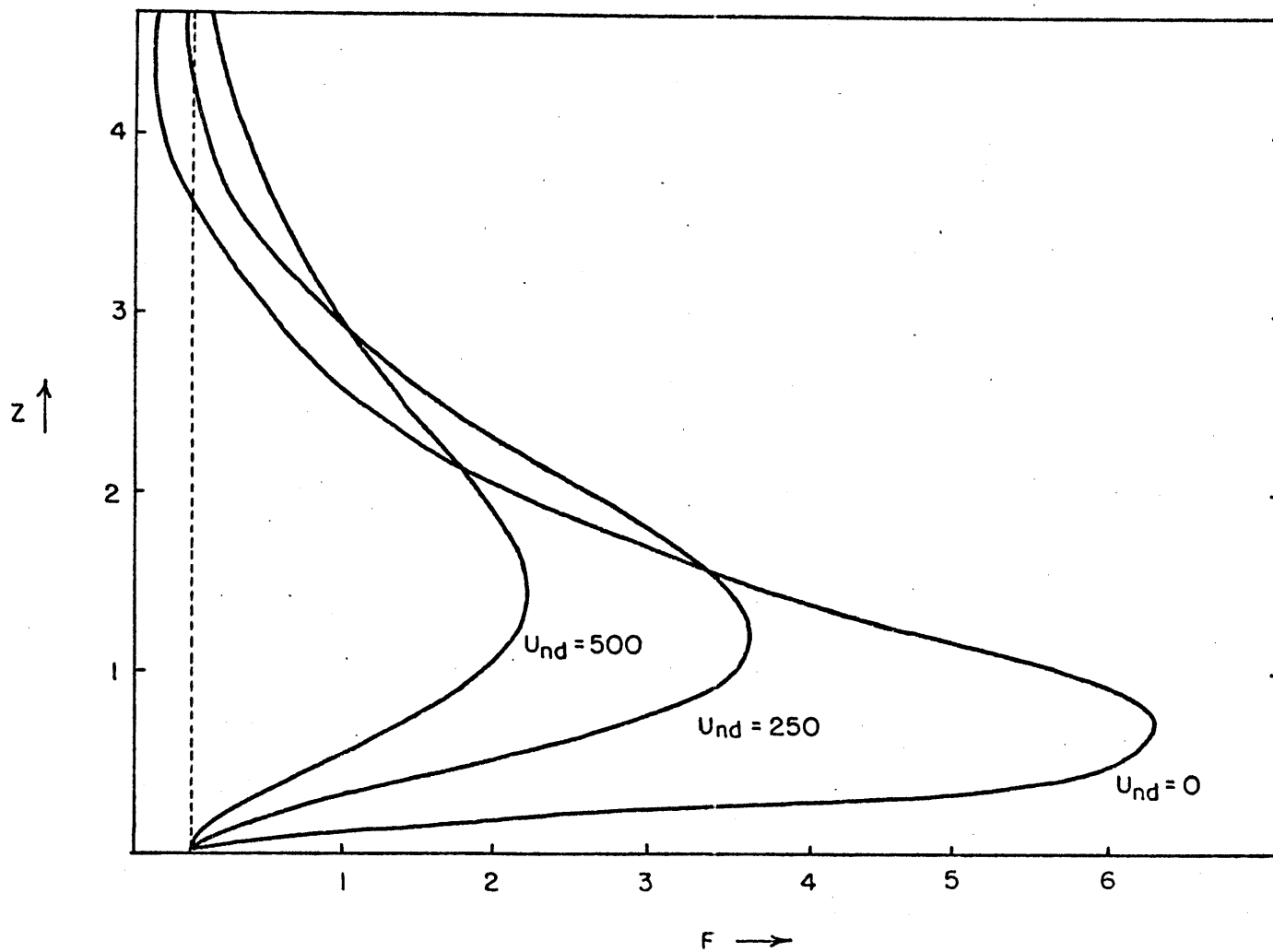


Figure 3.5. The time-averaged vertical heat flux  $F$  ( $\text{kJ sec}^{-1} \text{cm}^{-1}$ ) for three cases in which  $\frac{f}{w} = 1.5$ ,  $N^2 = 10^{-4} \text{sec}^{-2}$ .  $z$  is nondimensional;  $w$  and  $b$  are scaled using  $b_{\max} = 9.8 \text{cm sec}^{-2}$ .

The horizontally integrated flux will depend on the value of  $\kappa$  because  $x$  and  $z$  are scaled by the viscous length  $L = \sqrt{\frac{\kappa}{\omega}}$ . In section 3.3, where the fluxes are summed along the coastlines, the  $\kappa^{\frac{1}{2}}$  dependence is unchanged since the coastal lengths are dimensional.

The above discussion has assumed a single-harmonic diurnal temperature wave at the surface. The data presented by Lettau (1949, 1951) indicate that 6-12% of the diurnal temperature variation observed at typical inland stations is in the second harmonic. The results of chapter 2 should therefore be modified to include solutions in which the forcing frequency is a multiple of  $\omega$ . The dependence of the flux on  $\omega$  is apparent when the integrand of (3.2) is written as

$$(wb \, dx)_{dim} = (wb \, dx)_{nd} \frac{b_{max}^2}{\omega} \sqrt{\frac{\kappa}{\omega}} \quad (3.3)$$

The contribution of the higher harmonics is reduced according to the  $\omega^{-\frac{3}{2}}$  factor in (3.3). However, the smaller values of  $\frac{N^2}{\omega^2}$  associated with the higher harmonics will result in larger values of  $w_{nd}$ . Figure 3.3 shows that the nondimensional flux increases approximately as  $(\frac{N^2}{\omega^2})^{-1}$ . The dimensional flux in (3.3) therefore varies as  $\omega^{\frac{1}{2}}$ , indicating that an additional factor of  $\sqrt{2}$  must be introduced when the second harmonic's contribution to the flux is evaluated.

### 3.3 Application to actual coastal configurations

The results of section 3.2 are now used to compute the climatologically averaged vertical heat fluxes due to the sea breeze effect. Estimates are obtained for each continent and each season.

The coastline is represented by linear segments, each of which is assigned a  $\Delta T$  based on the monthly mean ocean temperature and monthly means of the maximum and minimum land temperatures. Since the temperatures are climatological averages, the effect of cloudiness is included in the data. The procedure used to compute  $\Delta T$  is discussed in Appendix C. The computed  $\Delta T$ 's are used to dimensionalize  $b$  and  $w$ .

Since the coastal segments are approximately 50 km in length, it is necessary to neglect smaller inlets, peninsulae, and islands. Large islands and inland bodies of water (e.g., the Great Lakes) are included. Representation of the coastline by linear segments also removes much of the curvature, although the effects of concavity and convexity should tend to cancel when many segments are included. Finally, stability and synoptic scale winds are included only as mean effects: the flux computations are based on the curve in figure 3.5 for which  $N^2 = 10^{-4} \text{ sec}^{-2}$  and  $U_{nd} = 250$ . Thus a normal gradient wind component of approximately 8 knots is used to represent the averaged influence of synoptic circulations. The dependence on  $f$  is not included, in view of figure 3.2.

Because of the sinusoidal time dependence of the forcing function, the results of the model are applicable only to the equinoctial months (March, September). However, calculations are also made for the months of June and December in order to gain a crude estimate of the summer and winter heat fluxes. At the summer solstice, the theoretical calculations will underestimate the sea breeze flux and overestimate

the land breeze flux. At the winter solstice, the reverse is true.

### 3.3.1 Results by season and by continent

The computed fluxes are presented in table 3.1. The values are for  $z \approx 1$ , where the flux reaches its maximum value (see figure 3.5).

The continents of Asia and Africa contribute the largest amounts to the total flux. While Africa's equatorial location results in little seasonal variation, Asia's more northerly location leads to a strong seasonal dependence. The Asian value for June (the monsoon season) is larger than any other monthly flux value. Europe and North America also show the expected strong seasonal dependence.

The fact that the northern hemisphere contains most of the world's land mass is reflected in the results, which show that 65% of the heat flux occurs in the northern hemisphere. The northern summer month of June contributes the most to the annual total, while the southern summer month of December contributes the least.

### 3.3.2 Comparison to other estimates of the sensible heat flux

In the middle and upper troposphere, synoptic scale eddies and the mean meridional cells accomplish most of the upward transport of sensible heat. Small scale eddies, referred to as convective turbulence, dominate the transport in the lower troposphere. The cloud patterns which appear in satellite photographs suggest that the sea breeze effect plays a role in organizing convective turbulence (Bugaev, 1973). The importance of this role is indicated by the relative magnitudes of the sea breeze and total vertical heat fluxes. Unfortunately, the magnitude

Table 3.1. Computed vertical heat fluxes due to the sea breeze effect.

(units:  $10^{14}$  j sec<sup>-1</sup>)

	<u>March</u>	<u>June</u>	<u>September</u>	<u>December</u>	<u>Annual Average</u>
Africa	0.53	0.52	0.58	0.42	0.51
Asia	0.50	0.92	0.60	0.17	0.55
Australia	0.24	0.07	0.24	0.29	0.21
Europe	0.09	0.50	0.23	0.00	0.20
N. America	0.23	0.67	0.33	0.06	0.32
S. America	0.36	0.18	0.39	0.34	0.32
Northern Hemisphere	1.18	2.45	1.45	0.39	1.37 (65%)
Southern Hemisphere	0.76	0.42	0.91	0.89	0.74 (35%)
Total	1.94	2.87	2.36	1.28	2.11

of the vertical flux of sensible heat is uncertain because it cannot be measured directly. In studies of the atmosphere's heat balance, the sensible heat flux is generally assigned the value required to balance the net effect of the other thermal processes. It therefore includes the sum of the errors in the estimates of all the other quantities. These errors are reflected in the variability of the previous estimates of the total sensible heat flux:

Kondratyev (1969)	$6.8 \times 10^{15} \text{ j sec}^{-1}$
Budyko (1958)	$8.5 \times 10^{15} \text{ j sec}^{-1}$
London (1957)	$19.0 \times 10^{15} \text{ j sec}^{-1}$
Houghton (1954)	$17.3 \times 10^{15} \text{ j sec}^{-1}$

Although these results are for the surface, the values probably do not vary significantly in the lowest kilometer (Palmen and Newton, 1969).

The four estimates of the total sensible heat flux are to be compared with the annual average of the sea breeze heat flux ( $2.1 \times 10^{14} \text{ j sec}^{-1}$ ) as estimated in section 3.3.1. Since the four previous studies agree on the order of magnitude of the total flux, and since the sea breeze flux is computed from realistic values of  $w$  and  $b$ , one may conclude that the sea breeze effect accounts for between 1% and 5% of the vertical flux of sensible heat at a height of several hundred meters. Above and below the level where the sea breeze flux reaches its maximum (see figure 3.5), the percentage is smaller.

A comparison can also be made with the upward heat transport accomplished by an extratropical cyclone. For the synoptic case of 4-5 April 1950, Palmen and Newton (1969) calculate a heat flux of  $2.3 \times 10^{14} \text{ j sec}^{-1}$

at 500 mb, the approximate level at which synoptic scale transports reach their maximum values. Therefore, in terms of the vertical transport of sensible heat, the globally integrated effect of the sea breeze at  $z \approx 250$  m is comparable to the effect at 500 mb of one extratropical cyclone.

#### 4. THE NONLINEAR FINITE-DIFFERENCE MODEL

The results of chapter 2 show that the linear model can describe and predict many of the observed features of the sea breeze. There remains the task of examining the nonlinear advection process, the omission of which appears to be the most serious shortcoming of the linear model. One expects that advection by the perturbation velocity will not change the gross features of the circulation, although advection should tend to redistribute the fields of velocity and temperature. The effect of nonlinear momentum advection was already anticipated in section 2.4.2, where a criterion for sea breeze occurrence was based on the assumption that the maximum perturbation velocity will be found at the coastline.

In a finite difference model of the sea breeze, the lateral boundaries must be sufficiently far from the coastline that boundary effects do not contaminate the solution. At the same time, the mesh must be fine enough to resolve the steep velocity and temperature gradients which are found near the coastline. In order to avoid the excessive storage requirements of a uniform fine grid, some previous investigators have resorted to stretched coordinate systems (Fisher, 1961; Moroz, 1967; Bhumralkar, 1972), while others have used uniform coarse grids with horizontal space increments of  $\Delta x = 4$  km (McPherson, 1967; Neumann and Mahrer, 1971) or  $\Delta x = 11$  km (Pielke, 1973). Each of these earlier models suffered from computational instability effects which were overcome only by artificial smoothing techniques (see table 1.1). An alternative to coordinate stretching is the method of overlapping



grids, a technique which is used in the present study. This technique may also have application to other phenomena such as hurricanes and squall lines which occur on a small enough scale that a fine mesh is required for adequate resolution.

#### 4.1 Description of the model

Since the aim of this section is to examine the effects of advection, the equations are the same as those of chapter 2 except for the nonlinear advection terms:

$$\frac{\partial u}{\partial t} + \frac{\partial}{\partial x} (Uu + u^2) + \frac{\partial}{\partial z} (wu) - fv = -\frac{\partial p}{\partial x} + \nu \frac{\partial^2 u}{\partial z^2} \quad (4.1)$$

$$\frac{\partial v}{\partial t} + \frac{\partial}{\partial x} (Uv + uv) + \frac{\partial}{\partial z} (wv) + fu = \nu \frac{\partial^2 v}{\partial z^2} \quad (4.2)$$

$$\frac{\partial b}{\partial t} + \frac{\partial}{\partial x} (Ub + ub) + \frac{\partial}{\partial z} (wb) + N^2 w = \kappa \frac{\partial^2 b}{\partial z^2} \quad (4.3)$$

$$b = \frac{\partial p}{\partial z} \quad (4.4)$$

$$\frac{\partial u}{\partial x} + \frac{\partial w}{\partial z} = 0 \quad (4.5)$$

The hydrostatic approximation has been made to facilitate the numerical integration, the continuity equation has been used to write the equations in "flux" form, and a basic current  $U$  has been included. The finite difference form of (4.1)-(4.5) is described in Appendix D, which also lists the boundary conditions. A lid is placed at  $H = 2.5$  km, a height at which the linear model predicts very small ( $1-10 \text{ cm sec}^{-1}$ ) velocities, and the vertical interval  $0 \leq z \leq H$  is divided into equal

space increments. The tendency for the development of an upper boundary layer is of little importance since the model is not run beyond  $t = 8$  hours.

A system of seven overlapping grids (Appendix D) is used to achieve the desired horizontal resolution near  $x = 0$  while enabling the lateral boundaries to be placed far ( $x = \pm 127$  km) from the coastline. The size of  $\Delta x$  varies from 0.5 km on the inner grid to 4.0 km on the outermost grids. The corresponding time steps are 30 sec and 240 sec. (This system of overlapping grids requires less than one-third the core storage and less than one-sixth the computing time of a uniform mesh,  $\Delta x = 0.5$  km, covering the same area). Any "noise" resulting from the interaction at the grid boundaries is minimized by using a two-step Lax-Wendroff scheme based on a time- and space-staggered lattice. This scheme is well-behaved computationally and does not require additional "smoothing" or periodic adjustments to avoid computational instability and "grid separation". In this application of the Lax-Wendroff scheme, the only smoothing is the removal of the discontinuity in the forcing function:  $b_0$  is halved at  $x = \pm 0.25$  km.

Unlike the linear model, the nonlinear model begins from a state of rest at  $t = 0$ . The two model circulations are compared in the next section.

#### 4.2 Results of the numerical integrations

Table 4.1 summarizes the integrations which were performed with the finite difference model. In each case, the external parameters were assigned the following values:  $\frac{f}{\omega} = 1.5$  ( $\phi = 48^\circ$  N),  $N^2 = 10^{-4} \text{ sec}^{-2}$ ,

Table 4.1. Summary of the nonlinear numerical integrations

<u>Run #</u>	<u>levels</u>	<u><math>(\Delta T)_{\max}</math></u>	<u><math>-U</math> (m sec<sup>-1</sup>)</u>	<u><math>u_{\max}</math> (t = 8 hrs) (m sec<sup>-1</sup>)</u>	<u>x of <math>u_{\max}</math> (km)</u>
1a	10	3 C°	0.0	1.65	2.75
1b	10	3 C°	1.0	1.96	1.75
1c	20	3 C°	2.0	2.15	0.75
1d	20	3 C°	3.25	1.13	-4.25
2a	10	5 C°	0.0	2.12	4.75
2b	20	5 C°	1.5	2.80	1.75
2c	20	5 C°	4.0	1.48	-4.25
3	10	7 C°	0.0	2.95	6.50
4a	10	9 C°	0.0	4.75	9.25
4b	20	9 C°	2.0	3.80	4.25
4c	20	9 C°	3.25	3.50	0.25
4d	20	9 C°	4.25	3.10	-3.00
5	10	5 C°	1.5	2.44	-3.00

Note: In run #5, the nonlinear advection terms were omitted.

$\kappa = \nu = 5 \times 10^4 \text{ cm}^2 \text{ sec}^{-1}$ . The integrations were carried out to  $t = 8$  hours, at which time the maximum wind speeds have just begun to decrease. The weakening stage of the sea breeze was not examined because it does not aid in the formulation of a sea breeze occurrence criterion.

In order to permit as direct a comparison as possible with the linear results, the finite difference model was run without the non-linear terms for the case of  $(\Delta T)_{\max} = 5 \text{ C}^\circ$ ,  $U = -1.5 \text{ m sec}^{-1}$  (run #5). Figure 4.1 shows  $u(x)$  at  $z = 250 \text{ m}$  ( $k = 1$ ), together with the analytically computed values of  $u$  at  $z = 0.33$  for the case of  $(\Delta T)_{\max} = 5 \text{ C}^\circ$ ,  $U = -1.8 \text{ m sec}^{-1}$ . The two models show reasonable agreement, especially when one considers that the finite difference circulation begins from a state of rest at  $t = 0$ , while the analytic sea breeze must overcome the land breeze remnants which persist beyond  $t = 0$ .

When the nonlinear advection terms are included, the perturbations show the expected onshore movement. Figure 4.2 shows isopleths of  $u$  and  $b$  at  $t = 8$  hours for the case of  $(\Delta T)_{\max} = 3 \text{ C}^\circ$ ,  $U = 0$  (run #1a). Even though the circulation is weak, the maximum velocity perturbations have been advected several kilometers inland. Cooler offshore temperatures ( $b < 0$ ) are also advected across the coastline, as was anticipated in section 2.3. The depth of the onshore flow, as well as the relative intensities of the low-level and return currents, are in good agreement with the linear results.

Figure 4.3 shows the results for the case of  $(\Delta T)_{\max} = 5 \text{ C}^\circ$ ,  $U = -4 \text{ m sec}^{-1}$  (run #2c). The basic current causes the perturbation to assume a frontal character, even more so than in the linear model.

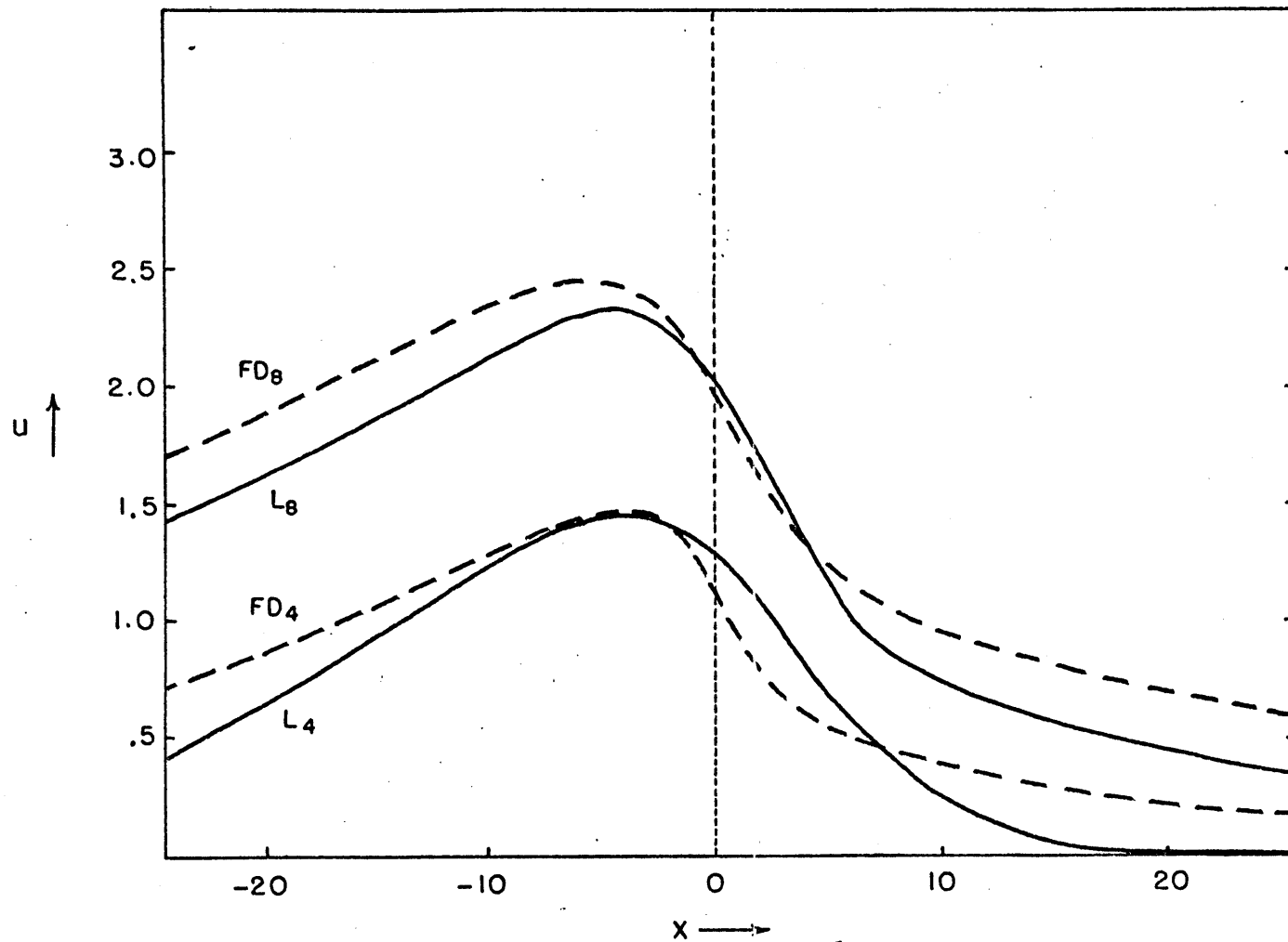


Figure 4.1. Comparison of the low-level  $u$  components ( $\text{m sec}^{-1}$ ) at  $t = 4, 8$  hours. Dashed curves are  $z = 0.33$  results of linear model with  $(\Delta T)_{\text{max}} = 5 \text{ C}^\circ$ ,  $U = -1.8 \text{ m sec}^{-1}$ . Solid curves are  $k = 1$  ( $z = 250 \text{ m}$ ) results of finite difference model (nonlinear advection terms omitted) with  $(\Delta T)_{\text{max}} = 5 \text{ C}^\circ$ ,  $U = -1.5 \text{ m sec}^{-1}$ . In each case,  $\frac{f}{\omega} = 1.5$ ,  $N^2 = 10^{-4} \text{ sec}^{-2}$ ,  $\kappa = \nu = 5 \times 10^4 \text{ cm}^2 \text{ sec}^{-1}$ .  $x$  is in kilometers.

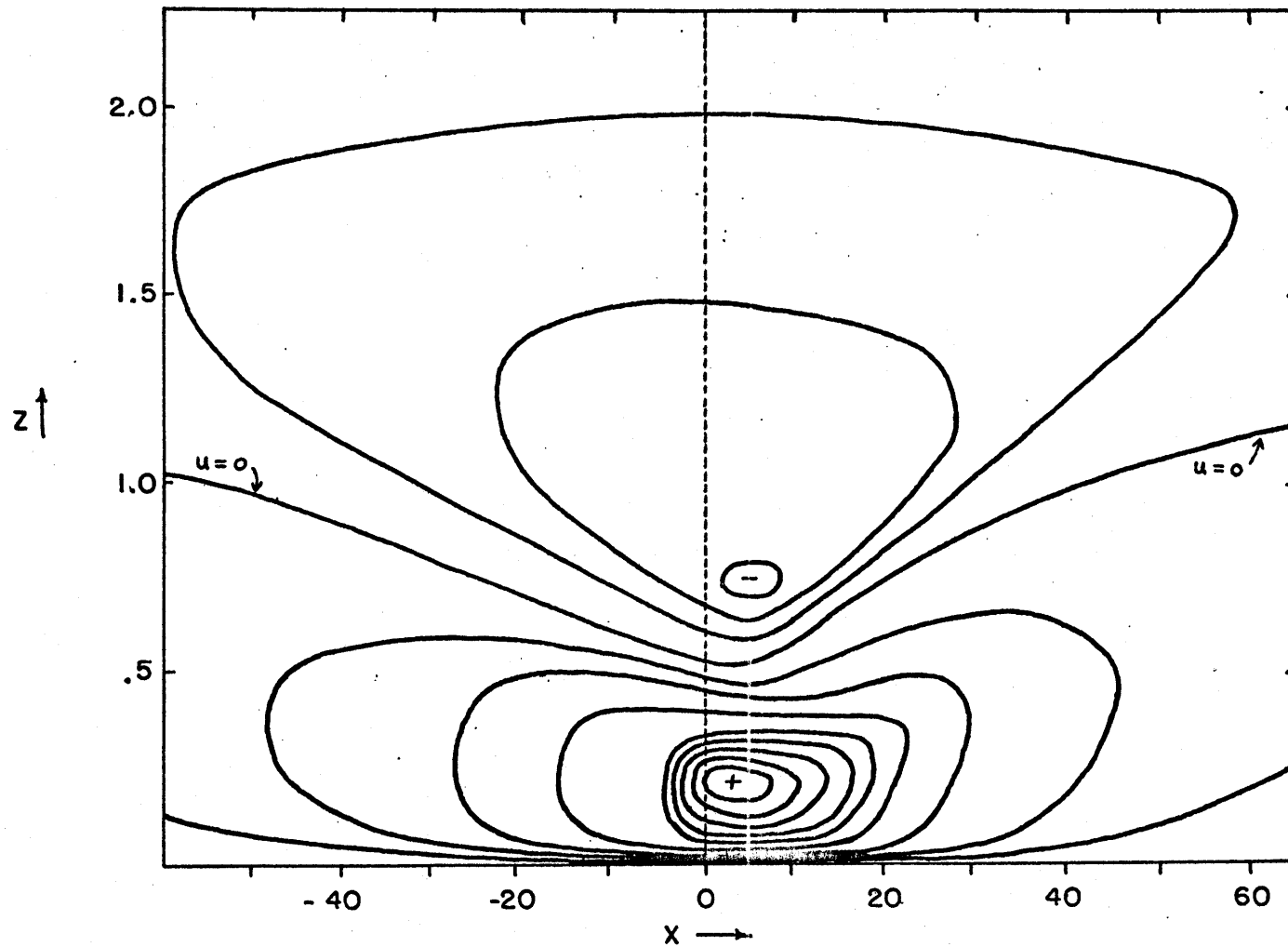


Figure 4.2a. Isopleths ( $0.2 \text{ m sec}^{-1}$  intervals) of the  $u$  component of the velocity at  $t = 8$  hours for run # 1a ( $\Delta T_{\text{max}} = 3 \text{ C}^\circ$ ,  $U = 0$ ,  $\frac{f}{\omega} = 1.5$ ,  $N^2 = 10^{-4} \text{ sec}^{-2}$ ).  $x$  and  $z$  are in kilometers.

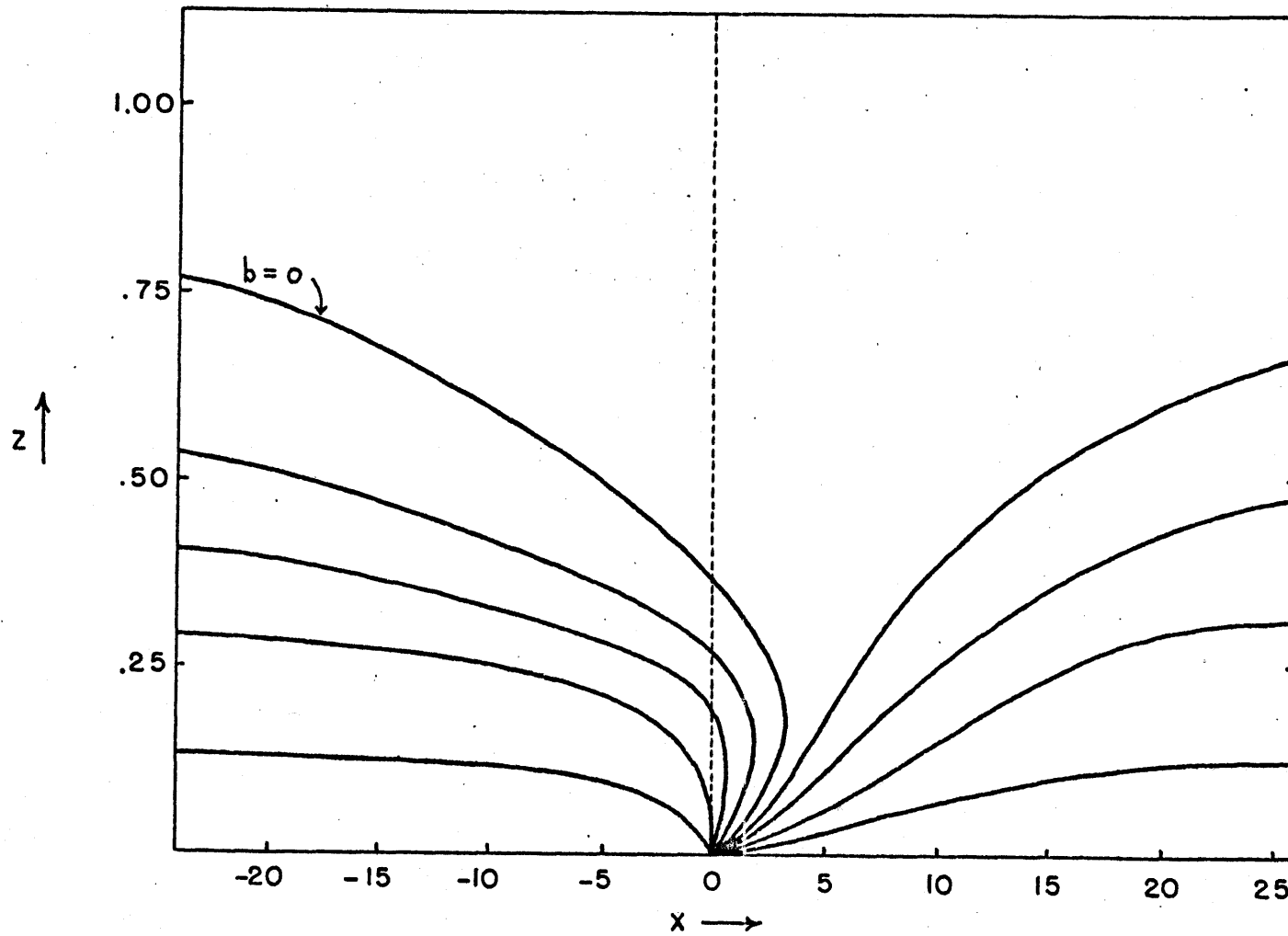


Figure 4.2b. Isopleths ( $0.1 \text{ cm sec}^{-2}$  intervals) of the buoyancy at  $t = 8$  hours for run # 1a.  $x$  and  $z$  are in kilometers.

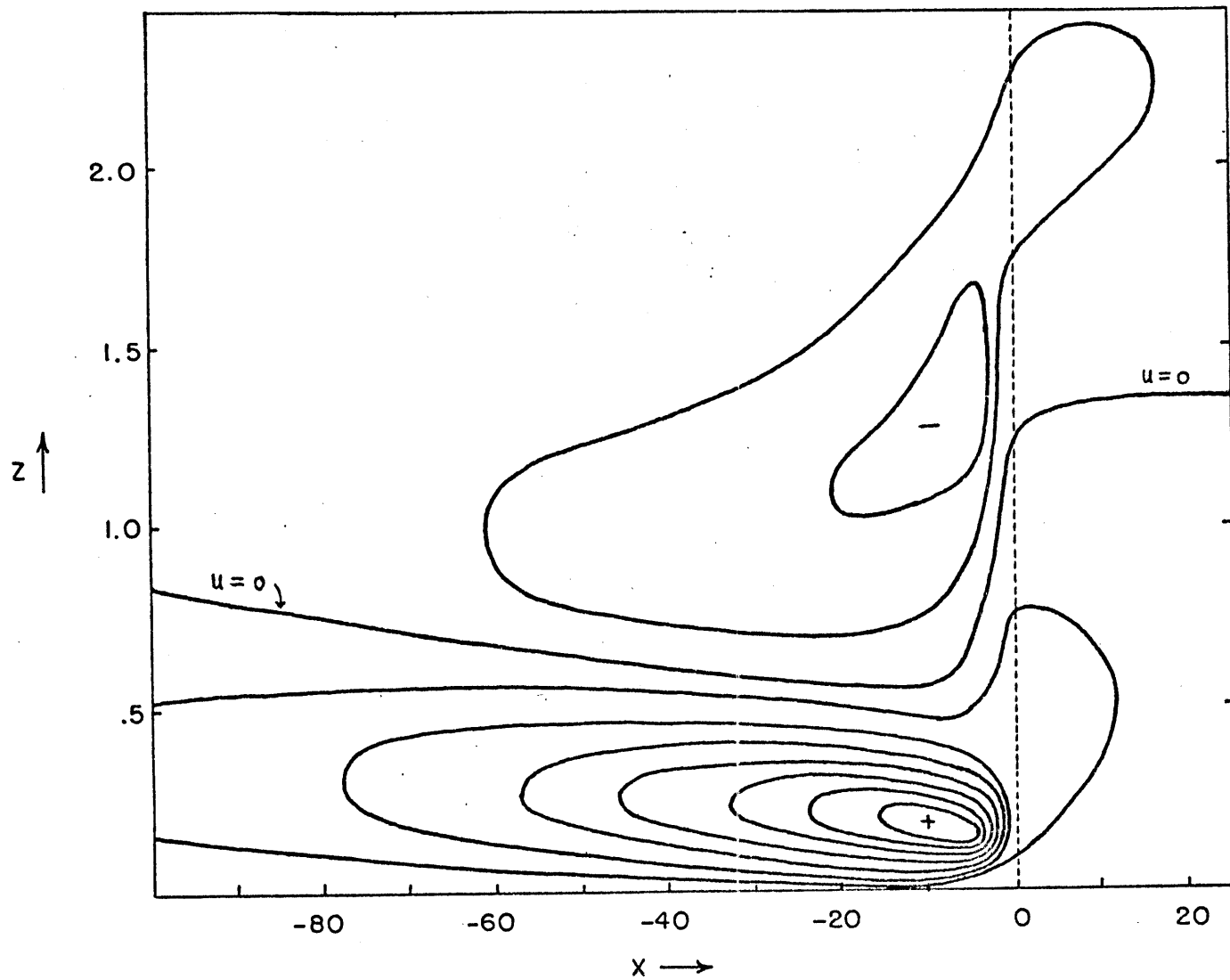


Figure 4.3a. Isopleths ( $0.2 \text{ m sec}^{-1}$  intervals) of the  $u$  component of the velocity at  $t = 8$  hours for run # 2c ( $\Delta T_{\text{max}} = 5 \text{ C}^\circ$ ,  $U = -4.0 \text{ m sec}^{-1}$ ,  $\frac{f}{\omega} = 1.5$ ,  $N^2 = 10^{-4} \text{ sec}^{-2}$ ).  $x$  and  $z$  are in kilometers.



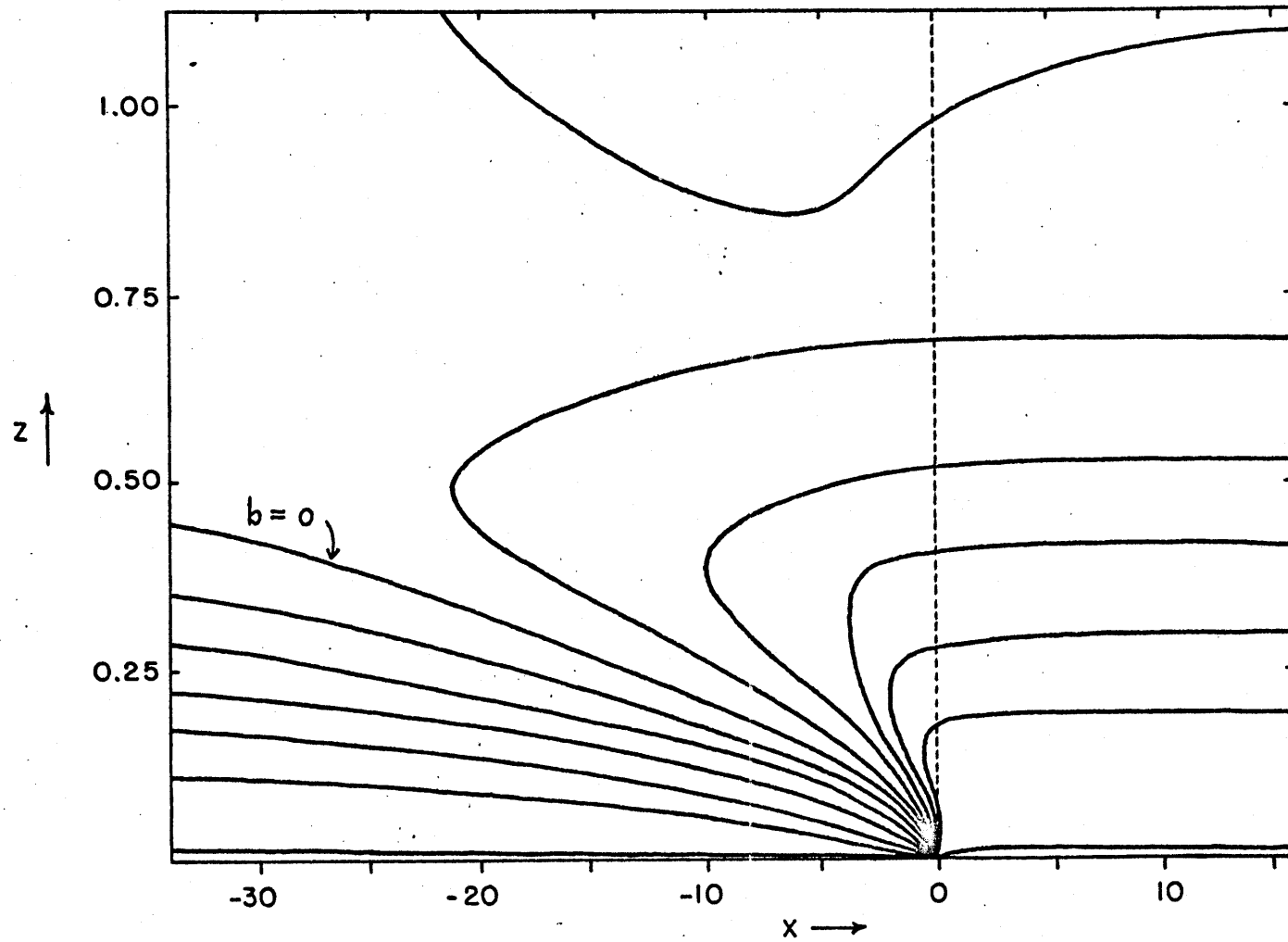


Figure 4.3b. Isopleths ( $0.1 \text{ cm sec}^{-2}$ ) of the buoyancy at  $t = 8$  hours for run # 2c.  $x$  and  $z$  are in kilometers.

The steepest gradients are slightly offshore in figure 4.3 because of the strong basic current in this particular example.

For maximum temperature differences of  $3\text{ C}^\circ$  and  $5\text{ C}^\circ$ , the addition of a weak basic current increases the maximum perturbation velocity (see table 4.1). This behavior is illustrated in figure 4.4, which shows that the velocities near the coastline are larger and the inland velocities are smaller when a basic current of  $-1.0\text{ m sec}^{-1}$  is present. Momentum is concentrated near the coastline because onshore nonlinear advection tends to offset the advection by the basic current. The linear model, on the other hand, predicts that the maximum  $u$  perturbation will be reduced in magnitude and advected offshore (figure 2.16). When nonlinear effects are reduced in importance by a large  $|U|$ , the nonlinear model also predicts a weakened and an offshore  $u_{\max}$  (runs # 1d, 2c, 4d).

The  $x$ -coordinate of the maximum perturbation velocity is examined as a function of time in figure 4.5. When the basic current is of approximately the same magnitude as the maximum perturbation velocity, the nonlinear model predicts that  $u_{\max}$  will first be advected offshore. As the perturbation becomes stronger,  $u_{\max}$  moves back toward the coast. Figure 4.5a, which contrasts the behavior of the nonlinear and linear models, supports the assumption of section 2.4.2 that  $u_{\max}$  will be found at the coastline when  $|u_{\max}| \approx |U|$ .

Figure 4.5b shows the effect of nonlinear advection when the basic current is strong. In this case (run #2c), the perturbation is not strong enough to advect  $u_{\max}$  back to the coastline, but it is clearly able to retard the offshore advection.  $|U|$  is large enough that figure 4.5b represents a non-sea breeze case by either criterion of figure 2.18.

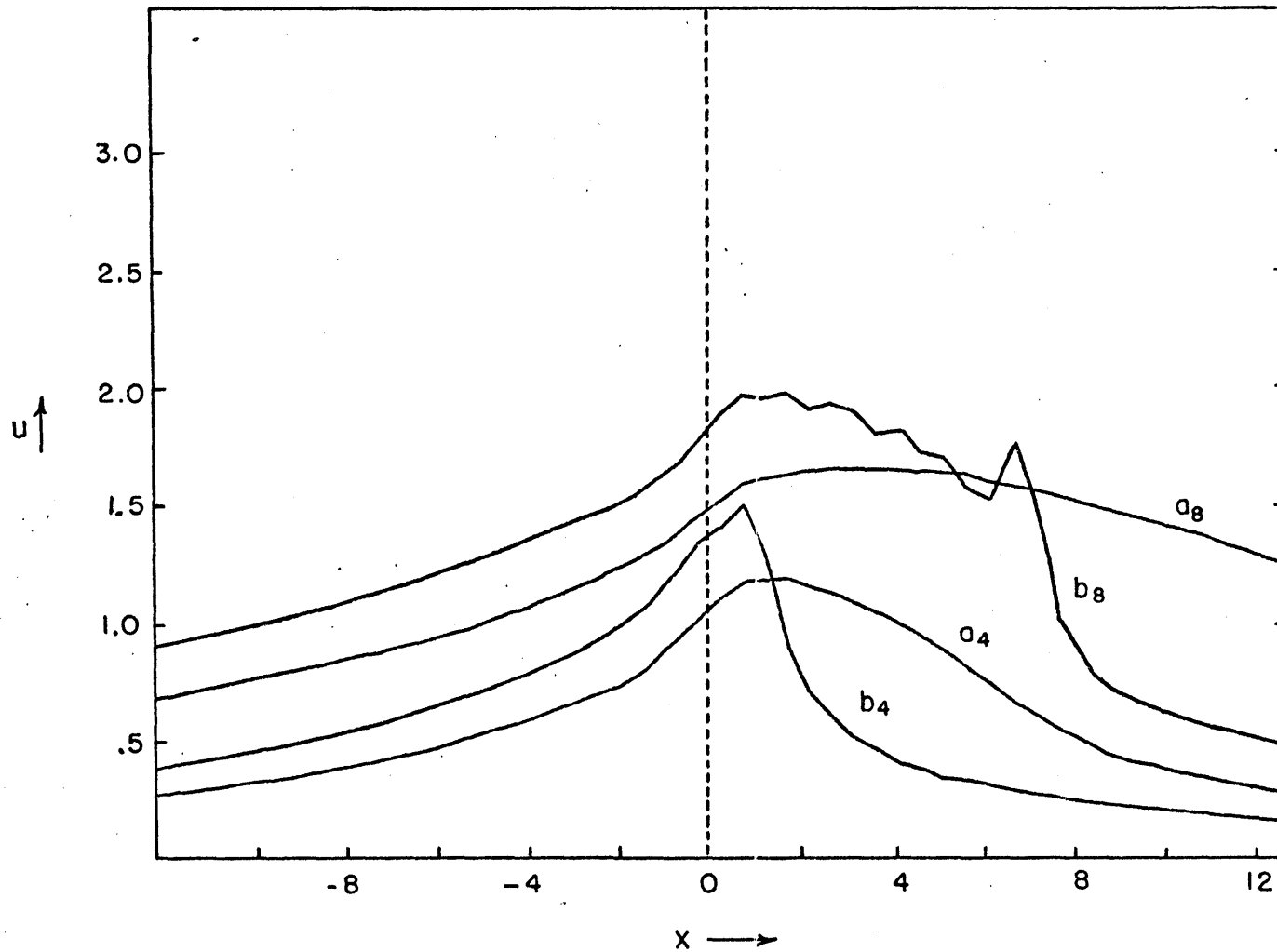
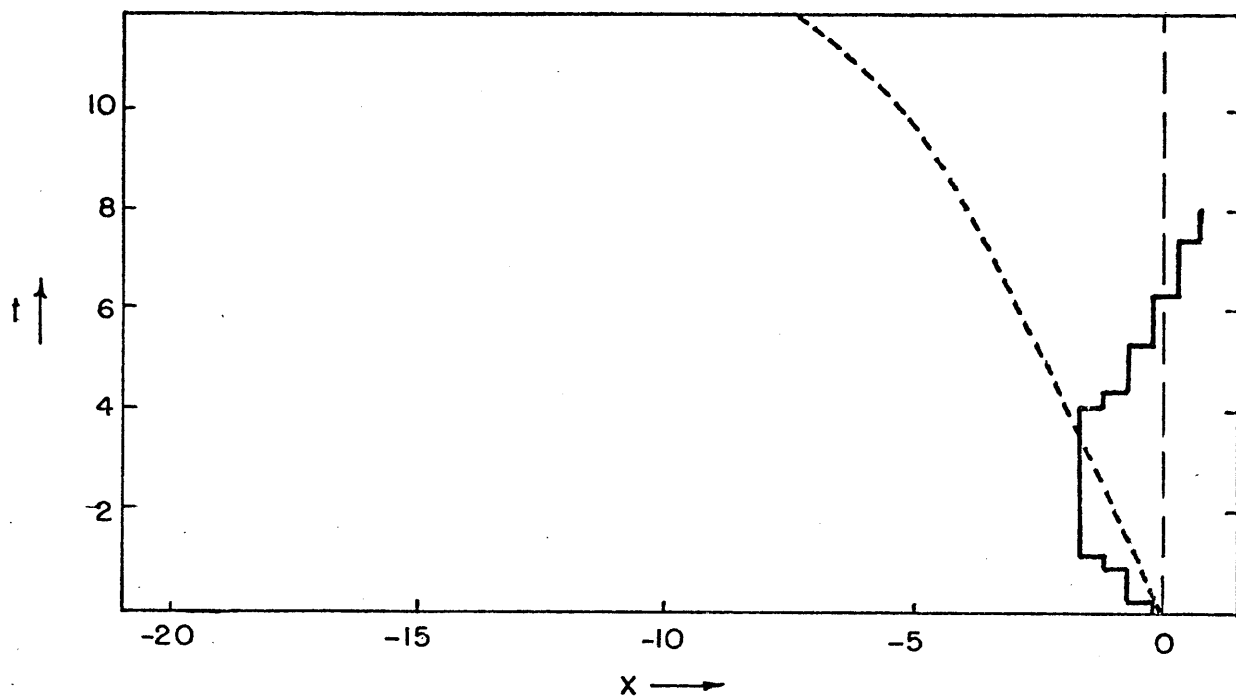
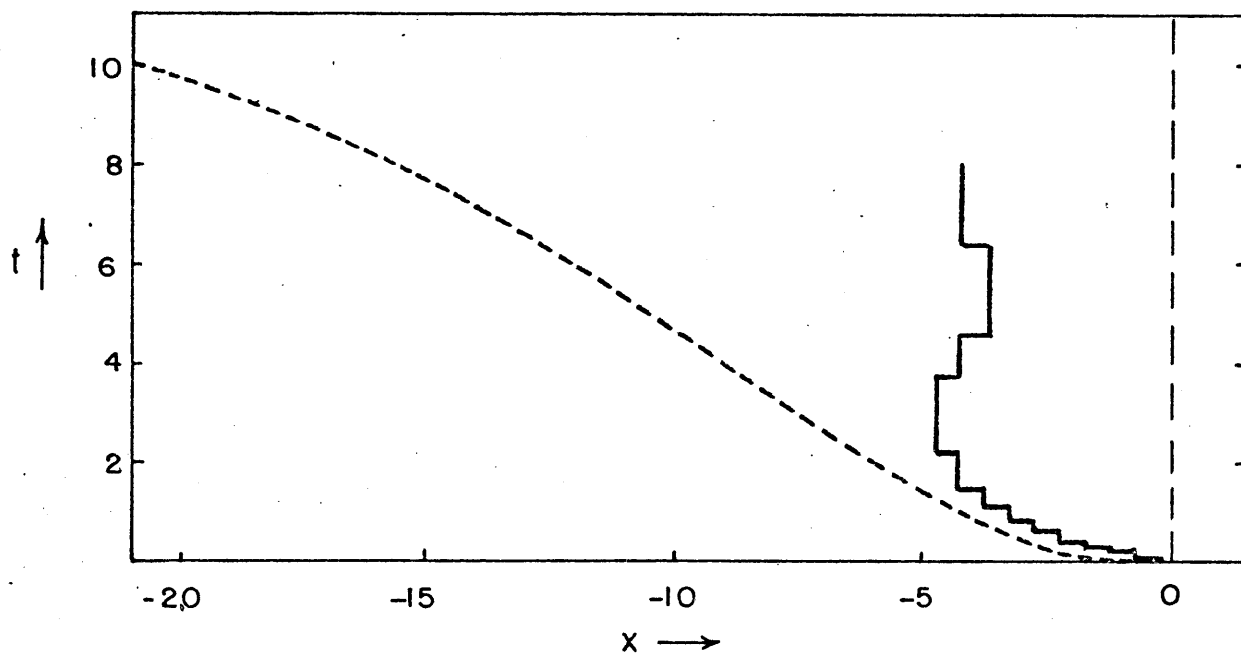


Figure 4.4. The  $u$  component of the velocity in  $\text{m sec}^{-1}$  at  $k = 1$  ( $z = 250$  m) for (a) run # 1a:  $\Delta T_{\text{max}} = 3$  C°,  $U = 0$  and (b) run # 1b:  $\Delta T_{\text{max}} = 3$  C°,  $U = -1.0$   $\text{m sec}^{-1}$ . The subscripts 4 and 8 refer to hours<sub>max</sub> after sunrise.  $x$  is in kilometers.



(a)  $(\Delta T)_{\max} = 3 \text{ C}^\circ$ ,  $U = -1.8 \text{ m sec}^{-1}$  (linear),  $-2.0 \text{ m sec}^{-1}$  (nonlinear)



(b)  $(\Delta T)_{\max} = 5 \text{ C}^\circ$ ,  $U = -4.5 \text{ m sec}^{-1}$  (linear),  $-4.0 \text{ m sec}^{-1}$  (nonlinear)

Figure 4.5. x-coordinate (km) of the maximum value of  $u$  at  $k = 1$  ( $z = 125 \text{ m}$ ). Dashed curves are linear results, solid curves are nonlinear results. Time is in hours after sunrise.

The validity of the nonlinear model as a sea breeze predictor is examined in figure 2.18, which locates runs # 1a - 5 in  $U - (\Delta T)_{\max}$  space. Each point is marked with the maximum value of  $(U + u)$  which occurs in the region  $x \geq 0$  at  $t = 8$  hours. Since positive values imply that a sea breeze exists on land, the nonlinear results are quite consistent with the empirical criterion of Lyons. The nonlinear results also agree quite well with the linear criterion based on the assumption that the maximum perturbation is found near the coastline when  $u_{\max} \approx |U|$ .

The results in table 4.1 may contain small errors because of numerical effects. Since artificial smoothing devices are not used in the numerical integrations, irregularities such as those in figure 4.4 tend to develop. The irregularities are most apparent when  $(\Delta T)_{\max}$  is large and when  $|U|$  is approximately equal to  $|u_{\max}|$ . In these cases, very large values of  $\frac{\partial u}{\partial x}$  are found near the coastline in the vicinity of the "sea breeze front". Significantly, the irregularities develop in these regions where the  $u$  gradient is steepest rather than in the regions of grid overlap; the problem is therefore not attributed to the grid overlap. Rather, the difficulty apparently lies in the inability of (4.1)-(4.5) to handle the behavior of the nonlinear system when  $u$  decreases rapidly with  $x$ . A possible explanation is that non-hydrostatic effects become important because of the large values of  $\frac{\partial w}{\partial t}$  in the frontal region. Another possibility is that the irregularities are to some extent real, representing local small-scale instabilities which are not handled well by the numerical scheme after they reach a certain magnitude. The irregularities are not examined further because they do not alter the conclusions about the nonlinear advection process which is the subject of this chapter.

## 5. SUMMARY AND CONCLUSIONS

This study has shown that a linear model can produce a sea breeze with realistic velocities and dimensions. The time-dependence of the computed circulation is also realistic: the computed and observed onset times agree very well, as do the times of maximum sea breeze intensity. These results imply that the  $\kappa \frac{\partial^2 b}{\partial z^2}$  parameterization of eddy conduction is adequate for many purposes. An examination of the balance of forces has indicated that the omission of coriolis and viscous effects by earlier modellers was not justified. The symmetric linear solution's most unrealistic feature, which has been shown to be due to the neglect of advection, is the concentration of large velocities near the coastline.

Because of the linear model's simplicity, one is able to explore the dependence of the circulation on the external parameters  $f$  and  $N^2$ . Among the results are an earlier predicted onset time at higher latitudes and an amplitude maximum at the inertial latitude. Strong stabilities (large  $N^2$ ) are associated with weaker circulations but more rapid inland propagations. These predictions cannot be tested adequately until more complete observational studies are made.

The large velocities near the coastline are reduced when a (constant) basic current is included. Maximum vertical velocities of several  $\text{cm sec}^{-1}$  occur in a narrow updraft which is suggestive of the sea breeze "frontal" region. Although sea breeze fronts have previously been detected only in nonlinear models, the results of chapter 2 imply that some of the "physics" of sea breeze frontal formation is present in the linear model if a basic current is included.

A nonlinear model, which is not constrained to behave periodically in time, will clearly be able to develop a more realistic sea breeze front.

The results from the linear model are realistic enough to be used in heat flux calculations. Integrations along the coastlines of six continents have shown that the sea breeze component of the general circulation can account for several per cent of the vertical flux of sensible heat at  $z \approx 250$  m. Since the flux computations were based on an algorithm which minimized the effect of the land breeze, the results of chapter 3 may well be underestimates.

Because the velocity components are scaled by  $\frac{b_{max}}{\omega}$ , the linear results are readily applied to the sea breeze prediction problem. The constant parameter in the empirical criterion  $\Delta T > \epsilon U^2$  has been given a physical interpretation in terms of the forcing frequency  $\omega$  and the conduction coefficient  $\chi$ . The value of  $\epsilon$  deduced from the Chicago lake breeze has been used to determine an appropriate value of the diffusion coefficient for use in scaling the basic current. The scaled basic current was then used to develop a theoretical sea breeze occurrence criterion which agrees very well with the empirical criterion.

The nonlinear advection process has been examined by using a finite difference model. In the absence of a basic current, the nonlinear model successfully predicts the onshore advection of the maximum perturbation. It also verifies the assumption that the nonlinear terms retard the offshore advection when a basic current is present. Suggested further applications of the finite difference

model include a study of the importance of initial conditions, which most likely account for the differences between the linear results and the nonlinear results with advection omitted. The dependence on  $\kappa$  and  $\nu$  can also be explored with the nonlinear model. Specifically, results of a constant-diffusivity case should be compared to the results when  $\kappa$  and  $\nu$  are made functions of the stability, shear, etc. Since the simple models of this study have produced realistic sea breezes, only minor improvements should result from detailed eddy diffusion formulations; for example, the weaker intensity of the land breeze might be predicted.

The results of chapter 4 indicate that the overlapping of grids is both feasible and useful in the study of mesoscale circulations. Even with four different mesh sizes, the numerical model was consistent with the linear model and produced realistic "nonlinear" circulations. The numerical problems which were encountered appear to be unrelated to the grid overlap. Because of the tendency for irregularities to develop in the region of large  $|\frac{\partial u}{\partial x}|$ , the validity of the hydrostatic assumption should be examined more closely. The linear model has indicated that the hydrostatic approximation is justified, but this conclusion may have to be modified when nonlinear advection is included.



### Appendix A. Numerical aspects of the linear solution

All computations were done on the IBM 370/165 at the M.I.T. Information Processing Center. The following procedure was used to obtain the linear solutions of chapter 2:

1. The roots of (2.21) were solved iteratively as functions of  $k$  using the Newton-Raphson method. The  $k$ -spacing varied with  $k$  and was arranged to give the smallest spacing in the wave band (see Appendix B) that contributed the largest amount to the integral over  $k$ :

k-range	number of grid points	grid spacing
0.0-0.1	100	.001
0.1-0.5	100	.004
0.5-1.0	100	.005
1.0-5.0	100	.040
5.0-100.	100	.950

In the integrations of section 2.3 ( $U = 0$ ), 500  $k$  points were used. In section 2.4, where a basic current was included, 1000  $k$  points were used; the 1000 points were symmetric about  $k = 0$ .

2. The roots obtained above were then substituted into (2.26)-(2.29) and the fourth order system of equations was solved for each value of  $k$ . The Gauss elimination method was used for both the real and imaginary parts of the coefficients  $b_1$ ,  $\psi_2$ ,  $\psi_3$ , and  $\psi_4$ .

3. The  $\lambda_j$  ( $j=1,2,3,4$ ) and the coefficients were placed into (2.22)-(2.25) and integrated over  $k$ . The cut-off value of  $k_{\max} = 100$  was determined by decreasing the cut-off from the large value of

$k' = 1000$  until the contribution from the interval  $k_{\max} < k \leq k'$  became 0.1% as large as the contribution from  $0 \leq k \leq k_{\max}$ . The value  $k = 100$  corresponds to a wavelength of about 0.02 km and, judging from the scale of motion in the solutions, seems to have been large enough.

Because the functions  $\sin kx$ ,  $\cos kx$ , and  $e^{ikx}$  oscillate very rapidly at large  $x$ , the integrand can be aliased by a fixed grid space. The integrand was therefore approximated as a linear function between grid points (Sullivan, 1970). For example, at a fixed  $(x, z, t)$ ,  $\Psi$  was integrated as follows for the symmetric case ( $U = 0$ ):

$$\begin{aligned} \Psi &= \int_0^{\infty} \operatorname{Re} \left\{ \sum_{j=2}^4 \psi_j(k) e^{-\lambda_j(k)z} e^{it} \right\} \cos kx \, dk \\ &= \int_0^{\infty} f(k) \cos kx \, dk \\ &= \sum_{i=1}^{500} \int_{k_{i-1}}^{k_i} (a_i k + b_i) \cos kx \, dk \\ &= \sum_{i=1}^{500} \left[ a_i \left( \frac{\cos kx}{x^2} + \frac{k \sin kx}{x} \right) + b_i \frac{\sin kx}{x} \right]_{k_{i-1}}^{k_i} \end{aligned}$$

where

$$f_i(k) = \operatorname{Re} \left\{ \sum_{j=2}^4 \psi_j(k_i) e^{-\lambda_j(k_i)z} e^{it} \right\}$$

$$a_i = \frac{f_i - f_{i-1}}{k_i - k_{i-1}}$$

$$b_i = \frac{k_i f_{i-1} - k_{i-1} f_i}{k_i - k_{i-1}}$$

As  $x \rightarrow 0$ , Simpson's rule must be used.

The degree to which the numerical approximations introduced errors into the solution was examined. All terms in (2.1)-(2.5) were

evaluated to see how closely the equations of motion were satisfied. The errors in the various equations, defined as the ratio of the residue of the equation to the largest term, were less than 1%. An exception was the buoyancy equation at large  $x$  ( $\geq 500$ ) where the error approached 4%.

The boundary conditions on  $(u, v, w)$  were satisfied to within one part in  $10^4$ . For  $x \leq 500$ , the lower boundary condition on  $b$  was satisfied to within 2%; at larger  $x$ , the error became as large as 6%.

The larger errors in  $b$  are attributable to the behavior of the coefficient  $b_1$ . As shown in Appendix B,  $b_1$  varies as  $k^{-1}$  as  $k \rightarrow 0$ . Since  $b_1$  appears only in the products  $kb_1$  and  $b_1 \sin kx$ , the solutions clearly remain finite. In the numerical evaluation, however,  $(b_1 \sin kx)_{k=0}$  could not be evaluated because  $(b_1)_{k=0}$  is undefined. It was therefore necessary to set  $k = \delta \sim 10^{-5}$  in order to evaluate  $(b_1 \sin kx)_{k=0}$ . This slight inaccuracy due to the  $k=0$  solution is detectable only at large  $x$ , where the errors approach several per cent as noted above.

### Appendix B. Wave number dependence of the linear solution

The dependence on  $k$  of the eigenvalues is shown in figures B.1a and B.1b. Since the  $\lambda_j$  show little dependence on  $f$ , only the  $\frac{f}{\omega} = 1.5$  curves are included. The solution is symmetric because  $U = 0$  in this example.

For small  $k$ , the hydrostatic and nonhydrostatic values are nearly identical; the eigenvalue  $\lambda_2$  vanishes as  $k \rightarrow 0$ , while the other three eigenvalues approach nonzero limits. At large  $k$ , the nonhydrostatic values become significantly larger than the hydrostatic values. The largest difference is in  $\lambda_1 \equiv \kappa$ . The  $e^{-\lambda_j z}$  dependence implies that there is stronger damping of the high wave-number components in the nonhydrostatic case.

The coefficients  $kb_1$ ,  $\psi_2$ ,  $\psi_3$ , and  $\psi_4$  are shown in figures B.2a-B.2c for three values of  $f$ ; again, only symmetric solutions are examined. Since the hydrostatic and nonhydrostatic values are nearly identical, only the latter are shown. Evidently large values of  $\lambda_j$  ( $j=1,2,3,4$ ) result in very small values of the coefficients. The differences in  $\lambda_j$  due to the hydrostatic approximation therefore have a minimal effect on the coefficients.

The coefficient  $b_1$ , which was discussed in Appendix A, shows little dependence on  $f$ . The values of  $\psi_j$  ( $j=2,3,4$ ) vary considerably with  $f$ ; their limits as  $k \rightarrow 0$  depend on  $f$ . Special attention is given to the case of  $\frac{f}{\omega} = 1.0$ , for which figure B.2b shows that  $\psi_2$  and  $\psi_4$  do not approach finite limits as  $k \rightarrow 0$ .

For  $\frac{f}{\omega} = 1.0$  and small  $k$ , the cubic (2.21) is solved algebraically. Taylor expansions about  $k = 0$  enable the solution to be expressed in

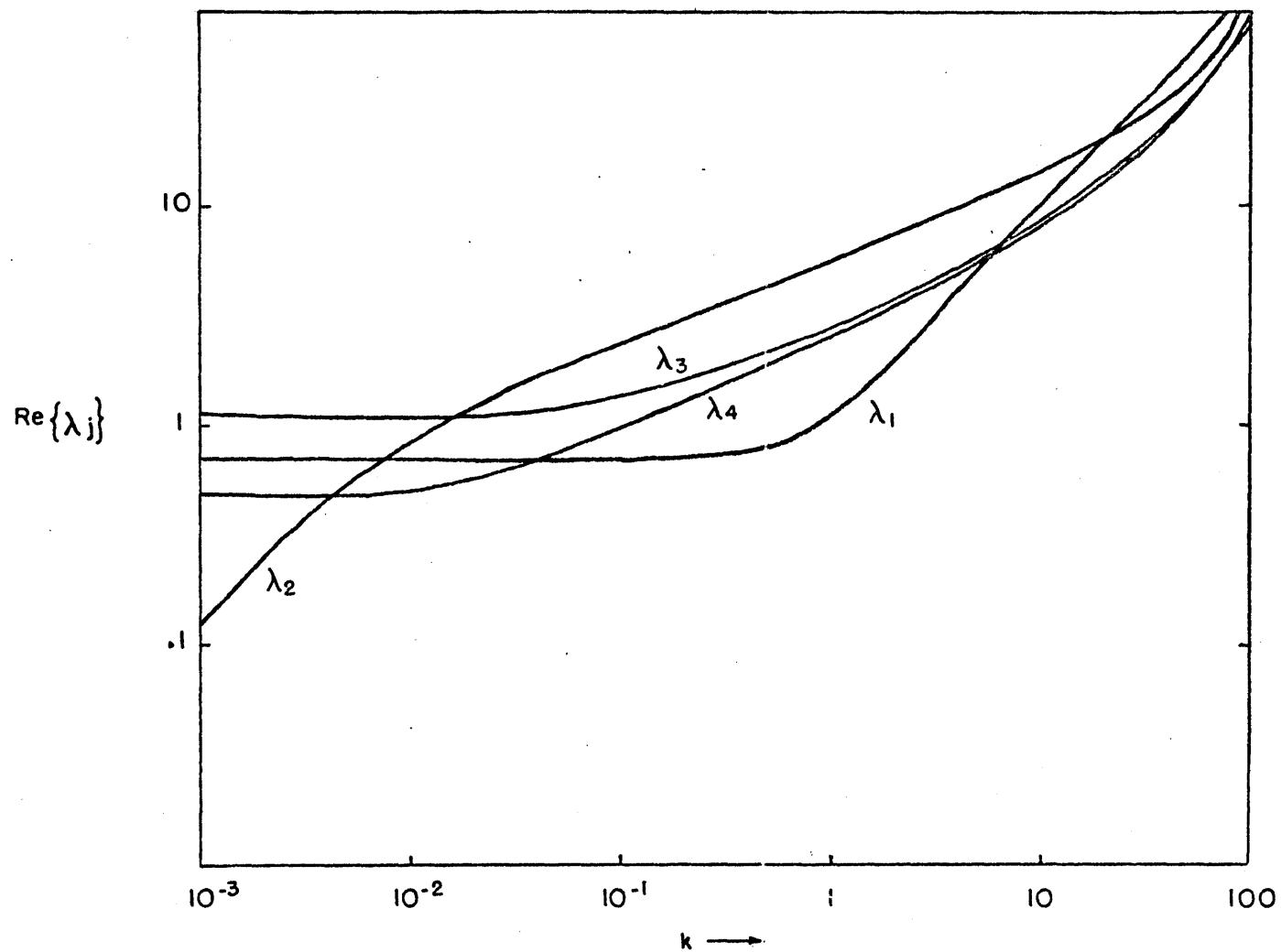


Figure B.1a.  $\text{Re}\{\lambda_j\}$  as a function of the horizontal wave number  $k$  for the nonhydrostatic case of  $\frac{f}{\omega} = 1.5$ ,  $N^2 = 10^{-4} \text{ sec}^{-2}$ ,  $U = 0$ .

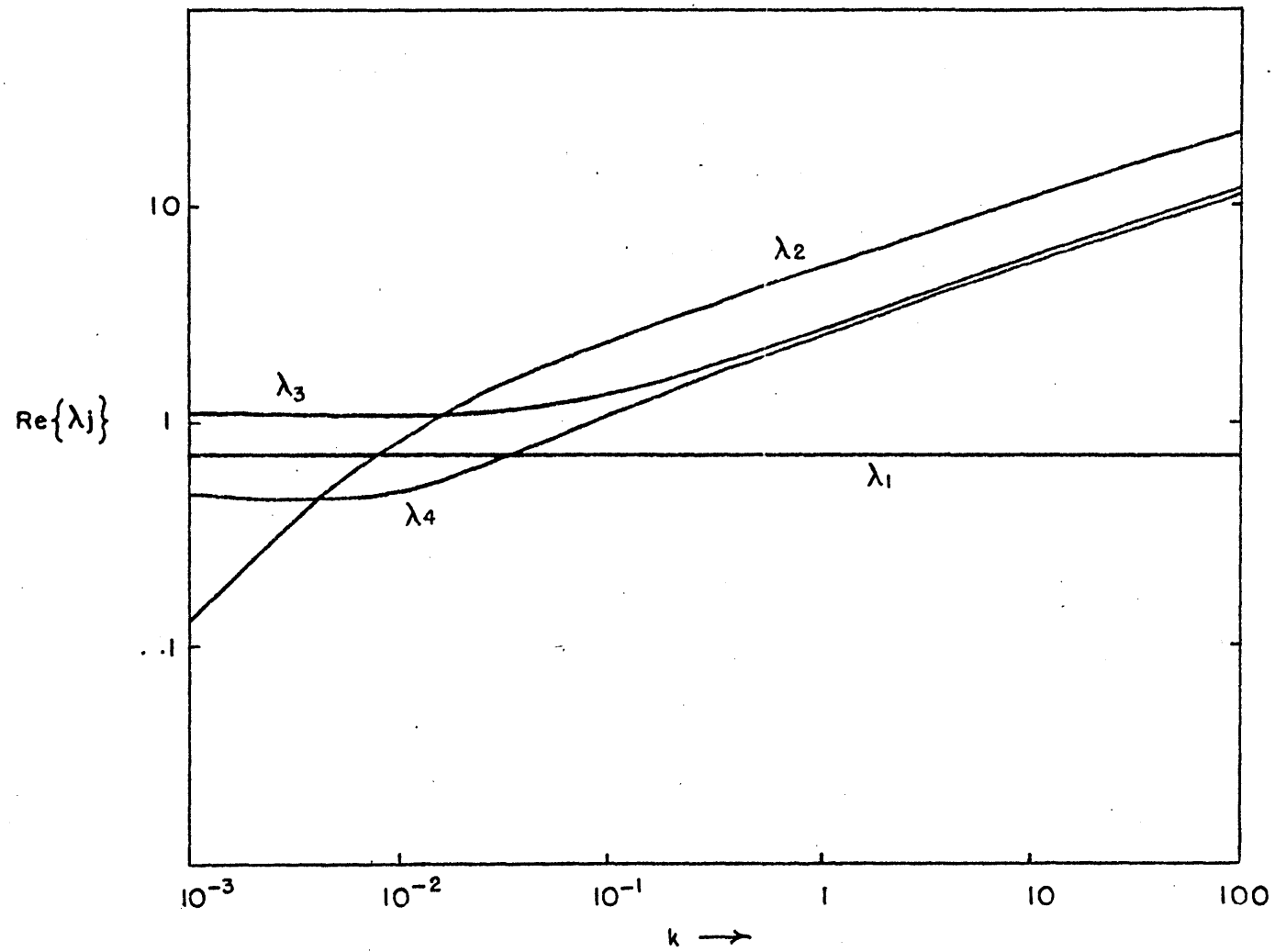


Figure B.1b. Same as figure B.1a but for the hydrostatic case.

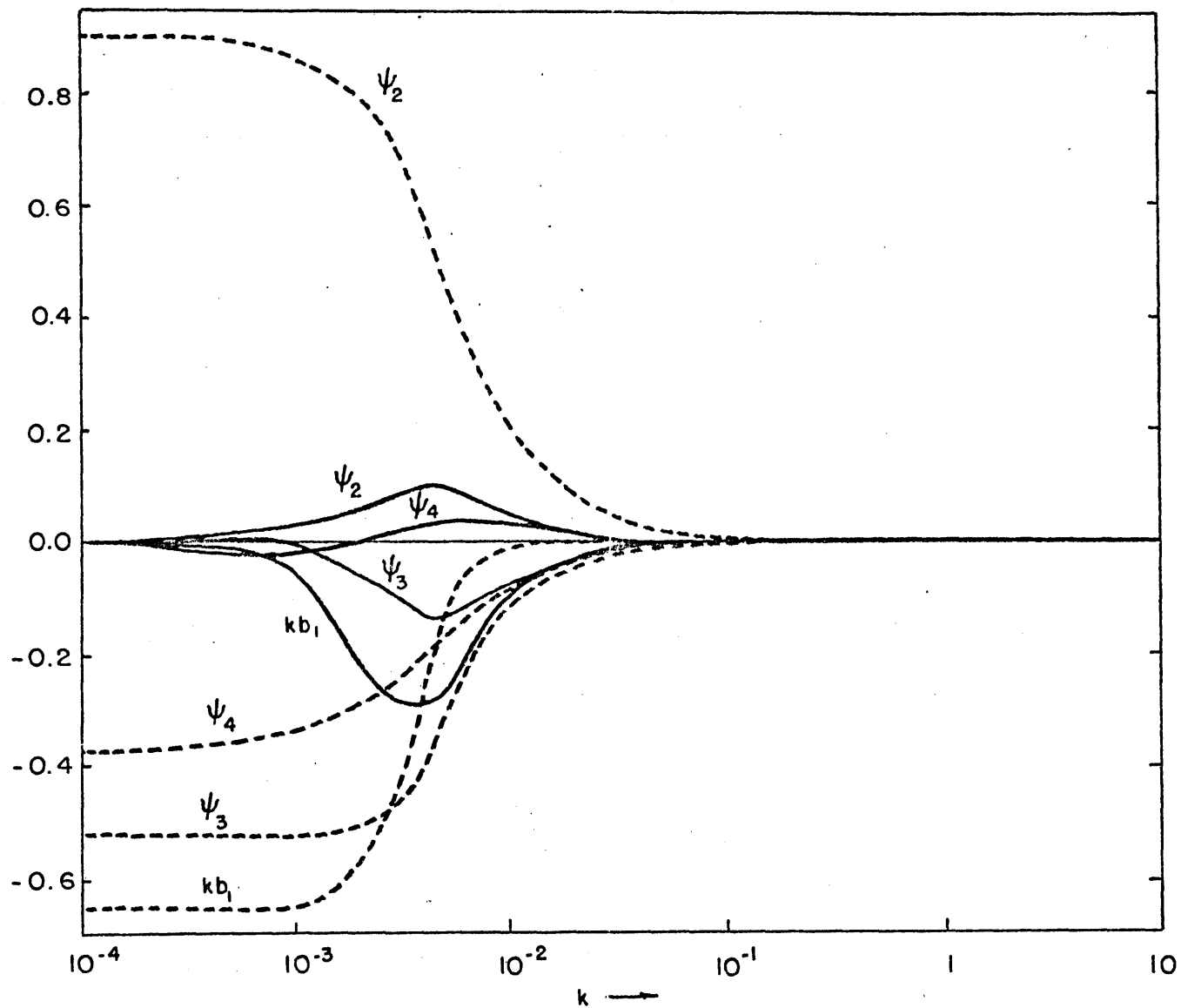


Figure B.2a. The complex coefficients  $b_1, \psi_2, \psi_3, \psi_4$  as functions of the horizontal wave number  $k$  for the nonhydrostatic case of  $\frac{f}{\omega} = 1.5, N^2 = 10^{-4} \text{ sec}^{-2}, U = 0$ . Solid curves are the real parts, dashed curves are the imaginary parts.

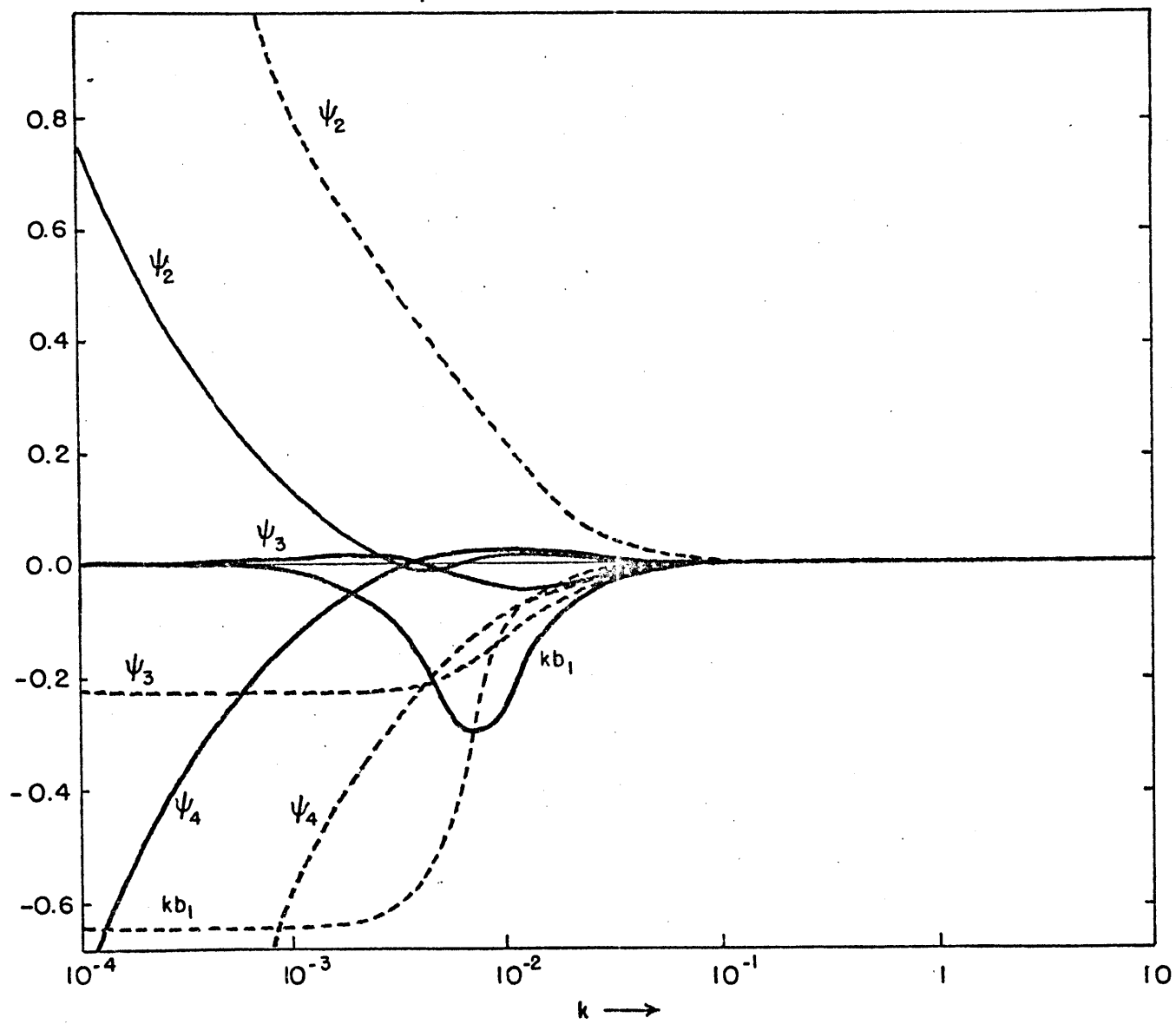


Figure B.2b. Same as figure B.2a but for  $\frac{f}{\omega} = 1.0$ .



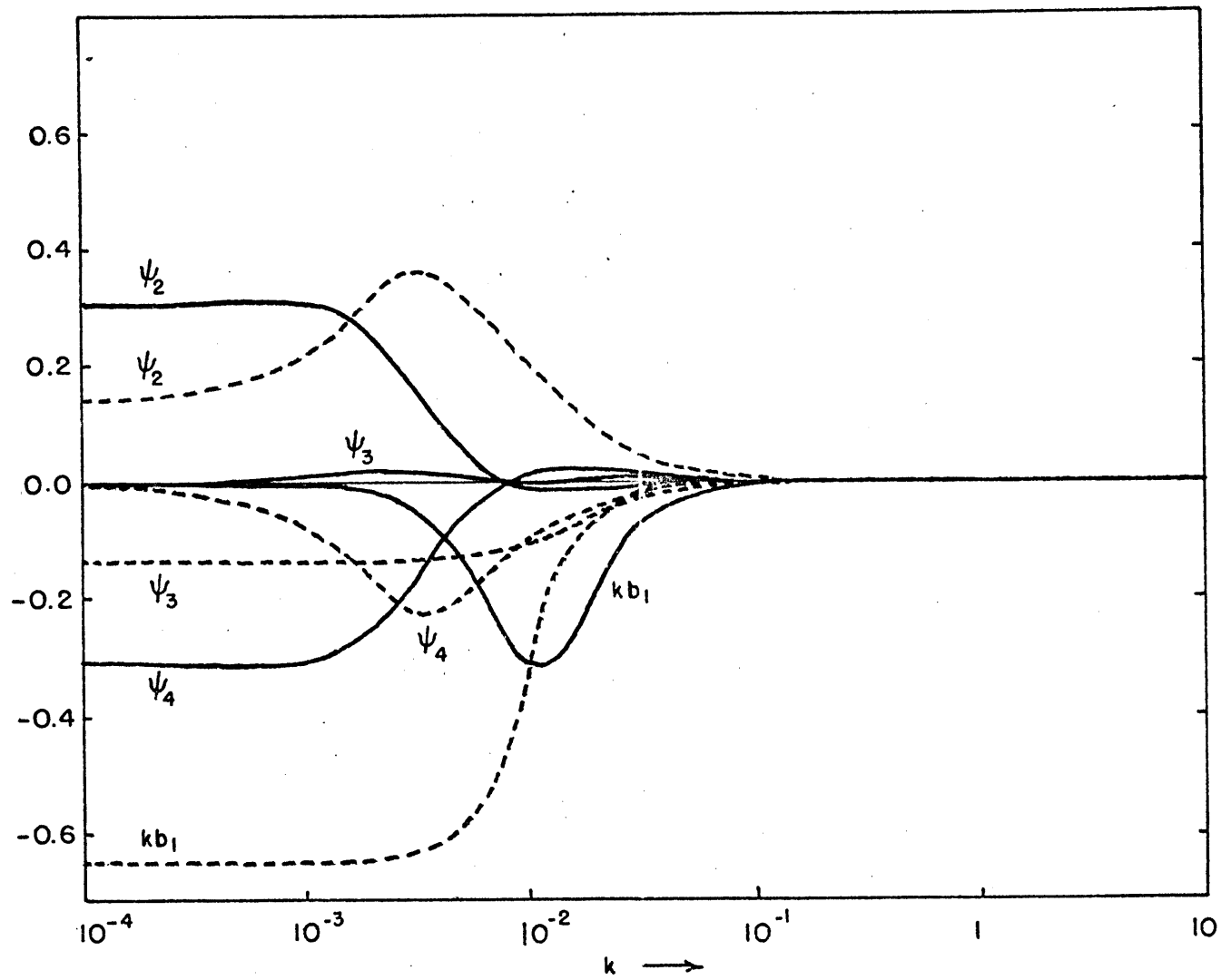


Figure B.2c. Same as figure B.2a but for  $\frac{f}{\omega} = 1.5$ .

powers of  $k^{\frac{1}{2}}$ :

$$\begin{aligned}\lambda_1 &= i^{\frac{1}{2}} + \frac{1}{2i^{\frac{1}{2}}} k^2 + o(k^4) \\ \lambda_2 &= a_1^{\frac{1}{2}} k^{\frac{1}{2}} + \frac{1}{2} a_1^{-\frac{1}{2}} a_2 k^{\frac{3}{2}} + o(k^{\frac{5}{2}}) \\ \lambda_3 &= (1+i) + \frac{1-i}{4} a_3 k^2 + o(k^4) \\ \lambda_4 &= -i a_1^{\frac{1}{2}} k^{\frac{1}{2}} + \frac{i}{2} a_1^{-\frac{1}{2}} a_2 k^{\frac{3}{2}} + o(k^{\frac{5}{2}})\end{aligned}$$

where

$$\begin{aligned}a_1 &\equiv \frac{1+i}{2} \left( \frac{N^2}{\omega^2} - 1 \right)^{\frac{1}{2}} \\ a_2 &\equiv \frac{1}{8} \left( \frac{N^2}{\omega^2} - 1 \right) + 1 \\ a_3 &\equiv 1 - \frac{1}{4} \left( \frac{N^2}{\omega^2} - 1 \right)\end{aligned}$$

Substitution into the expressions for  $\alpha_j$  and  $\gamma_j$  corresponding to the symmetric case gives:

$$\begin{aligned}\alpha_2 &= -i \frac{N^2}{\omega^2} k - a_1 \frac{N^2}{\omega^2} k^2 + o(k^3) \\ \alpha_3 &= i \frac{N^2}{\omega^2} k + (1-a_3) \frac{N^2}{\omega^2} k^3 + o(k^5) \\ \alpha_4 &= -i \frac{N^2}{\omega^2} k + a_1 \frac{N^2}{\omega^2} k^2 + o(k^3) \\ \gamma_2 &= i a_1^{\frac{1}{2}} k^{\frac{1}{2}} + \left( a_1^{\frac{3}{2}} + \frac{1}{2} i a_1^{-\frac{1}{2}} a_2 \right) k^{\frac{3}{2}} + o(k^{\frac{5}{2}}) \\ \gamma_3 &= (1-i) + (1+i) \left( \frac{3a_3}{4} - 1 \right) k^2 + o(k^4) \\ \gamma_4 &= a_1^{\frac{1}{2}} k^{\frac{1}{2}} + \left( i a_1^{\frac{3}{2}} - \frac{1}{2} a_1^{-\frac{1}{2}} a_2 \right) k^{\frac{3}{2}} + o(k^{\frac{5}{2}})\end{aligned}$$

The four boundary conditions are then solved for the coefficients:

$$b_1 = -\frac{2i}{\pi} k^{-1} + o(k) \quad (\text{B.1})$$

$$\psi_2 = -ck^{-\frac{1}{2}} + \frac{i}{\pi\sqrt{2}} + o(k^{\frac{1}{2}}) \quad (\text{B.2})$$

$$\psi_3 = -\frac{i}{\pi\sqrt{2}} + o(k^{\frac{1}{2}}) \quad (\text{B.3})$$

$$\psi_4 = ck^{-\frac{1}{2}} + o(k^0) \quad (\text{B.4})$$

where

$$c = \frac{i^{\frac{5}{2}}}{\pi(1-i)(1+i)^{\frac{1}{2}} \left(\frac{1}{2}\left[\frac{u^2}{\omega^2} - 1\right]\right)^{\frac{1}{2}}}$$

The  $k$ -dependence of (B.1)-(B.4) is consistent with figure B.2b.

Examination of the products  $k\psi_j$ ,  $\lambda_j\psi_j$ ,  $\alpha_j\psi_j$ , and  $\gamma_j\psi_j$  ( $j=2,3,4$ )

shows that the quantities ( $w$ ,  $u$ ,  $v$ ,  $b$ ) remain finite as  $k \rightarrow 0$ , despite the  $k^{-1/2}$  dependence of  $\psi_2$  and  $\psi_4$ .

### Appendix C. Integration of the flux along a coastline

The following procedure is used to compute the land-sea temperature difference  $\Delta T$  for a coastal segment. Mean monthly ocean temperatures  $T_o$  are taken from the U.S. Navy, Marine Climatic Atlas of the World, while monthly means of the maximum and minimum land temperatures  $T_{max}$  and  $T_{min}$  are taken from the British Meteorological Office publication Tables of Temperature, Relative Humidity, and Precipitation for the World. Since the daily range of temperature at coastal stations is reduced by maritime influences (including the sea breeze itself), the land temperatures are taken from stations that are less than several hundred kilometers from, but not squarely on, the coastline. If the only station within several hundred kilometers of the coastline is on the coastline,  $T_{max}$  and  $T_{min}$  are taken from the coastal station.

Given  $T_o$ ,  $T_{max}$ , and  $T_{min}$ , a value is assigned to  $\Delta T$ :

- i) if  $T_{max} \leq T_o$  then  $\Delta T = 0$
- ii) if  $T_{max} > T_o$   
 and  $(T_{max} - T_o) \leq .5(T_{max} - T_{min})$  then  $\Delta T = .5(T_{max} - T_{min})$
- iii) if  $T_{max} > T_o$   
 and  $(T_{max} - T_o) > .5(T_{max} - T_{min})$  then  $\Delta T = \begin{cases} T_{max} - T_o & \text{sea breeze} \\ T_o - T_{min} & \text{land breeze} \end{cases}$
- iv) if  $T_{min} > T_o$  then  $\Delta T = \begin{cases} T_{max} - T_o & \text{sea breeze} \\ 0 & \text{land breeze} \end{cases}$

In categories iii) and iv), the land breeze and sea breeze fluxes are computed separately because of the asymmetry of  $T_{max}$  and  $T_{min}$  about  $T_o$ . Distinctions are made to avoid specifying too large a value of  $\Delta T$  for

either half of the cycle. Categories i), iii), and iv) insure that the land breeze heat flux is never larger than the sea breeze heat flux. This restriction is made because higher nighttime stabilities generally cause the land breeze to be weaker than the sea breeze (see section 2.3.3).

The following data describe the coastal partitioning:

	<u>length of one linear segment</u>	<u>number of stations</u>	<u>approximate # of values of <math>\Delta T</math></u>
Africa	58.8 km	140	55
Asia	67.4 km	155	70
Australia	53.2 km	90	45
Europe	26.3 km	202	95
N. America	48.3 km	160	60
S. America	65.0 km	97	50

#### Appendix D. Formulation of the nonlinear model

The equations are integrated with a two-step Lax-Wendroff scheme based on the time- and space-staggered lattice suggested by Eliassen (1956, see also Phillips, 1962). An "uncentered difference", upstream trajectory computation is used to evaluate the "prime" quantities  $u'$ ,  $v'$ ,  $b'$  at the half time step. A centered difference formulation of the "flux" form of the equations is then used to evaluate  $u$ ,  $v$ , and  $b$  for the next full time-step.

If the vertical interval  $0 \leq z \leq H$  is divided into  $K$  layers, we define  $u$ ,  $v$ ,  $b$ , and  $p$  at the midpoint of each layer and  $w$  at the boundaries of each layer. The lattice is shown in figure D.1, where  $j$  and  $k$  are the horizontal and vertical indices respectively.

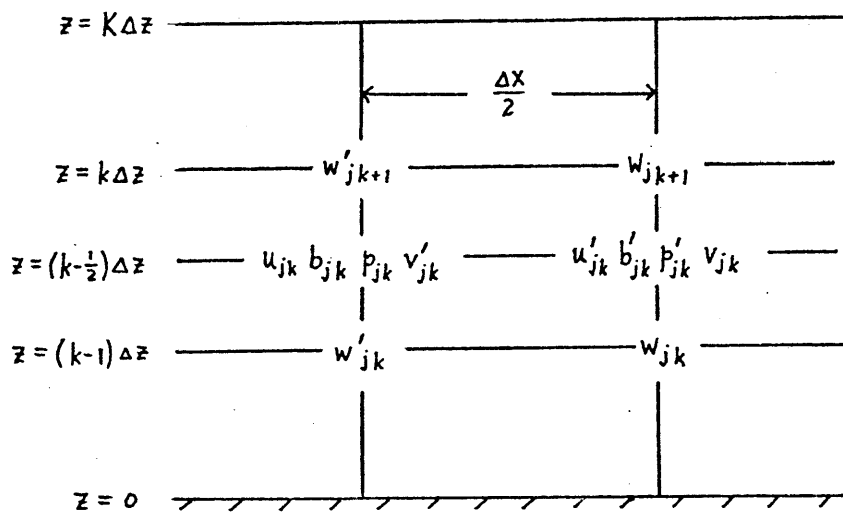


Figure D.1 The modified version of the Eliassen finite-difference grid

### D.1 Finite difference form of the equations

The full-timestep equations corresponding to (4.1)-(4.5) are written in flux form:

$$u_{jkn+1} = u_{jkn} - \sigma_x (FXU_{jk} - FXU_{j-1k}) - \frac{\sigma_z}{4} (FZU_{jk+1} - FZU_{jk}) - \sigma_x (p'_{jk} - p'_{j-1k}) + \lambda v'_{jk} + \delta (u_{jk+1n} - 2u_{jkn} + u_{jk-1n}) \quad (D.1)$$

$$v_{jkn+1} = v_{jkn} - \sigma_x (FXV_{j+1k} - FXV_{jk}) - \frac{\sigma_z}{4} (FZV_{j+1k+1} + FZV_{jk+1} - FZV_{j+1k} - FZV_{jk}) - \lambda u'_{jk} + \delta (v_{jk+1n} - 2v_{jkn} + v_{jk-1n}) \quad (D.2)$$

$$b_{jkn+1} = b_{jkn} - \sigma_x (FXB_{jk} - FXB_{j-1k}) - \frac{\sigma_z}{4} (FZB_{jk+1} - FZB_{jk}) - \frac{\eta}{2} (w'_{jk+1} + w'_{jk}) + \delta (b_{jk+1n} - 2b_{jkn} + b_{jk-1n}) \quad (D.3)$$

$$p_{jkn} = p_{jk-1n} + \frac{\Delta z}{2} (b_{jkn} + b_{jk-1n}) \quad (D.4)$$

$$w_{jk+1n} = w_{jkn} - \frac{\Delta z}{\Delta x} (u_{j+1kn} - u_{jkn}) \quad (D.5)$$

where  $\sigma_{(x,z)} \equiv \frac{\Delta t}{\Delta(x,z)}$ ,  $\lambda \equiv f\Delta t$ ,  $\eta \equiv N^2\Delta t$ , and  $\delta \equiv \frac{\nu\Delta t}{(\Delta z)^2}$  ( $\nu = \kappa$ ). The flux terms are given by

$$FXU_{jk} \equiv (U + u'_{jk})^2$$

$$FZU_{jk} \equiv w'_{jk} (u'_{jk} + u'_{j-1k} + u'_{jk-1} + u'_{j-1k-1})$$

$$FXV_{jk} \equiv v'_{jk} \left[ U + (u'_{jk} + u'_{j-1k})/2 \right]$$

$$FZV_{jk} \equiv w'_{jk} (v'_{jk} + v'_{jk-1})$$

$$FXB_{jk} \equiv b'_{jk} (U + u'_{jk})$$

$$FZB_{jk} \equiv w'_{jk} (b'_{jk} + b'_{j-1,k} + b'_{j,k-1} + b'_{j-1,k-1})$$

The half-timestep (prime) variables in (D.1)-(D.5) have previously been computed from the equations

$$u'_{jk} = u^*_{jkn} - \frac{\sigma_x}{2} (p_{j+1,k} - p_{jk}) + \frac{\lambda}{2} v_{jkn} \\ + \frac{\delta}{4} [(u_{j+1} + u_j)_{k+1n} - 2(u_{j+1} + u_j)_{kn} + (u_{j+1} + u_j)_{k-1n}]$$

$$v'_{jk} = v^*_{jkn} - \frac{\lambda}{2} u_{jkn} + \frac{\delta}{4} [(v_j + v_{j-1})_{k+1n} - 2(v_j + v_{j-1})_{kn} + (v_j + v_{j-1})_{k-1n}]$$

$$b'_{jk} = b^*_{jkn} - \frac{\eta}{2} (w_{jk+1n} + w_{jkn}) + \frac{\delta}{4} [(b_{j+1} + b_j)_{k+1n} - 2(b_{j+1} + b_j)_{kn} + (b_{j+1} + b_j)_{k-1n}]$$

$$p'_{jk} = p'_{jk-1} + \frac{\Delta z}{2} (b'_{jk} + b'_{jk-1})$$

$$w'_{jk+1} = w'_{jk} - \frac{\Delta z}{\Delta x} (u_{jkn} - u_{j-1kn})$$

Asterisks denote the values of  $u$ ,  $v$ ,  $b$  at  $t = n\Delta t$  at the point upstream the distance  $(-\bar{u}\frac{\Delta t}{2}, -\bar{w}\frac{\Delta t}{2})$  from the point corresponding to the location of  $u'$ ,  $v'$ ,  $b'$  at the half-timestep. Overbars represent averages of the nearest surrounding values of  $u$ ,  $v$ ,  $b$ . Values of  $u^*$ ,  $v^*$ , and  $b^*$  are obtained by interpolation with the polynomial  $a + bx + cy + dxz$  fitted to the four surrounding points of  $u$ ,  $v$ , and  $b$  respectively. Two of these surrounding points are at the same level as  $u'$ ,  $v'$ , and  $b'$ , while the other two are located above or below depending on the sign of  $w$ .



The lower boundary conditions are the same as in the linear model:

$$u = v = w = 0; \quad b_0 \text{ specified} \quad (z = 0)$$

At the upper boundary, we assume that all perturbation variables vanish:

$$u = v = w = b = 0 \quad (z = K\Delta z)$$

In the evaluation of the diffusion terms at  $k = K$ , the values of  $u_K$ ,  $v_K$ , and  $b_K$  are reflected across the boundary to obtain  $u_{K+1} = -u_K$ , etc.

At  $k = 1$ ,  $u$  and  $v$  are again reflected, while  $\left(\frac{\partial^2 b}{\partial z^2}\right)_{k=1}$  is computed by assuming

$$\left(\frac{\partial b}{\partial z}\right)_{z=0} = \frac{2(b_1 - b_0)}{\Delta z}$$

At the extreme lateral boundaries, the boundary conditions depend on whether a basic current is present. When there is no current, the assumption of a forcing function that is periodic in  $x$  gives:

$$u(x_R + \epsilon) = -u(x_R - \epsilon)$$

$$b(x_R + \epsilon) = b(x_R - \epsilon)$$

$$v(x_R + \epsilon) = -v(x_R - \epsilon)$$

$$u(x_L - \epsilon) = -u(x_L + \epsilon)$$

$$b(x_L - \epsilon) = b(x_L + \epsilon)$$

$$v(x_L - \epsilon) = -v(x_L + \epsilon)$$

$$(U = 0)$$

where  $\epsilon = \Delta x$  for  $u$ ,  $b$ ;  $\epsilon = \frac{\Delta x}{2}$  for  $v$ .

In the presence of a basic current, these conditions are changed to

$$\begin{aligned}
 \text{outflow boundary:} \quad u &= u_{int} \\
 b &= b_{int} \\
 v' &= v'_{int} \\
 w' &= w'_{int} \quad (U \neq 0) \\
 v &= 0
 \end{aligned}$$

$$\begin{aligned}
 \text{inflow boundary:} \quad u &= 0 \\
 b &= \tilde{b} \\
 v' &= 0 \\
 w' &= 0 \quad (U \neq 0) \\
 v &= 0
 \end{aligned}$$

where  $\tilde{b}$  is forecast using vertical diffusion only.

In order to compute the pressure term from the hydrostatic relation, it is necessary to assume  $p_{k=1} = 0$ . The computed pressure  $p_c$  will therefore differ from the actual pressure by a function of  $x$ :

$$p_{\text{correct}} = p_c + p_o(x)$$

The unknown function  $p_o(x)$  is incorporated into the solution by adjusting  $u$  and  $u'$  to satisfy the requirement  $\sum_{k=1}^K u_{jk} = 0$  imposed by the continuity equation and the lower boundary conditions  $w_{z=0} = 0$  and

$w_{z=K\Delta z} = 0$ . The correction formula for  $u$  is

$$(u_{jk})_{corrected} = u_{jk} - \frac{1}{K} \sum_{k=1}^K u_{jk}$$

The following computational stability criterion applies:

$$\left[ \frac{\Delta t}{\Delta x} (|U| + |c_{gr}| + |u|_{max}) + \frac{\Delta t}{\Delta z} |w|_{max} \right] < 1 \quad (D.6)$$

where  $c_{gr} \approx \frac{NH}{\pi} \approx 8 \text{ m sec}^{-1}$  is the phase speed of the most rapidly travelling gravity wave.

#### D.2. The system of overlapping grids

Figure D.2 shows the relative positions of the seven overlapping grids. The vertical space increment is the same for each grid:  $\Delta z = \frac{H}{K}$  where  $H$  is the height of the lid (2.5 km) and  $K$  is the number of levels. The horizontal space increments are specified to give finer resolution near the coastline, and the time increments are chosen to satisfy the stability criterion (D.6):

<u>grid #</u>	<u><math>\Delta x</math></u>	<u><math>\Delta t</math></u>
1	4.0 km	240 sec
2	2.0 km	120 sec
3	1.0 km	60 sec
4	0.5 km	30 sec

The central grid (4) contains 40 points in the horizontal, while each of

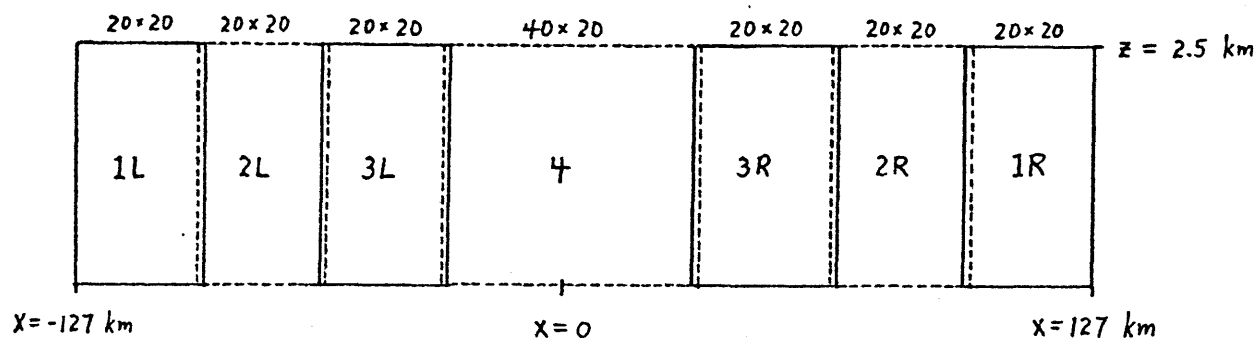


Figure D.2. The system of overlapping grids

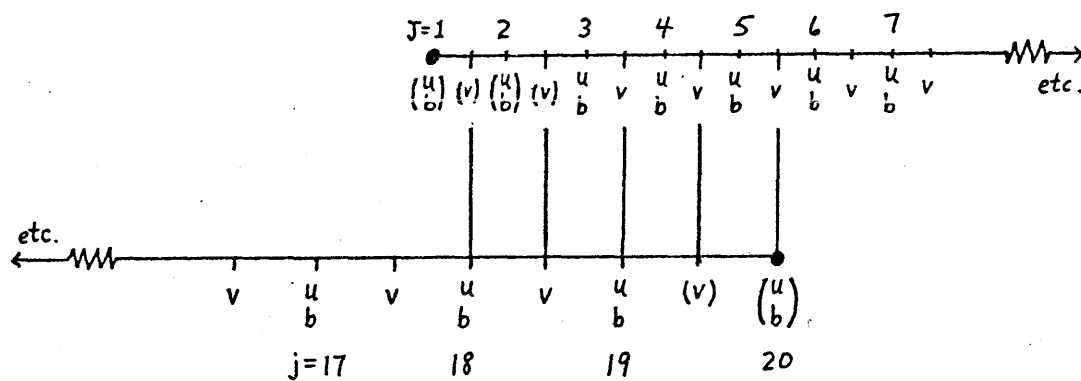


Figure D.3. Cross-section along the x-axis through an overlap region in the left half of the grid system (figure D.2). The sketch shows the relative position of variables on the coarse mesh (upper) and fine mesh (lower) at full time steps of the two-step Lax-Wendroff procedure. Indices  $J$  and  $j$  apply to the coarse and fine meshes. Heavy dots denote extreme points of both grids, and parentheses denote values obtained by interpolation from the other grid.

the other six grids contains 20 points in the horizontal.

At the boundaries of adjacent grids, the "two-way" interaction scheme of Phillips and Shukla (1973) is used. The forecasts for the coarse and fine grids are made independently, but the innermost column of the coarse grid and the outermost two columns of the fine grid are interpolated from the other grid after each (full) time step of the coarse grid. Linear interpolation formulae are used. The overlap is designed to be as small as possible without requiring interpolation between values which have themselves been interpolated. The overlap between two of the meshes is illustrated in figure D.3.

The following algorithm describes the integration procedure:

- A1) Set  $n = 0$  and initialize  $u, v, b$  to 0 on all grids, all points.
- A2) Begin the largest time step:  $t = n \Delta t$  ( $\Delta t = 4$  min).
- A3) Apply the lateral boundary conditions to the outermost grids.
- A4) (Note: for each time step ( $\Delta t, \frac{\Delta t}{2}, \frac{\Delta t}{4}, \frac{\Delta t}{8}$ ), the expression  $(\pm) b_0 = b_{\max} \sin \omega t$  is recomputed using  $t$  at the beginning of the time step).
 

Forecast grids 3, 4, 4	interpolate 3 $\leftrightarrow$ 4
Forecast grids 2, 3, 4, 4	interpolate 2 $\leftrightarrow$ 3, 3 $\leftrightarrow$ 4
Forecast grids 3, 4, 4	interpolate 3 $\leftrightarrow$ 4
Forecast grids 1, 2, 3, 4, 4	interpolate 1 $\leftrightarrow$ 2, 2 $\leftrightarrow$ 3, 3 $\leftrightarrow$ 4
- A5) Set  $n = n + 1$  and return to A2.

## REFERENCES

- Bhumralkar, C. M., 1972: An observational and theoretical study of atmospheric flow over a heated island. U. of Miami, Final Report: GA-14156.
- Budyko, M. I., 1958: The Heat Balance of the Earth's Surface, translated by the U. S. Weather Bureau, 259 pp.
- Bugaev, V. A., 1973: Dynamic climatology in light of satellite information. Bull. Amer. Meteor. Soc., 54, 394-418.
- Defant, F., 1950: Theorie der land- und seewinde. Arch. Meteor. Geophys. Biokl., 2(A), 404-425.
- , 1951: Local winds. Compendium of Meteorology, Amer. Meteor. Soc., pp. 655-662.
- Dolezel, E. J., 1948: A study of the sea breeze potential for the case of an offshore general wind. M.I.T. Sc. D. thesis.
- Eliassen, A., 1956: A procedure for numerical integration of the primitive equations of the two-parameter model of the atmosphere. Sci. Rept. 4, Dept. Meteor., U.C.L.A., 53 pp.
- Estoque, M. A., 1961: A theoretical investigation of the sea breeze. Quart. Jour. Roy. Meteor. Soc., 87, 136-146.
- , 1962: The sea breeze as a function of the prevailing synoptic situation. Jour. Atmos. Sci., 19, 244-250.
- and C. M. Bhumralkar, 1969: Flow over a localized heat source. Mon. Wea. Rev., 97, 850-859.
- Fisher, E. L., 1960: An observational study of the sea breeze. Jour. of Meteor., 17, 645-660.
- , 1961: A theoretical study of the sea breeze. Jour. of Meteor. 18, 216-233.
- Geisler, J. E. and F. P. Bretherton, 1969: The sea-breeze forerunner. Jour. Atmos. Sci., 26, 82-95.
- Hatcher, R. W. and J. S. Sawyer, 1947: Sea breeze structure with particular reference to temperature and water vapor gradients and associated radio ducts. Quart. Jour. Roy. Meteor. Soc., 73, 391-406.
- Haurwitz, B., 1947: Comments on the sea breeze circulation. Jour. of Meteor., 4, 1-8.

- Holton, J. R., 1972: An Introduction to Dynamic Meteorology, Academic Press Inc., New York, 319 pp.
- Houghton, H. G., 1954: On the annual heat budget of the northern hemisphere. Jour. of Meteor., 11, 1-9.
- Hsu, S. A., 1967: Mesoscale surface temperature characteristics of the Texas coast sea breeze. U. of Texas, Atmos. Sci. Group, Report No. 6.
- Kimble, G. M. T., et al., 1946: Tropical land and sea breezes. Bull. Amer. Meteor. Soc., 27, 99-113.
- Kondratyev, K. Y., 1969: Radiation in the Atmosphere, Academic Press, Inc., New York, 912 pp.
- Kuo, K. L., 1968: The thermal interaction between the atmosphere and the earth and the propagation of diurnal temperature waves. Jour. Atmos. Sci., 25, 682-705.
- LeBlanc, L. L. and K. C. Brundige, 1969: A numerical experiment in predicting stratus clouds. Jour. Appl. Meteor., 8, 177-189.
- Lettau, H. H., 1949: Isotropic and non-isotropic turbulence in the atmospheric surface layer. AFCRL Geophysical Research Papers, No. 1, 86 pp.
- , 1951: Theory of surface-temperature and heat-surface oscillations near a level ground surface. Trans. Amer. Geophys. Union, 32, 189-200.
- London, J., 1957: A study of the atmospheric heat balance. Final Report, Project 131. N.Y.U. Dept. of Meteor. and Oceano., New York.
- Lyons, W. A., 1972: The climatology and prediction of the Chicago lake breeze. Jour. Appl. Meteor., 11, 1259-1270.
- Malkus, J. S. and M. E. Stern, 1953a: The flow of a stable atmosphere over a heated island, Part I. Jour. of Meteor., 10, 30-41.
- , and ----, 1953b: see Stern, M. E., and J. S. Malkus, 1953b.
- McPherson, R. D., 1968: A three dimensional numerical study of the Texas coast sea breeze. U. of Texas, Coll. of Engineering, Report No. 15.
- , 1970: A numerical study of the effect of a coastal irregularity on the sea breeze. Jour. Appl. Meteor., 9, 767-777.
- Moroz, W. J., 1967: A lake breeze on the eastern shore of Lake Michigan: Observations and model. Jour. Atmos. Sci., 24, 337-355.
- Mudrick, S., 1973: A numerical study of frontogenesis. Ph. D. thesis, M.I.T. Dept. of Meteorology, Cambridge, Mass., 248 pp.

- Neumann, R. J., and B. A. Mahrer, 1971: A theoretical study of the land and sea breeze circulation. Jour. Atmos. Sci., 28, 532-542.
- Ogura, Y. and H. Kondo, 1970: A linear stability of convective motion in a thermally unstable layer below a stable region. Jour. Meteor. Soc. Japan, 48, 204-216.
- , and N. A. Phillips, 1962: Scale analysis of deep and shallow convection in the atmosphere. Jour. Atmos. Sci., 19, 173-179.
- Olfe, D. B. and R. L. Lee, 1971: Linearized calculations of urban heat island convection effects, Jour. Atmos. Sci., 28, 1374-88.
- Palmen, E. and C. W. Newton, 1969: Atmospheric Circulation Systems, Academic Press, Inc., New York, 603 pp.
- Pearce, R. P., 1955: The calculation of a sea breeze circulation in terms of differential heating across a coastline. Quart. Jour. Roy. Meteor. Soc., 81, 351-381.
- Pearson, R. A., 1973: Properties of the sea breeze front as shown by a numerical model. Jour. Atmos. Sci., 30, 1050-1060.
- Phillips, N. A., 1962: Numerical integration of the hydrostatic system of equations with a modified version of the Eliassen finite difference grid. Proceedings of the International Symposium on Numerical Weather Prediction, Tokyo, Japan, 1962.
- , and J. Shukla, 1973: On the strategy of combining coarse and fine grid meshes in numerical weather prediction. Jour. Appl. Meteor., 12, 763-770.
- Pielke, R. A., 1973: A three-dimensional numerical model of the sea breezes over south Florida. NOAA Technical Memorandum ERL-WMPO-2, Weather Modification Program Office, Boulder, Colo., 136 pp.
- Pierson, W. J., Jr., 1950: The effects of eddy viscosity, coriolis deflection, and temperature fluctuation on the sea breeze as a function of time and height. Meteor. Pap. N. Y. Univ., Vol. 1, No. 2, 29 pp.
- Rider, N. E., 1954: Eddy diffusion of momentum, water vapor, and heat near the ground. Phil. Trans. Roy. Soc. London, A246, 481-501.
- Schmidt, F. H., 1947: An elementary theory of the land and sea breeze circulation. Jour. of Meteor., 4, 9-15.
- Smith, R. C., 1955: Air motion over a heated land mass. Quart. Jour. Roy. Meteor. Soc., 81, 382-395.
- , 1957: Air motion over a heated land mass, Part II. Quart. Jour. Roy. Meteor. Soc., 83, 248-256.



Stern, M. E., 1954: The theory of mean atmospheric perturbations produced by differential surface heating. Jour. of Meteor., 11, 495-502.

----, and J. S. Malkus, 1953b: The flow of a stable atmosphere over a heated island, Part II. Jour. of Meteor., 10, 105-120.

Sullivan, J. B., 1970: On the generation of inertial-gravity waves in the ocean. Ph. D. thesis, M.I.T. Dept. of Meteorology, 102 pp.

Tables of Temperature, Relative Humidity, and Precipitation for the World, 1958, British Meteorological Office, London, parts I-VI.

U.S. Navy, Marine Climatic Atlas of the World, 1959. NAVAER 50 1C-54, vol. VIII, U.S. Govt. Printing Off., Washington, D.C.

Wexler, R., 1946: Theory and observation of land and sea breezes. Bull. Amer. Meteor. Soc., 27, 272-287.

Yoshikado, Y. and T. Asai, 1972: A numerical experiment of effects of turbulent transfer processes on the land and sea breeze. Contributions, Geophysical Institute, Kyoto U., No. 12, 33-48.

## BIOGRAPHICAL NOTE

The author was born on 9 August 1948, raised in the Philadelphia area, and graduated from Devon (Pa.) Preparatory School. In 1970, he received a B. A. in mathematics from Dartmouth College, where he met his wife, Laura R. Lynn. Summer work was done at the U.S. Naval Oceanographic Office and at the Arctic Institute of North America, both in Washington, D.C. He enrolled at M.I.T. in September 1970, where he has been supported by an NDEA fellowship and a research assistantship.